Systematic Methodology for Enhanced Performance Prediction in Designing Large Active Phased Array Antennas for Satellite Communication

by

Justin Tung

A thesis
presented to the University of Waterloo
in fulfillment of the
thesis requirement for the degree of
Master of Applied Science
in
Electrical and Computing Engineering

Waterloo, Ontario, Canada, 2025

© Justin Tung 2025

Author's Declaration

I hereby declare that I am the sole author of this thesis. This is a true copy of the thesis, including any required final revisions, as accepted by my examiners.

I understand that my thesis may be made electronically available to the public.

Abstract

The deployment of 5th generation (5G) and the development of 6th generation (6G) networks have increased the demand for global connectivity at high data rates. Traditional terrestrial infrastructure, including base stations and optical fiber, faces challenges in remote or sparsely populated regions, such as mountainous terrain and oceans. Satellite communication (SATCOM) provides a complementary solution, enabling direct wireless links between users and satellite constellations, removing the need for implementing optic fiber cables. Low earth orbit (LEO) satellites have been proposed as they reduce latency and power requirements compared to traditional geostationary satellites, but their constant motion necessitates rapid beam tracking. At the same time, Ka-band operation (27.5–31 GHz) offers wide bandwidths for high data rates but requires high-gain antennas to overcome propagation losses. Electronically steerable Phased Array Antennas (PAAs) have emerged as the leading solution to address these requirements by enabling fast beam steering without mechanical components. Achieving the necessary gain, however, demands large arrays, which introduces significant design challenges.

This thesis presents a systematic design methodology for large 26.5–40 GHz (Ka)-band active PAAs and their feed networks. The methodology leverages industry-standard eletromagnetic (EM) simulation models to guide the design of antenna elements and feed networks, ensuring wideband and scalability. Using this approach, a 16×16 active PAA is designed, integrating 64 beamforming integrated circuits (BFICs). Critical system-level considerations, including DC power delivery, digital signal integrity, and thermal management, are then analyzed to ensure reliable operation.

Acknowledgements

I would like to thank Professor Boumaiza for giving me the opportunity to be part of EmRG for the last two years, as well as providing invaluable guidance and mentorship throughout my graduate studies.

I would like to thank my parents for always supporting me in everything I do, without whom I would not have been able to complete this thesis. Thank you for all your sacrifices to provide me with opportunities in life.

I would like to thank my brother, Bernard, for convincing me to join EmRG and feeding me throughout my graduate studies. I have a sister.

I would also like to thank Dr. Ahmed Ben Ayed and Huixin Jin for their invaluable input.

Table of Contents

Author's Declaration ii

Abstract iii

Acknowledgements iv

List of Figures vii

List of Tables xii

List of Abbreviations xiii

1 Introduction 1

1.1 Motivation 1

1.2 Problem Statement 3

1.3 Thesis Organization 4

2 Background and Literature Review 5

2.1 Antennas and Phased Arrays 5

2.1.1 Figures of Merits 5

2.2 Literature Review 15

2.2.1 Patch Antennas 15

2.2.2 Active Phased Array Antenna Stack-up 27

2.2.3 Large Scale Phased Array Antennas for Satellite Communication . . 30

3 Design Methodology of Large Phased Array Antenna and Feed Network 35
3.1 Design Requirements . . . 35
3.1.1 Antenna Design Requirements . . . 35
3.1.2 Feed Network Design Requirements . . . 36
3.2 PCB Stack-Up Definition . . . 36
3.3 Antenna Design . . . 38
3.3.1 Antenna Analysis in a Large Array . . . 38
3.3.2 Design Methodology of Large Phased Array Antennas . . . 42
3.3.3 Patch Antenna Design . . . 43
3.4 Feed Network Design . . . 55
3.4.1 Design Methodology of the Feed Network . . . 56
3.4.2 Power Divider Topologies . . . 58
3.4.3 Design of Power Divider Network . . . 60

4 16 × 16 Active Phased Array Antenna Analysis 67
4.1 System Architecture . . . 67
4.2 DC Power Analysis . . . 70
4.3 Signal Integrity Analysis . . . 72
4.4 Thermal Analysis . . . 75

5 Conclusion and Future Works 77
5.1 Conclusion . . . 77
5.2 Future Works . . . 78

References 80

List of Figures

1.1 Areas of interest proposed for 6G coverage. [1] 1

2.1 2-D cut of a typical radiation pattern. [4] 8

2.2 The array factor is plotted varying the spacing between antenna elements at (a) boresight and (b) $\theta = -60°$. 9

2.3 Example of traveling electromagnetic waves in linear, circular and elliptical polarization (left to right) [5]. At the end of each wave shows what is observed over time at a fixed observation point. 11

2.4 Typical structure of an edge fed patch antenna which includes a patch, a ground layer beneath it, and a microstrip line fed directly to the patch. [6] 15

2.5 The antenna designed in [8], where (a) shows the top view and (b) shows the side view and the stack-up. (c) shows the measured reflection coefficient of the antenna. 16

2.6 (a) Dual linear polarized probe fed patch antenna at 29.5 GHz and (b) dual band version at 19.5 GHz and 29.5 GHz in [11]. (c) interleaved array configuration of antennas in (a) and (b) used in [11]. 17

2.7 Patch antenna fed by an L-shaped probe introduced in [12]. 18

2.8 (a) Linearly polarized proximity-fed patch antenna at 70 GHz. (b) Full stack-up of the active PAA, showing the packaged antenna and BFICs mounted on the carrier board with the cooling solution. (c) Four 4×4 subarrays combined to form an 8×8 array [13]. 19

2.9 (a) Dual linearly polarized proximity-fed patch antenna at 140 GHz arranged in a 1×4 subarray with two 1-to-4 vertical dividers. (b) Sixteen 1×4 subarrays combined to form an 8×8 array, including the two 1-to-8 dividers [14]. 20

2.10 (a) Dual linearly polarized proximity fed patch antenna with a shielding structure at 60 GHz and the (b) fabricated 4×4 array in [15]. 20

2.11 (a) Stack-up of proposed linear polarized aperture fed stacked patch antenna. The two methods of feeding the slot are by using a (b) low impedance stub or by using (c) two 100Ω stubs joined together by a power combiner [17]. . 21

2.12 (a) Dual linearly polarized cross slot fed patch antenna at 2.8 GHz fed with two fork feeds. (b) Stack-up of the antenna showing the location of each component in the stack-up in [18]. (c) The 8×8 array as well as the measurement setup. 22

2.13 Dual linear polarized stacked patch antenna using offset orthogonal H-shaped slots with added shorting vias to improve isolation between feeds. [19] . . . 23

2.14 (a) Single feed square patch with a diagonal slot to generate circular polarization [4]. Single feed square patch with truncated corners to generate circular polarization [4]. (c) Dual feed patch to generate circular polarization [4]. (d) Sequentially rotated antennas to generate circular polarization [16]. 24

2.15 (a) Patch antenna with truncated corners. (b) 2×2 subarray of patch antennas with truncated corners oriented in with sequential rotation to improve axial ratio (AR). [21] 25

2.16 (a) Probe fed stacked patch antenna (b) with L stubs in [22]. (c) 2×2 mirrored antennas used in [22]. 26

2.17 General block diagram of an active PAA fabricated using a (a) single printed circuit board (PCB) and when using (b) antennas in tiled packages onto a PCB [24]. 28

2.18 (a) Stack-up of a 6+2+6 antenna-in-package (AIP). (b) Bottom side of the AIP showing the BFICs, power splitter, bandpass filter, and up/downconverter [25]. 29

2.19 The array factor of a linear 16 element array made up of four 1×4 subarrays at 13 GHz when (a) there are no gaps in between the tiles and when (b) there is a 3 mm gap between the tiles. The blue curve shows the 1×4 subarray array factor; the green curve shows the array factor of the four tiles; and the red shows the combination of the green and blue curves [26]. 30

2.20 Block diagram of the 1024 element transmitter active phased array in [27]. 31

2.21 2×2 subarray used in [27] to build the 1024 element array. 32

2.22 The Wilkinson power divider (WPD) used in [27, 28] where (a) shows the circuit model and (b) shows the layout. 32

2.23 The 1024 element transmitter array in [27]. (a) Bottom side of the PCB. (b) Top side of the PCB. 33

2.24 1024 element transmitter array in [29]. (a) Bottom side of the PCB. (b) Top side of the PCB. 33

3.1 12-layer PCB stack-up using high-density interconnect (HDI) process with micro-via to access every layer. 37

3.2 (a) Fabricated cross-section of the proposed 12-layer stack-up. (b) Cracking between via and pad. (c) Misalignment of micro-vias. 38

3.3 (a) Explicit simulation boundary condition shown in red where there are radiation boundaries on all 6 faces. (b) Unit cell under periodic boundary condition, where the radiation boundaries are on the top and bottom, while the pair of parallel faces are set to be equivalent. 39

3.4 $S_{1,1}$ of an antenna simulated under periodic boundary condition compared to when simulated in a 16×16 array and the "half-active" $S_{1,1}$. 40

3.5 Normalized circularly polarized realized gain pattern of the element pattern, active element pattern, and scanned 16×16 array. 42

3.6 Design methodology of an antenna in a large array. 44

3.7 high frequency structure simulator (HFSS) model of the proposed patch antenna. (a) Isometric view. (b) Top view. (c) Side view. 45

3.8 Circularly polarized gain of the patch antenna under open boundary condition at 29.5 GHz under (a) left-hand circularly polarized (LHCP) and (b) right-hand circularly polarized (RHCP) excitation. 46

3.9 Periodic S-Parameters of the designed slot fed antenna in (a) magnitude and (b) smith chart. 47

3.10 (a) S_{11} and (b) S_{22} of the designed antenna as the length of slot 1 L_1 is varied. 47

3.11 (a) S_{11} and (b) S_{22} of the designed antenna as the radius of the upper patch R_1 is varied. 48

3.12 (a) S_{11} and (b) S_{22} of the designed antenna as the radius of the lower patch R_2 is varied. 48

3.13 Co-polarized and cross-polarized linear gain when (a) port 1 is excited and (b) when port 2 is excited. 49
3.14 (a) Active S-Parameters of the designed slot fed antenna. (b) Boresight AR across frequency. 50
3.15 Boresight circular gain across frequency when in (a) LHCP mode and (b) RHCP mode. 50
3.16 Total efficiency and radiation efficiency of the antenna across frequency. . . 51
3.17 Active S_{11} as the antenna is scanned along (a) $\phi = 0°$ and (b) $\phi = 90°$. . . 52
3.18 Active S_{22} as the antenna is scanned along (a) $\phi = 0°$ and (b) $\phi = 90°$. . . 52
3.19 Circularly polarized realized gain of both principle azimuthal planes at (a)(b) 27.5 GHz, (c)(d) 29.5 GHz, and (e)(f) 31 GHz. The left column is LHCP while the right is RHCP. 54
3.20 Block diagram of a 3-port network. 55
3.21 Proposed design methodology for the feed network. 57
3.22 Circuit model of the resistive power divider (RPD). 58
3.23 Circuit model of the lossless power divider (LPD). 59
3.24 Circuit model of the WPD. 60
3.25 (a) HFSS layout of the 1-to-2 WPD. (b) Simulated S-parameters of the 1-to-2 WPD. 61
3.26 HFSS layout of the 1-to-64 WPD network where each stage is connected using co-planar waveguide (CPWG). 61
3.27 S-parameters of the designed 1-to-64 WPD network. (a) Return losses. (b) Through. (c) Isolation from port 2. 62
3.28 Output reflection coefficient of the 1-to-64 WPD (a) with uniform excitation, (b) array tapering. 63
3.29 (a) HFSS layout of the 1-to-2 LPD. (b) Simulated S-parameters of the 1-to-2 LPD. 64
3.30 S-parameters of the 1-to-64 LPD network. (a) Return losses. (b) Through. (c) Isolation at port 2. 65
3.31 Output reflection coefficients of the 1-to-64 LPD network (a) with uniform excitation, and (b) with array tapering. 66

4.1 Block diagram of the radio frequency (RF) architecture of the 16×16 active PAA. 68

4.2 PCB layout of the designed active PAA. (a) Top side. (b) Bottom side. . . 69

4.3 Layer 10 of the direct current (DC) simulation of the antenna array. 71

4.4 Block diagram of a serial-peripheral-interface (SPI) connections from the connector to the BFICs. 72

4.5 Eye diagrams from transient simulations of the digital control signals are shown, where the yellow trace corresponds to the simulated waveform, the blue line indicates the minimum threshold for a logic-high level, and the orange line indicates the minimum threshold for a logic-low level. (a) Signal received at the connector when the furthest BFIC is driving the serial-data-in (SDI) net. (b) Signal received at the furthest BFIC when the connector is driving the serial-data-out (SDO) net. (c) Signal received at the furthest BFIC when the connector is driving the clock (CLK) signal. (d) Signal received at the furthest BFIC when the connector is driving the longest chip select (CS) signal. 74

4.6 Ansys Icepak thermal simulations of the antenna array (a) without any cooling devices, (b) with a case, heatsink and fan. 76

4.7 The designed aluminum case with heatsinks glued onto the back to cool the antenna array. 76

List of Tables

1.1 Planned LEO satellite systems [2]. 2

3.1 Scan loss across frequency and scan angles. 53

3.2 Circularly polarized realized gain across frequency and scan angles. 53

List of Abbreviations

5G 5th generation iii, 1

6G 6th generation iii, 1

AIP antenna-in-package viii, 28, 29

AR axial ratio viii, x, 3, 11, 12, 25–27, 32, 34, 35, 49, 50

BFIC beamforming integrated circuit iii, vii, viii, xi, 3, 15, 16, 19, 27–30, 32, 36, 43, 55, 60, 67–70, 72–75, 78

CLK clock xi, 72–74

CPWG co-planar waveguide x, 43, 60, 61

CS chip select xi, 72–74

DC direct current xi, 67, 70, 71

EIRP effective isotropic radiated power 10, 13, 14, 17, 18, 28, 30, 32, 34, 68

EM eletromagnetic iii, 5, 38, 42, 78

GEO geostationary orbit 2

HDI high-density interconnect ix, 27, 30, 36, 37

HFSS high frequency structure simulator ix, x, 38, 41, 45, 56, 60, 61, 64

Ka 26.5–40 GHz iii, 2, 3

LEO low earth orbit iii, xii, 2, 3, 36

LHCP left-hand circularly polarized ix, x, 11, 45, 46, 49–51, 54

LPD lossless power divider x, 58, 59, 63–66, 77

PAA Phased Array Antenna iii, vii, viii, xi, 2–5, 10, 15, 16, 19, 27, 28, 35, 42, 67–69, 77–79

PCB printed circuit board viii, ix, xi, 3, 15, 16, 19, 27, 28, 30, 33, 34, 36, 37, 60, 62, 67, 69, 75, 77

RF radio frequency xi, 3, 12, 27, 28, 30, 36, 38, 55, 67–70, 77, 78

RHCP right-hand circularly polarized ix, x, 11, 45, 46, 49–51, 54

RPD resistive power divider x, 58

RX receive 13, 28

SATCOM Satellite communication iii, 2, 3, 13, 35, 75, 77, 78

SDI serial-data-in xi, 72, 74

SDO serial-data-out xi, 72, 74

SPI serial-peripheral-interface xi, 68, 72

TX transmit 13, 28

WPD Wilkinson power divider ix, x, 28, 30, 32, 34, 59–64, 67, 69, 77

Chapter 1

Introduction

1.1 Motivation

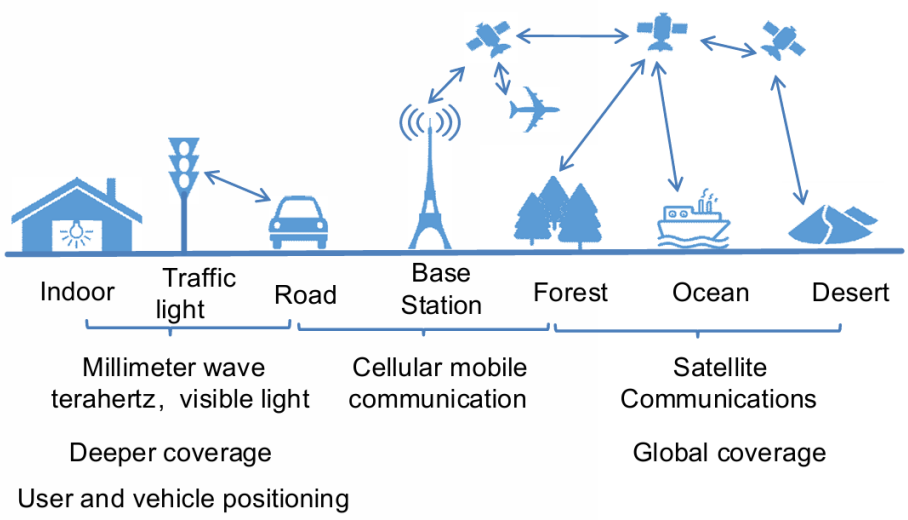


Figure 1.1: Areas of interest proposed for 6G coverage. [1]

The emergence of 5G and the development of the upcoming 6G standard have emphasized the integration of terrestrial and non-terrestrial networks. The 3rd Generation Partnership Project formally introduced Non-Terrestrial Networks as part of the 5G New Radio specification. Prior to 5G, terrestrial mobile networks provided coverage to only

about 20% of the world's landmass, corresponding to roughly 6% of the Earth's surface [1]. Modern terrestrial infrastructure largely relies on optical fiber backhaul between base stations, which is constrained by geography, terrain, and population density. Expanding this coverage through additional base stations and fiber deployment is not economically viable on a global scale. Applications that demand coverage include military operations, disaster recovery, maritime services, and in-flight connectivity.

To overcome these limitations, SATCOM has been proposed as a complementary solution, enabling user devices to communicate with satellites that route data through satellites before returning it to the end user. This approach has gained significant momentum in recent years, with initiatives from companies such as SpaceX, OneWeb, Telesat, LeoSat, and Kuiper [2]. An overview of the planned LEO constellations is provided in Table 1.1.

	OneWeb	Starlink	Telesat	LeoSat	Kuiper
Country	UK	USA	Canada	France	USA
Number of satellites	588	4425–42000	117	108	3236
Service band	Ku, Ka	Ku, Ka, V	Ka	Ka	Ka, V

Table 1.1: Planned LEO satellite systems [2].

Traditional SATCOM systems have relied on geostationary orbit (GEO) satellites positioned approximately 36,000 km above the equator. While these satellites appear stationary from Earth, they require high transmit power and introduce substantial latency, typically 500–600 ms for a round trip. To reduce latency and provide performance comparable to terrestrial fiber-optic infrastructure, LEO constellations have emerged. Operating at altitudes of roughly 2,000 km, LEO satellites lower round-trip delays to 30–50 ms while reducing power requirements. However, unlike geostationary satellites, they are in constant motion, necessitating rapid and continuous beam tracking. Mechanical steering of conventional satellite dishes is too slow for this purpose, motivating the adoption of electronically steerable PAAs.

To further increase data rates, 27.5–31 GHz has been allocated in the Ka-band for next-generation SATCOM services. Operating in this band provides large bandwidths and efficient spectrum utilization but also introduces higher free-space propagation path loss and atmospheric attenuation. These challenges demand high-gain antenna systems, which can be realized either through higher amplifier gain or by scaling up the size of PAAs. Consequently, the design of scalable, high-performance PAAs at Ka-band is central to enabling future SATCOM systems.

1.2 Problem Statement

SATCOM systems demand high data rates, reliable connectivity, and flexible beam steering to support modern applications such as broadband internet, remote sensing, and mobile communications. Achieving these requirements at Ka-band frequencies presents significant engineering challenges, since operation at high frequencies leads to increased free-space propagation path loss, which necessitates the use of high-gain antenna solutions.

Traditional satellite dishes can provide high gain, but they rely on mechanical movement, which may not meet the rapid tracking requirements of LEO satellites and introduces reliability concerns due to moving parts. To overcome these limitations, PAAs offer a means of electronically steering the beam, enabling rapid reconfigurability without mechanical components. By increasing the aperture size of these PAAs, the gain is also increased.

However, the design of such arrays introduces several interdependent challenges that must be carefully addressed. At the antenna element level, it is critical to achieve wide impedance bandwidth, low AR for circular polarization, and consistent radiation patterns across a broad scanning range. Equally important is the design of the feed network, which must distribute RF signals to the BFIC while maintaining precise amplitude, phase, and impedance matching. The integration of active components further increases complexity, as BFIC must be embedded within compact PCB stackups alongside their power and digital control interfaces, all while minimizing unwanted coupling and signal degradation.

Thermal management represents another significant constraint, since the heat generated by hundreds of active devices must be effectively dissipated to ensure reliable operation under practical environmental conditions. Finally, manufacturability and scalability impose additional requirements, as large arrays—sometimes consisting of more than one thousand elements—must be fabricated using commercially available PCB technologies in a manner that maintains performance while remaining cost-effective.

Consequently, there is a critical need for a comprehensive design methodology that simultaneously addresses antenna element design, feed network architecture, active component integration, thermal management, and manufacturability. This thesis aims to develop and demonstrate such a methodology, enabling high-performance, scalable, and manufacturable active PAA suitable for next-generation Ka-band SATCOM systems.

1.3 Thesis Organization

This thesis is organized as follows: Chapter 2 presents literature review on patch antenna structures, different array implementations, and large active PAA. Chapter 3 discusses the design methodology of the patch antenna and feed network. Chapter 4 discusses the design and analysis of the system architecture, power distribution, digital control, and thermal solution. Chapter 5 concludes this thesis and recommends future research directions based on the work presented.

Chapter 2

Background and Literature Review

2.1 Antennas and Phased Arrays

In wireless communication systems, the antenna serves as the essential interface between guided EM waves within transmission lines and radiated waves propagating through free space. The performance of an antenna directly impacts the efficiency of the communication link, determining how effectively power is transmitted into the surrounding medium or how incident signals are captured and converted back into electrical form. As noted by Balanis [3], an antenna is "the system component that is designed to radiate or receive electromagnetic waves," highlighting its fundamental role in shaping system-level parameters such as gain, polarization, and bandwidth.

PAAs extend this concept by combining multiple antenna elements in a coordinated configuration. Each element is typically connected to a phase shifter and amplifier, allowing the array to manipulate the amplitude and phase of each excitation. This enables electronic beam steering, offering a flexible and rapid way to direct radiation patterns without relying on mechanical movement. This capability enables rapid beam scanning, improved directivity, and adaptable radiation patterns.

2.1.1 Figures of Merits

To evaluate the effectiveness of an antennas and PAAs, certain figures of merits are typically used to characterize the effectiveness of the antenna or PAA. The following section lists and describes the metrics used in this thesis.

Directivity

The directivity is a fundamental parameter that quantifies how strongly an antenna concentrates its radiated power in a particular direction relative to an ideal isotropic radiator. Mathematically, it is expressed in equation 2.1 as the ratio of the maximum radiation intensity, $U_{\max}$, to the average radiation intensity over all directions. For an isotropic source, which radiates uniformly in every direction, $U = U_{\max}$, and hence the directivity is unity. In practical terms, directivity characterizes the theoretical focusing capability of an antenna, independent of losses. However, since no real antenna is perfectly lossless, directivity alone does not fully describe performance. Instead, it must be considered together with antenna efficiency to determine the actual gain.

$$D = \frac{U}{U_0} = \frac{4\pi U}{P_{rad}} \tag{2.1}$$

where

D : directivity (dimensionless)
U : radiation intensity (W/unit solid angle)
U_0 : radiation intensity of isotropic source (W/unit solid angle)
P_{rad} : radiated power (W)

Antenna Efficiency

Antenna efficiency, denoted as e_0, accounts for all mechanisms that reduce the power radiated relative to the power accepted by the antenna. As given in equation 2.2, this includes mismatch losses between the feed and the antenna (e_r), as well as intrinsic losses such as conductor losses (e_c) and dielectric losses (e_d). An antenna may exhibit very high directivity, but if the efficiency is poor, the effective radiated power will be significantly reduced. To minimize dielectric loss, careful selection of low-loss materials with low dissipation factors (D_f) is essential. In practice, e_c and e_d are often combined into a single quantity known as the radiation efficiency, which isolates material and conductor losses from impedance mismatch effects.

$$e_0 = \frac{P_{rad}}{P_{acc}} = e_r e_c e_d = e_r e_{rad} = (1 - |\Gamma|^2) e_{rad} \tag{2.2}$$

where

P_{acc} : accepted power (W)
e_0 : total efficiency (dimensionless)
e_r : mismatch efficiency (dimensionless)
e_c : efficiency due to conductor losses (dimensionless)
e_d : efficiency due to dielectric losses (dimensionless)
e_rad : radiation efficiency (dimensionless)
γ : reflection coefficient (dimensionless)

Gain

Antenna gain provides a more practical figure of merit by combining directivity with radiation efficiency, as defined in equation 2.3. Gain therefore represents the ability of the antenna not only to focus energy but also to radiate it effectively once losses are considered.

$$G(\theta, \phi) = e_{rad} D(\theta, \phi) \tag{2.3}$$

where

G : Gain (dimensionless)

To further account for mismatch between the antenna and its feeding structure, the concept of realized gain, or absolute gain, is introduced. Realized gain incorporates mismatch losses in addition to conductor and dielectric effects, providing the most complete measure of how much power is actually radiated in a given direction. From a system design perspective, realized gain is the most relevant metric, since it directly reflects the usable radiated power delivered to free space.

$$G_{abs}(\theta, \phi) = e_r G(\theta, \phi) = (1 - |\Gamma|^2) G(\theta, \phi) \tag{2.4}$$

where

G_{abs} : absolute gain (dimensionless)

Radiation Pattern and Array Factor

The radiation pattern of an antenna describes the spatial distribution of radiated power as a function of direction in the far-field region. Formally, it is characterized in terms of the electric and magnetic fields, or the power density, measured at a fixed distance from the antenna. The radiation pattern provides a comprehensive depiction of how an

antenna directs energy in 3-D space, typically expressed in spherical coordinates. Given the inherent 3-D nature of the pattern, it is common practice to visualize 2-D cross sections at a fixed azimuthal angle, ϕ, while varying the elevation angle, θ. An illustrative example is provided in Fig. 2.1, where the primary lobe is identified as the region of maximum radiation, occurring at $\theta = 0°$, bounded by nulls. The half-power beamwidth is defined as the angular region within the main lobe where the radiated power falls by 3 dB relative to the peak. Radiation in directions outside the main lobe is represented by minor or side lobes, which arise naturally from the Fourier transform characteristics of the antenna aperture; for a square aperture, this manifests as a sinc-function distribution in space.

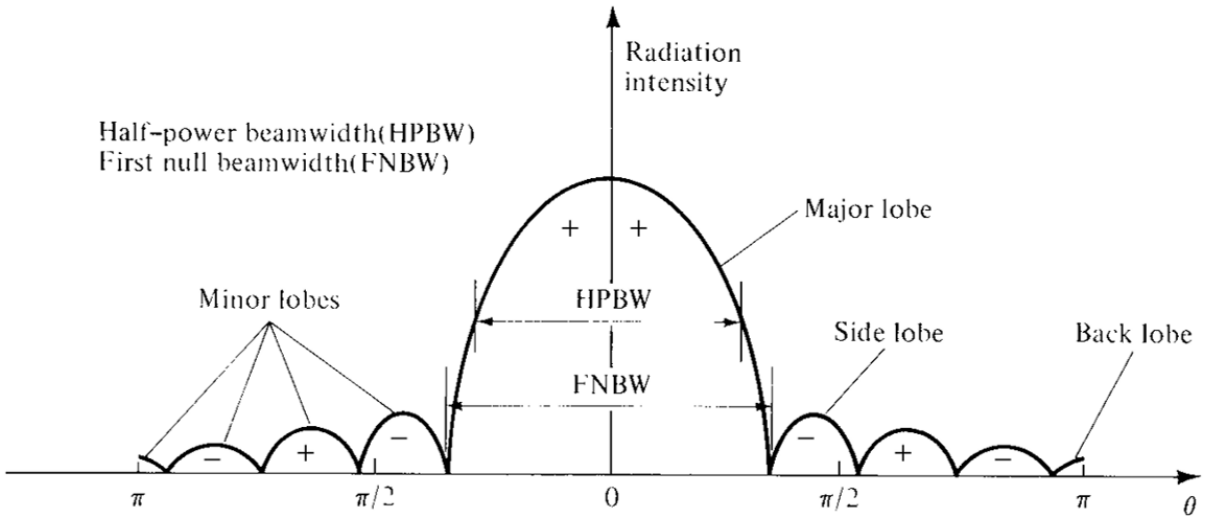
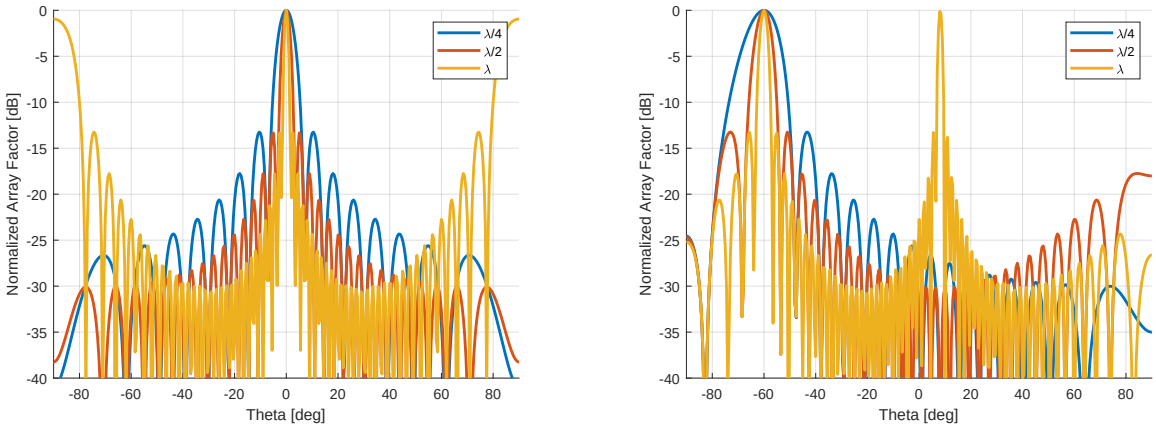


Figure 2.1: 2-D cut of a typical radiation pattern. [4]

In the context of antenna arrays, the overall radiation pattern is determined by the product of the individual element pattern and the array factor, as expressed in equation 2.6. The array factor provides a mathematical description of the directional behavior of the array based on the spatial configuration and relative excitation of the elements, assuming each source behaves as an isotropic radiator. Equation 2.5 defines the array factor as a summation over all elements, each weighted by its complex excitation a_n and accounting for its physical position, $\vec{r}_n$. The effect of element spacing on the array factor is demonstrated in Fig. 2.2a, where increasing the inter-element distance introduces grating lobes in the visible region that arise due to spatial undersampling of the aperture. To achieve beam steering, the excitation coefficients, a_n, are adjusted to introduce phase offsets that constructively reinforce the radiation in a desired direction (θ_0, ϕ_0). Fig. 2.2b illustrates a steered array factor at $\theta = -60°$ for various element spacings. When the spacing exceeds



(a) (b)

Figure 2.2: The array factor is plotted varying the spacing between antenna elements at (a) boresight and (b) $\theta = -60°$.

half a wavelength, $\lambda/2$, undesired grating lobes emerge, exemplified by the dual peaks at $\theta = -60°$ and $\theta = 8°$, which divert energy into unintended directions. It is important to note that the array factor also combines in back radiation and is dependent on the antenna radiation pattern to suppress the back radiation.

$$AF(\theta, \phi) = \sum_{n=1}^{N} a_n e^{j\frac{2\pi}{\lambda}\hat{r}\cdot\vec{r_n}} = \sum_{n=1}^{N} a_n e^{j\frac{2\pi}{\lambda}[x_n sin(\theta)cos(\phi)+y_n sin(\theta)sin(\phi)]} \tag{2.5}$$

where

AF : array factor (dimensionless)
N : total number of antennas
a_n : excitation weight at the n^{th} antenna
$\hat{r}$: directional unit vector
$\vec{r_n}$: position of the n^{th} antenna in spherical coordinates
$\vec{x_n}$: position of the n^{th} antenna in the x-axis in cartesian coordinates
$\vec{y_n}$: position of the n^{th} antenna in the y-axis in cartesian coordinates

$$E_{array}(\theta, \phi) = E_{element}(\theta, \phi)AF(\theta, \phi) \tag{2.6}$$

where

E_{array} : radiation pattern of the array
$E_{element}$: radiation pattern of the antenna element

Scan Loss

Since the element pattern is not isotropic, as the PAA steers its beam away from boresight ($\theta = 0°$), there is a reduction in gain characterized as scan loss. This reduction arises because the effective aperture of the array diminishes as the steering angle approaches $\theta = 90°$, ultimately reaching zero at the horizon. In an ideal PAA, the scan loss follows a $\cos\theta$ dependence, reflecting the geometric projection of the aperture in the steering direction.

From a system perspective, scan loss is a critical consideration as it directly impacts the effective isotropic radiated power (EIRP) in transmitters and the antenna gain-to-noise-temperature ratio in receivers for off-boresight angles. In practical terms, the magnitude of scan loss at extreme steering angles informs the design requirements at boresight.

Scan Blindness

In some cases, scan blindness can also be observed as the beam is steered, this is a phenomenon characterized by the inability of the PAA to effectively radiate or receive power in certain scan directions. Despite appropriate phase settings intended to steer the beam, the antenna fails to form a usable radiation pattern at these angles. The primary mechanism underlying scan blindness is the excitation of surface waves, which propagate laterally within the substrate rather than radiating into free space.

Surface waves are particularly problematic when the substrate between the antenna elements and the ground plane supports waveguide-like propagation. Factors that exacerbate this effect include substrates with high dielectric constants, increased substrate thickness, and densely packed planar antenna layouts. In such configurations, energy intended for radiation is instead trapped in the substrate, leading to nulls or severe reductions in gain at specific scan angles. Consequently, careful consideration of substrate properties and array geometry is essential to mitigate scan blindness and maintain reliable scanning performance across the intended angular range.

Polarization

Polarization characterizes the temporal evolution of the electromagnetic field vector at a fixed observation point and is a critical consideration in antenna design and system performance. Antennas are generally classified according to their polarization, with linear and circular polarizations being the most commonly employed.

For linearly polarized waves, the electric field vector oscillates along a straight line within a plane orthogonal to the direction of propagation. The orientation of this line determines the polarization designation: if aligned along the $\phi = 0°$ plane, the wave is considered vertically polarized, whereas alignment along $\phi = 90°$ corresponds to horizontal polarization. Misalignment between the transmitting and receiving antenna polarizations results in reduced power transfer, highlighting the importance of polarization matching in system design.

Circular polarization, by contrast, provides greater robustness against polarization mismatch because the electric field rotates over time, thereby providing components along both horizontal and vertical axes simultaneously. The sense of rotation defines the polarization as either LHCP or RHCP. Conceptually, circular polarization can be viewed as the superposition of two orthogonal linear polarizations with a 90° phase offset. This phase offset produces an electric field vector that traces a circular trajectory in the observation plane, ensuring consistent power reception irrespective of the relative orientation of the antennas.

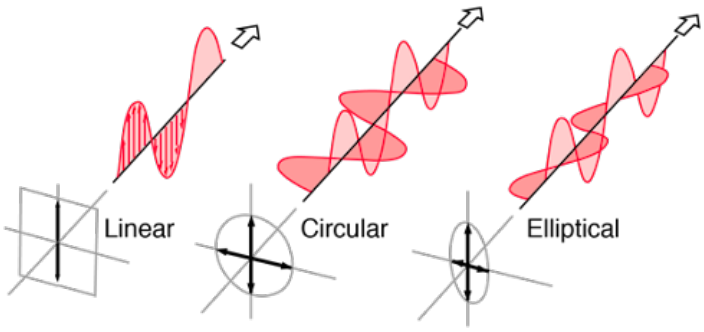


Figure 2.3: Example of traveling electromagnetic waves in linear, circular and elliptical polarization (left to right) [5]. At the end of each wave shows what is observed over time at a fixed observation point.

Axial Ratio

AR is a fundamental metric used to quantify the quality of circular polarization. It is defined as the ratio of the major to minor axis of the polarization ellipse observed, effectively describing the degree to which the polarization deviates from an ideal circle. An axial ratio of 1 (0 dB) corresponds to perfect circular polarization, where the major and minor axes are equal in magnitude.

$$AR = \frac{E_{major}}{E_{minor}} \tag{2.7}$$

In practical systems, particularly in dual-linear polarized antennas, the major and minor axes typically align with the horizontal and vertical polarization components. The AR serves as a key performance indicator in communication systems, as deviations from ideal circular polarization can reduce the effective power transfer between transmitting and receiving antennas. For satellite and wireless communications, a commonly accepted standard is an AR of less than or equal to 3 dB, ensuring sufficiently circular polarization to maintain system reliability and minimize polarization mismatch losses.

Load Modulation and Mutual Coupling

In RF systems, the behavior of antennas is commonly characterized using S-parameters, which describe the reflection and transmission properties of multi-port networks. For single-port antennas, the return loss, $S_{1,1}$, provides a straightforward measure of impedance mismatch. However, in multi-port antennas, the reflection at one port is influenced by the excitations of the other ports, a phenomenon referred to as load modulation or active loading.

To mitigate the effects of load modulation, antenna elements can be designed with high isolation, thereby reducing the influence of other ports within the antenna. In the context of antenna arrays, load modulation is not limited to interactions within a single antenna; it also arises from mutual coupling with adjacent antennas. Consequently, load modulation can significantly affect reflection efficiency and, in certain cases, the AR of the radiated fields.

Mathematically, load modulation is captured by the active return loss, as shown in equation 2.8, which incorporates the S-parameters, $S_{i,j}$, of the N-port network. The active return loss represents the reflection at a given port considering the combined effect of all excitations in the array. As the beam is steered, the excitation weights of the other antennas vary, altering the active return loss. Therefore, analysis of the active return loss provides critical insight into phenomena such as scan blindness and scan loss.

$$Active\ S_{i,i} = \frac{\sum_{n=1}^{N} S_{i,n} a_n}{a_i} \tag{2.8}$$

Bandwidth

The bandwidth of an antenna is generally defined as the frequency range over which the antenna maintains performance characteristics that satisfy the design specifications. For many canonical antennas, such as a half-wavelength dipole, the resonance condition is satisfied at a single frequency, corresponding to optimal impedance matching and radiation pattern characteristics. As the operating frequency deviates from this center frequency, these performance metrics deteriorate. Nevertheless, an antenna may still meet the system requirements over a finite range of frequencies, which is then identified as the operational bandwidth. In practice, a common specification for acceptable impedance matching is a reflection coefficient of $S_{11} \leq -10$ dB.

$$BW = \frac{f_h - f_l}{f_c} \tag{2.9}$$

Impedance bandwidth is often expressed as a relative percentage with respect to the center frequency, as given in equation 2.9. In the context of SATCOM, particularly for ground terminals operating in the Ka-band, two frequency ranges are of primary interest: 17.7–21.2 GHz for the receive (RX) band and 27.5–31 GHz for the transmit (TX) band. For these applications, the RX band requires a relative bandwidth of approximately 18%, whereas the TX band requires approximately 14%.

Effective Isotropic Radiated Power

EIRP is a measure of the apparent power radiated by an antenna system in the direction of its maximum gain. It is defined as the product of the power delivered to the antenna and the antenna gain relative to an isotropic radiator. Expressed in logarithmic terms, EIRP can be written as seen in equation 2.10

$$EIRP\ (dBW) = P_{in}\ (dBW) + G_{ant}\ (dBi) \tag{2.10}$$

where P_{in} is the power sent into the antenna, and G_{ant} is the realized gain of the antenna aperture. Increasing either the input power or the aperture gain results in a higher EIRP, thereby enhancing the effective radiated strength of the transmitting system.

Output 1 dB Compression Point

The output 1 dB compression point (OP_{1dB}) is a parameter used to characterize the linearity of an amplifier. It is defined as the output power level at which the amplifier gain decreases by 1 dB from its small-signal gain due to nonlinear compression. At low input powers, the amplifier operates in its linear region, such that the output power increases proportionally with the input power according to the small-signal gain. As the input power increases, the amplifier approaches saturation and the gain begins to compress. The OP_{1dB} marks the point at which this deviation becomes 1 dB, as expressed in equation 2.11.

$$OP_{1dB} = P_{in} + (G - 1), \tag{2.11}$$

where OP_{1dB} is the output power at the 1-dB compression point, P_{in} is the corresponding input power, and G is the small-signal gain of the amplifier.

The OP_{1dB} provides a practical measure of the maximum usable output power of the amplifier in its linear operating region. This parameter is often used in conjunction with the EIRP to determine the maximum transmitted power of a system. In communication systems with modulated signals, amplifiers are typically operated with some back-off from the OP_{1dB} so that the peak power of the signal reaches the OP_{1dB}, while the average power remains lower, preserving linearity and minimizing distortion.

2.2 Literature Review

2.2.1 Patch Antennas

The patch antenna is a prevalent choice in PAAs due to its inherently low-profile structure, which allows seamless integration onto PCBs. This compact form factor is particularly advantageous in active PAAs, where additional PCB layers are often required to route power and digital control signals to BFICs. A patch antenna consists of a metallic patch of length $\lambda_g/2$ positioned over a ground plane, effectively functioning as a $\lambda_g/2$ open-circuit stub. Radiation is primarily generated by the fringing fields at the edges of the patch, which combine in phase to produce the far-field radiation. A well-known limitation of the patch antenna arises from its $\lambda_g/2$ dependence, which naturally results in a narrow impedance bandwidth. The following section discusses implementations of patch antennas in arrays in the literature.

Edge Fed Patch Antenna

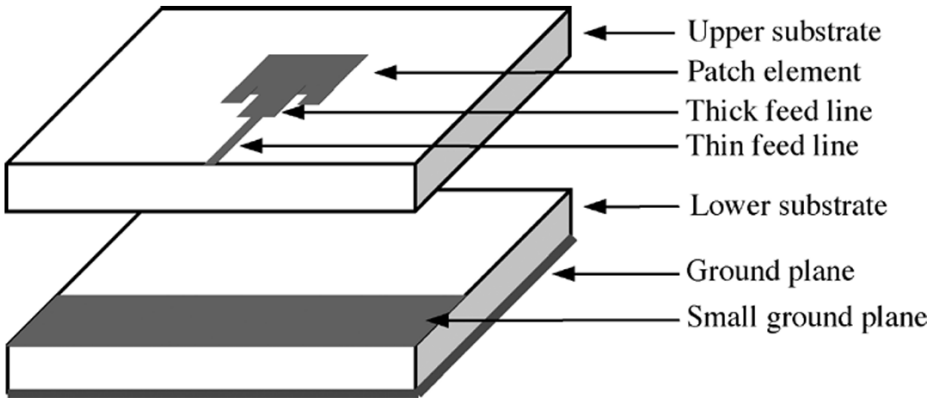


Figure 2.4: Typical structure of an edge fed patch antenna which includes a patch, a ground layer beneath it, and a microstrip line fed directly to the patch. [6]

The first feeding mechanism, the edge-fed method, is the simplest and intuitive. In this approach, a microstrip line directly connects to the edge of the patch, as illustrated in Fig. 2.4 and discussed in [6]. The edge-fed technique dates back to the 1970s [7] and has been demonstrated to support linearly polarized patch antennas. For instance, [6] achieved a 4% impedance bandwidth at 5 GHz by employing a thick dielectric substrate.

However, thicker substrates necessitate wider microstrip feed lines, which can introduce additional challenges. Specifically, maintaining the feed on the same layer as the patch may result in spurious radiation between the feed line and the patch. Furthermore, in active PAA implementations, the BFICs are typically placed on the bottom side of the PCB to avoid disturbing the antenna radiation pattern. Consequently, the feed network must also be routed to the bottom layer, introducing additional design complexity that must be carefully managed to prevent performance degradation.

Probe Fed Patch Antenna

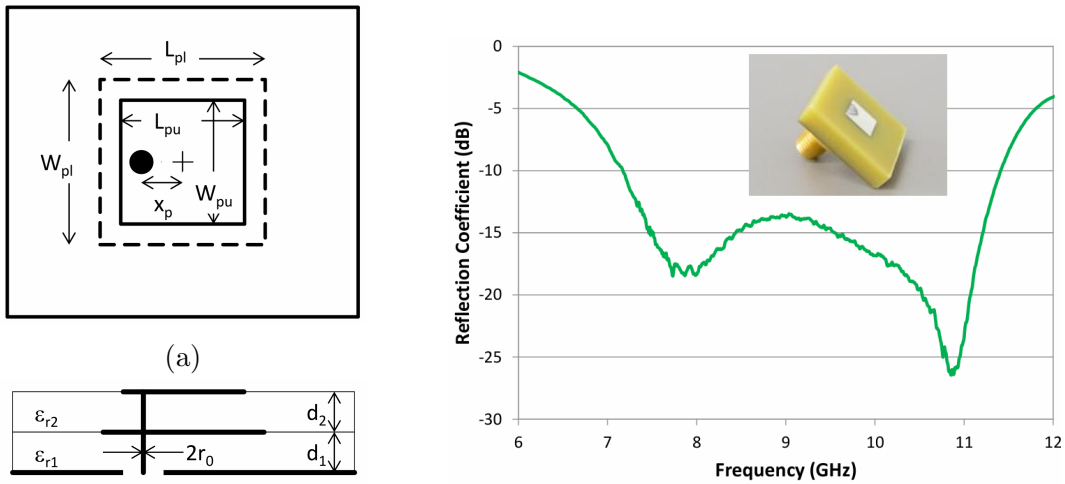
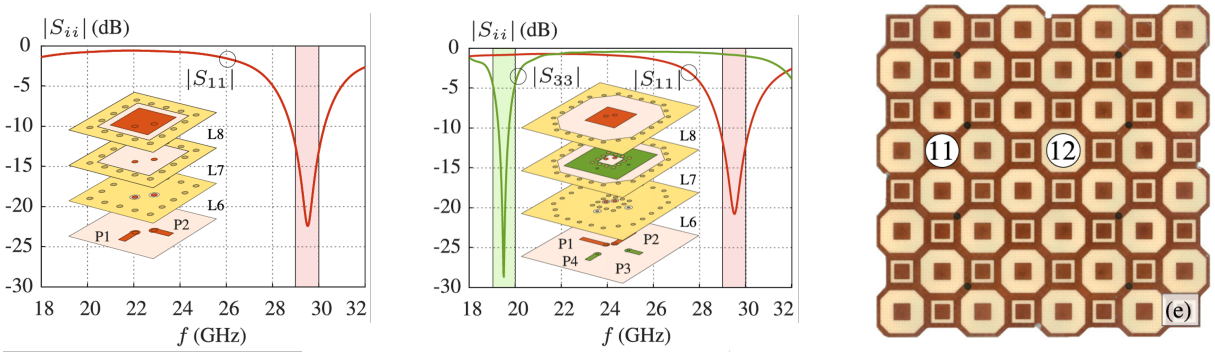


Figure 2.5: The antenna designed in [8], where (a) shows the top view and (b) shows the side view and the stack-up. (c) shows the measured reflection coefficient of the antenna.

Probe-fed patch antennas offer an alternative to the traditional edge-fed design by replacing the microstrip feed with a probe that connects directly to the patch from beneath the antenna ground layer. This approach allows the feed network to be isolated from the radiating element, reducing spurious coupling and undesired radiation. The vertical connection is typically realized using vias in multilayer PCBs or other laminar circuit board technologies, which provide a conductive path from the bottom layer to the patch.

An illustrative example of this technique is presented in [8], where a linearly polarized stacked patch antenna was designed and measured. The antenna, depicted in Fig. 2.5, consisted of three layers: two patch layers and a ground layer on the bottom. A cutout

in the ground plane allowed the probe to pass from the top layer to the bottom. This configuration achieved a measured impedance bandwidth of 44% at 9 GHz. The substantial bandwidth was attributed to both the use of a thick substrate and the addition of a second patch, which introduced a second resonance to extend the overall bandwidth. Further demonstrations of linearly polarized probe-fed patch antennas at 40 GHz and 60 GHz are provided in [9, 10], where bandwidths of 12% and 11% were achieved, respectively. In [10], the authors implemented a 4×8 array with dummy elements along the edges, achieving a maximum EIRP of 53 dBm at boresight, which decreased to 50 dBm at $\theta = 30°$.



(a) (b) (c)

Figure 2.6: (a) Dual linear polarized probe fed patch antenna at 29.5 GHz and (b) dual band version at 19.5 GHz and 29.5 GHz in [11]. (c) interleaved array configuration of antennas in (a) and (b) used in [11].

To support dual polarization, probe-fed designs can incorporate two probes to independently excite orthogonal polarizations. For instance, [11] designed dual-linear polarized patch antennas by symmetrically arranging the patches along both polarization planes. Two antennas were developed: one operating at 29.5 GHz, and a dual-band version covering 19.5 GHz and 29.5 GHz. The 29.5 GHz design, shown in Fig. 2.6a, achieved a 5% impedance bandwidth. The dual-band antenna, illustrated in Fig. 2.6b, added a second resonant patch for the lower frequency and two additional probes to excite it. This configuration maintained a 5% bandwidth at 29.5 GHz and introduced a 3% bandwidth at 19.5 GHz.

The antennas were organized into an interleaved array configuration, forming an 8×8 array at 29.5 GHz and an 8×4 array at 19.5 GHz, as shown in Fig. 2.6c. The transmitter array exhibited a scan loss of 1.9 dB and 2.6 dB at $\pm 40°$ along the H-plane and E-plane, respectively. At wider scan angles, performance degraded by up to 7 dB at $\pm 60°$, with

grating lobes appearing due to large element spacing ($0.55\lambda_0$). The large spacing also generated surface waves, resulting in scan blindness at $-55°$ on the E-plane. Despite these limitations, the array achieved an EIRP of 50.4 dBm at the 1 dB compression point at boresight with cross-polarization better than 20 dB. The receiver array exhibited similar scanning performance, with a scan loss of 1.9 dB at $\pm 40°$ on the H-plane and 2.1 dB on the E-plane, although grating lobes and surface wave effects were less pronounced due to slightly smaller element spacing ($0.52\lambda_0$).

Proximity Fed Patch Antenna

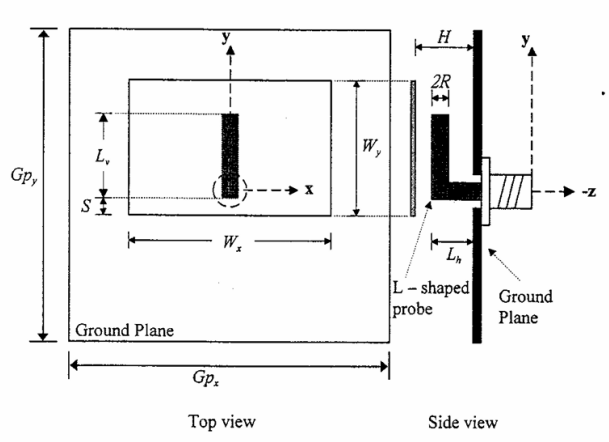
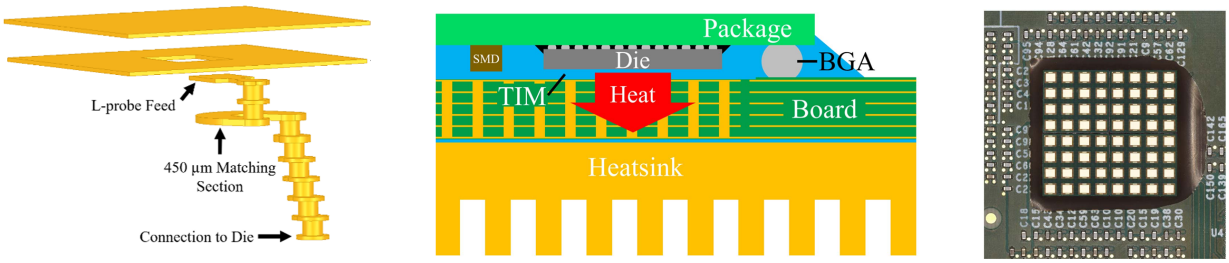


Figure 2.7: Patch antenna fed by an L-shaped probe introduced in [12].

The proximity feed is where an L-shaped probe capacitively couples to the patch rather than being directly connected. This technique suppresses the inherent inductive behavior of a direct probe and can improve bandwidth. The concept was first introduced by [12] in 2000. As illustrated in Fig. 2.7, the patch features an open-ended stub beneath it that is connected to a probe. Using this approach, the authors demonstrated a single-element antenna with a 36% impedance bandwidth at 4.5 GHz and a cross-polarization level of -15 dB. To further reduce cross-polarization and enhance gain, a 1×2 array was formed by mirroring the antennas along the x-axis with $\lambda/2$ spacing. This configuration increased the gain from 6.5 dBi to 9 dBi while reducing the cross-polarization to -20 dB.

At higher frequencies, [13] designed a linearly polarized stacked patch antenna at 70 GHz, utilizing stacked microvias to form the probe section of the feed. An additional patch was introduced to extend the bandwidth, resulting in a 13% impedance bandwidth.



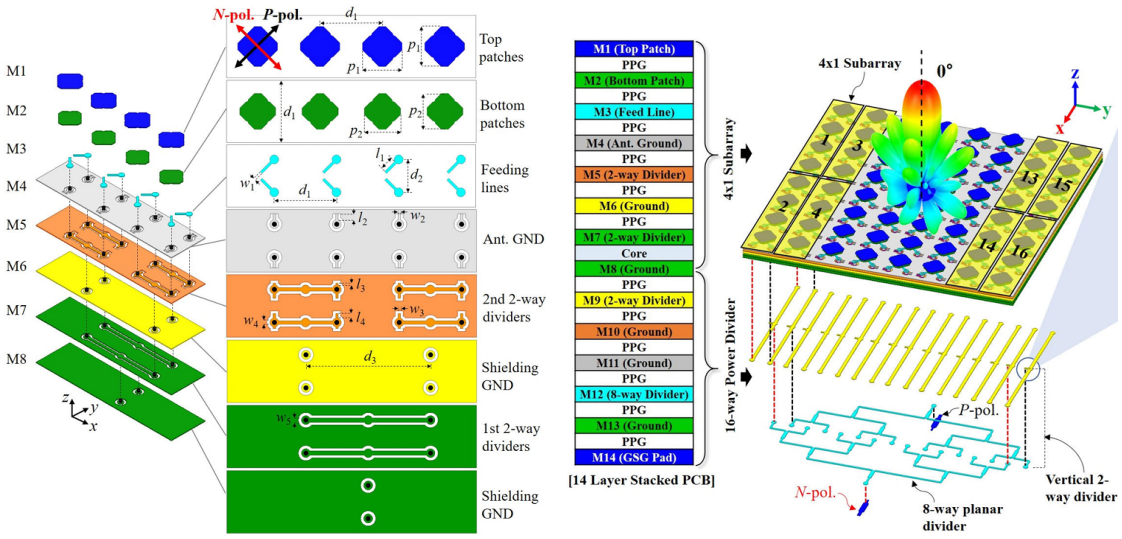
(a) (b) (c)

Figure 2.8: (a) Linearly polarized proximity-fed patch antenna at 70 GHz. (b) Full stack-up of the active PAA, showing the packaged antenna and BFICs mounted on the carrier board with the cooling solution. (c) Four 4×4 subarrays combined to form an 8×8 array [13].

An 8×8 array was constructed from four 4×4 subarrays, each packaged and mounted on a carrier board with thermal underfill to conduct heat from the die to the heatsink, as shown in Fig. 2.8c. The array achieved a scan loss of 5 dB at $\pm 60°$ along the H-plane; however, the E-plane patterns exhibited distortions caused by surface waves interacting with the carrier PCB.

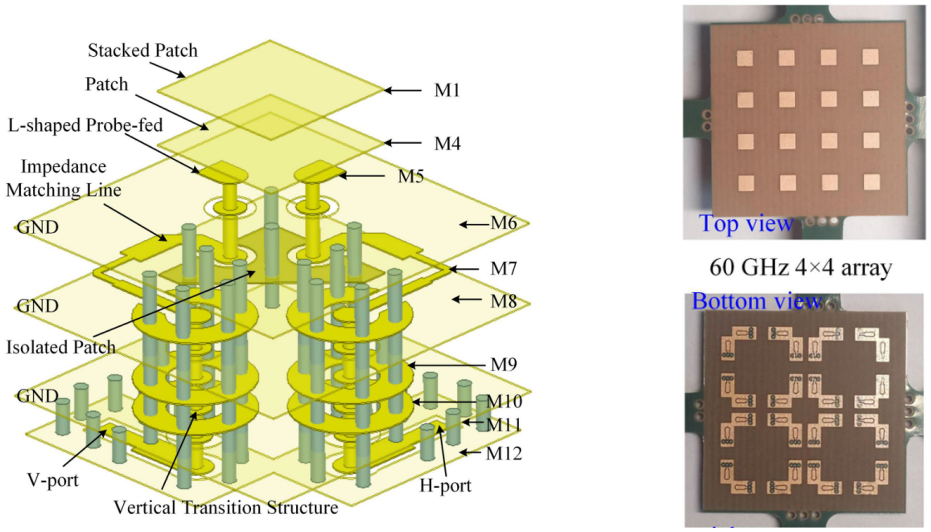
For dual-polarization operation, [14] designed a symmetrical proximity-fed stacked patch antenna at 140 GHz, achieving a bandwidth of 17% with port isolation better than -13 dB across the band. To form an 8×8 array, a 1×4 subarray was duplicated 16 times. Each 1×4 subarray incorporated two 1-to-4 vertical dividers, one per polarization, as shown in Fig. 2.9a. To construct the full 8×8 array, additional vertical dividers were used to combine two 1×4 subarrays into a 1×8 subarray, which were then interconnected through an 1-to-8 planar T-junction divider (Fig. 2.9b). This network generated a fixed beam at boresight ($\theta = 0°$) with a measured gain of 17.4 dBi, a sidelobe level of -13.9 dB, and cross-polarization of -22.6 dB. A modified divider network with additional delay lines enabled fixed beam steering to $\theta = 55°$, yielding a gain of 13.5 dBi with a sidelobe level of 5.9 dB and cross-polarization of -14.7 dB.

[15] implemented a grounded shielding structure between the feeds of both polarization (Fig. 2.10), improving isolation from -15 dB to -20 dB. Their antenna achieved a 24% bandwidth at 60 GHz. Simulations of a 4×4 array indicated scan loss of 3 dB at $\theta = \pm 30°$ along the E-plane and $\theta = \pm 37°$ along the H-plane. The array demonstrated a simulated peak gain of 18.1 dBi at boresight at 66 GHz, while measured single elements achieved 5.8 dBi at 55 GHz; scanning performance was not reported.



(a) (b)

Figure 2.9: (a) Dual linearly polarized proximity-fed patch antenna at 140 GHz arranged in a 1×4 subarray with two 1-to-4 vertical dividers. (b) Sixteen 1×4 subarrays combined to form an 8×8 array, including the two 1-to-8 dividers [14].

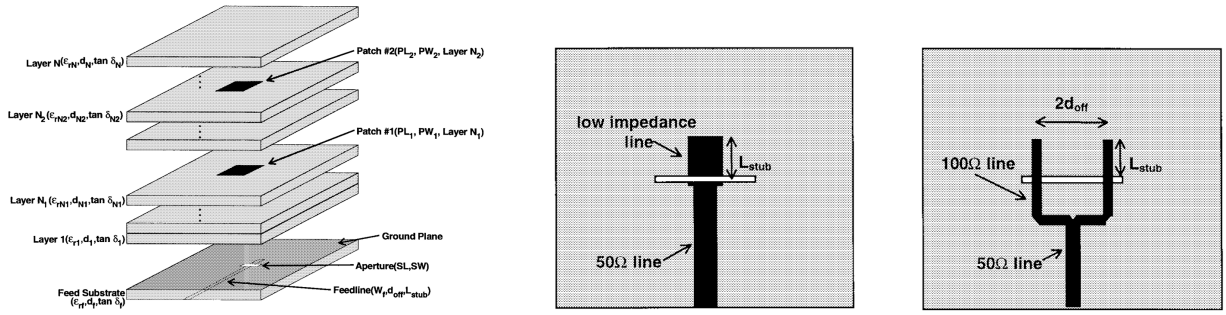


(a) (b)

Figure 2.10: (a) Dual linearly polarized proximity fed patch antenna with a shielding structure at 60 GHz and the (b) fabricated 4×4 array in [15].

Aperture (Slot) Fed Patch Antenna

Aperture coupling represents another form of non-direct contact feeding, where the patch is excited through a slot etched in the ground plane. A microstrip line or stub on the opposite side of the ground couples energy through the aperture into the radiating element. This configuration eliminates the need for vertical vias or probes, thereby simplifying fabrication and offering improved mechanical reliability. Moreover, the thin slot geometry typically produces purer radiation patterns with reduced cross-polarization levels [16]. However, the approach is more sensitive to alignment tolerances since precise registration between the feed slot and patch is required during fabrication.

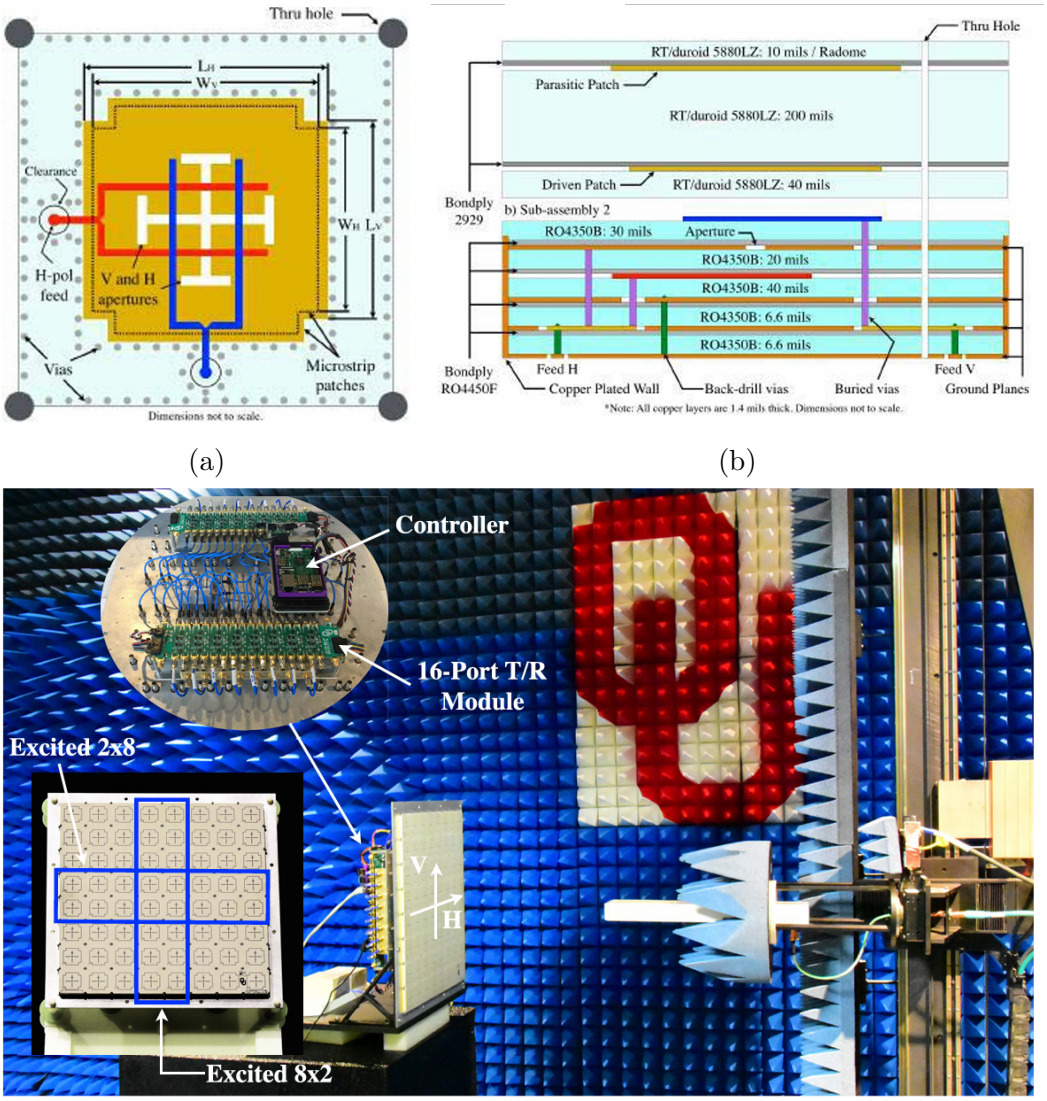


(a) (b) (c)

Figure 2.11: (a) Stack-up of proposed linear polarized aperture fed stacked patch antenna. The two methods of feeding the slot are by using a (b) low impedance stub or by using (c) two 100Ω stubs joined together by a power combiner [17].

An early demonstration of aperture coupling was presented by [17], who designed a linearly polarized stacked patch antenna comprising two patches excited by a slot in the ground plane. As shown in Fig. 2.11a, the slot itself functioned as an additional resonator, extending the operational bandwidth of the antenna. Two different feeding strategies were investigated: (1) a single low-impedance stub (Fig. 2.11b), and (2) two 100 Ω stubs combined through a T-junction to achieve 50 Ω matching (Fig. 2.11c). The former configuration was ultimately selected, yielding a fabricated antenna with a measured bandwidth of 69% spanning 5.07–10.38 GHz. The antenna also achieved a front-to-back ratio of 8–14 dB and a peak gain of 8.5 dBi.

The technique has also been extended to produce dual-polarized patch antennas. In [18], a cross-slot geometry was employed that was fed by two forks, as illustrated in Fig. 2.12a and Fig. 2.12b. This design achieved 18% bandwidth at 2.8 GHz with port-to-port isolation better than -48 dB across the band. An 8×8 array was fabricated and measured in an



(a) (b)

(c)

Figure 2.12: (a) Dual linearly polarized cross slot fed patch antenna at 2.8 GHz fed with two fork feeds. (b) Stack-up of the antenna showing the location of each component in the stack-up in [18]. (c) The 8×8 array as well as the measurement setup.

anechoic chamber, where only 2×8 elements per polarization were excited (Fig. 2.12c). The measured scan performance confirmed stable operation, with sidelobe levels maintained below −13 dB and cross-polarization suppressed below −40 dB when scanning from −45° to 45° along both the E-plane and H-plane.

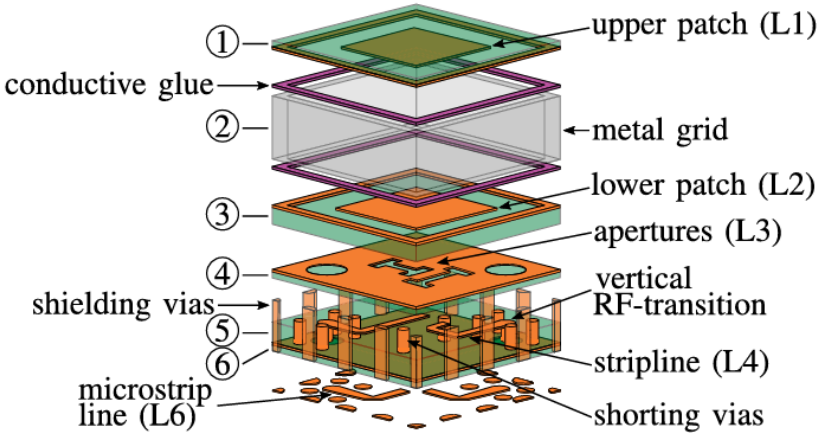


Figure 2.13: Dual linear polarized stacked patch antenna using offset orthogonal H-shaped slots with added shorting vias to improve isolation between feeds. [19]

Alternative methods for achieving dual polarization were demonstrated in [19,20], where the slots were offset from the center rather than overlapping in a cross configuration. The offset slots (Fig. 2.13) break the symmetry between polarizations, preventing the use of fork feeding and limiting the design to single-stub feeds. To maintain the electrical length while reducing the horizontal slot size, H-shaped slots were introduced, effectively balancing bandwidth and compactness. In [20], shielding vias were further incorporated in the stripline feed layer to suppress unwanted coupling, improving port isolation from −25 dB to −50 dB. The fabricated antenna achieved a 21.8% bandwidth at 27 GHz. By contrast, [19] reported a 10% bandwidth at 29 GHz with −25 dB isolation. To evaluate scan performance, the authors constructed an 11 × 11 array, exciting only the central element while terminating all others in 50 Ω. The measured radiation patterns indicated a scan loss of approximately 5 dB at $\theta = \pm 60°$, with a boresight peak gain of 5.3 dBi at 31 GHz. This approach offers an advantage over the fork feed method, as it uses a single layer, whereas the fork-feed method requires two layers to accommodate dual polarization.

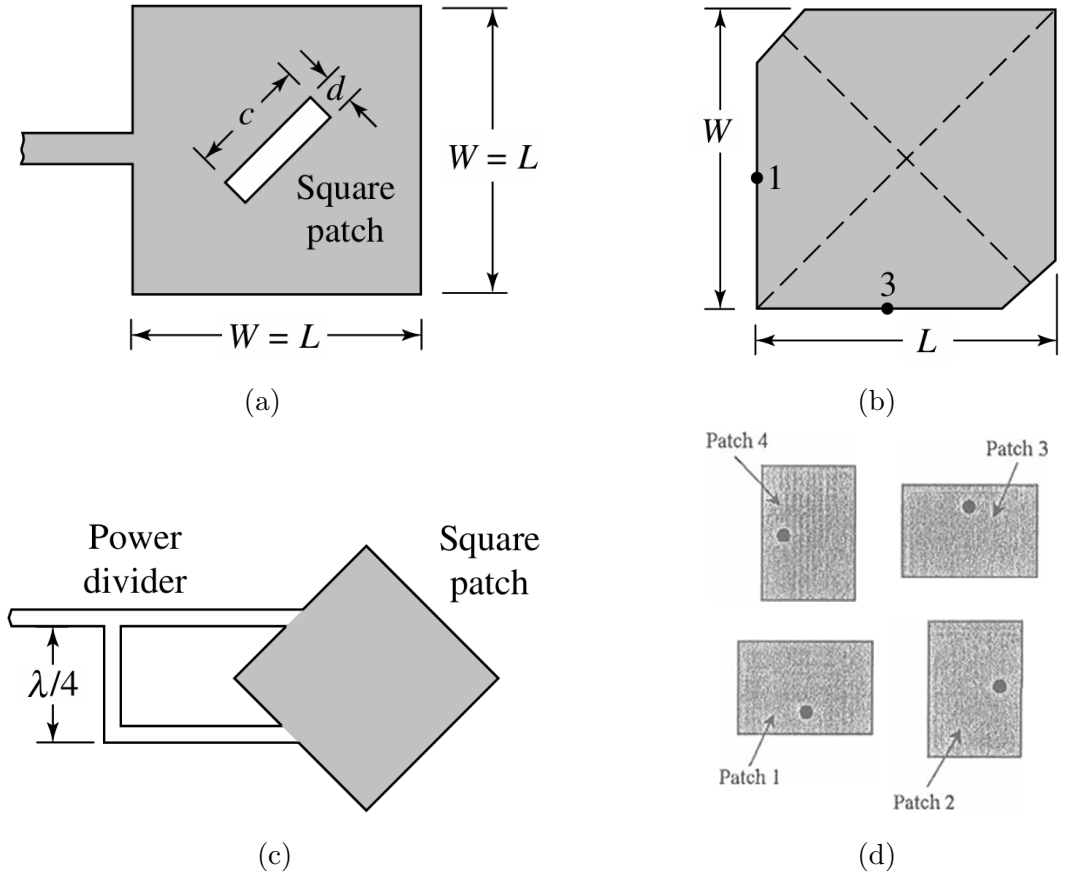
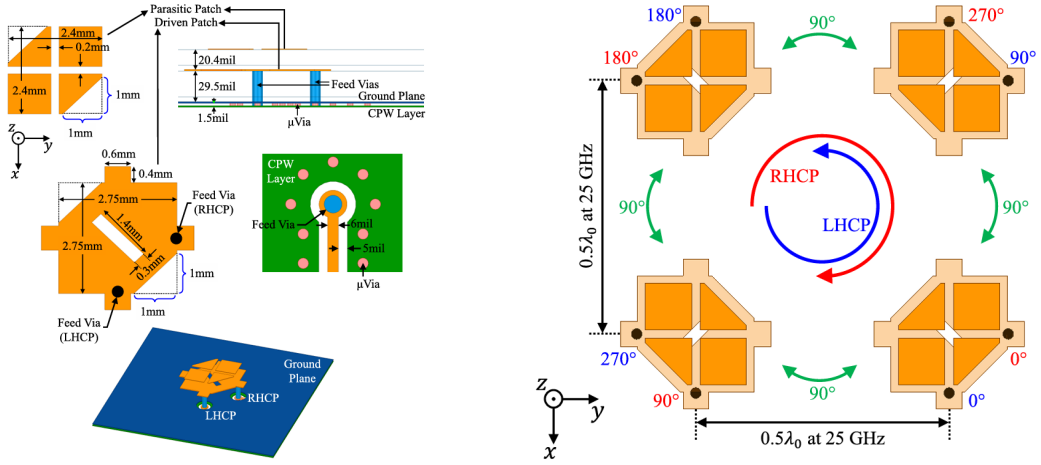


Figure 2.14: (a) Single feed square patch with a diagonal slot to generate circular polarization [4]. Single feed square patch with truncated corners to generate circular polarization [4]. (c) Dual feed patch to generate circular polarization [4]. (d) Sequentially rotated antennas to generate circular polarization [16].

Circular Polarization with Patch Antennas

Three primary approaches are commonly employed to achieve circular polarization in patch antennas. The first approach involves designing the antenna to be inherently circularly polarized. For patch antennas, this typically requires geometrical modifications to the patch itself, as illustrated in Fig. 2.14a and Fig. 2.14b. These modifications are intended to couple the orthogonal linear polarization modes with a 90° phase offset, thereby producing circular polarization. An example of such a design is presented in [21], where the antenna incorporates both a diagonal slot and truncated corners, as shown in Fig. 2.15a. While this method is effective in generating circular polarization, it generally suffers from a narrow AR bandwidth. This limitation arises from the frequency-dependent nature of the 90° phase offset between the two orthogonal modes. Specifically, in [21], the antenna achieved a 3 dB AR bandwidth of only 3% at 32 GHz, despite an impedance bandwidth of 64%. In addition, the AR is not reconfigurable and is fixed based on the geometry of the antenna.



(a) (b)

Figure 2.15: (a) Patch antenna with truncated corners. (b) 2×2 subarray of patch antennas with truncated corners oriented in with sequential rotation to improve AR. [21]

The second method relies on manipulating the relative orientation of antennas within an array. In this technique, each antenna in a subarray is sequentially rotated, as shown in Fig. 2.14d, where the antennas are rotated 90° clockwise in a 2×2 array. This configuration ensures that two antennas excite the vertical polarization while the other two excite the horizontal polarization. By mirroring the antennas with the same polarization, polarization impurities can partially cancel, improving the AR at boresight. In [21], this method was

combined with corner truncation and a diagonal slot on the patch to form an 8×8 array from the 2×2 subarray, achieving a measured boresight AR below 3 dB at 24 GHz and 26.5 GHz. While effective at boresight, this technique exhibits degradation as the beam is scanned, since the polarization cancellation is no longer maintained. For instance, the 3 dB AR range was limited to $\theta = \pm 37°$ at 26 GHz in [21].

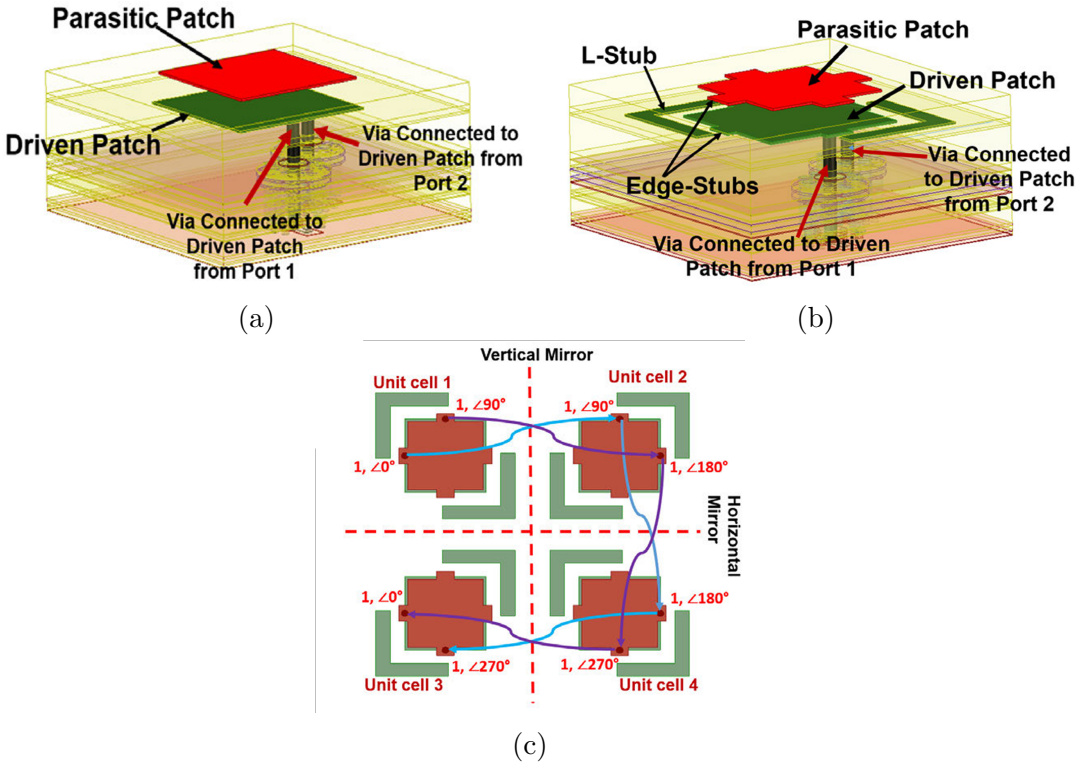


Figure 2.16: (a) Probe fed stacked patch antenna (b) with L stubs in [22]. (c) 2×2 mirrored antennas used in [22].

The third approach to achieving circular polarization involves designing the antenna to be dual linearly polarized and introducing the 90° phase offset through the feed network, as illustrated in Fig. 2.14c. This method offers the advantage of adjustable AR performance, allowing for fine tuning of the circular polarization. However, this flexibility comes at the cost of increased complexity in the feeding structure. For optimal performance, the antenna must not only support dual polarization, but the two feeds must maintain sufficient isolation to prevent load modulation between ports. An example of this implementation

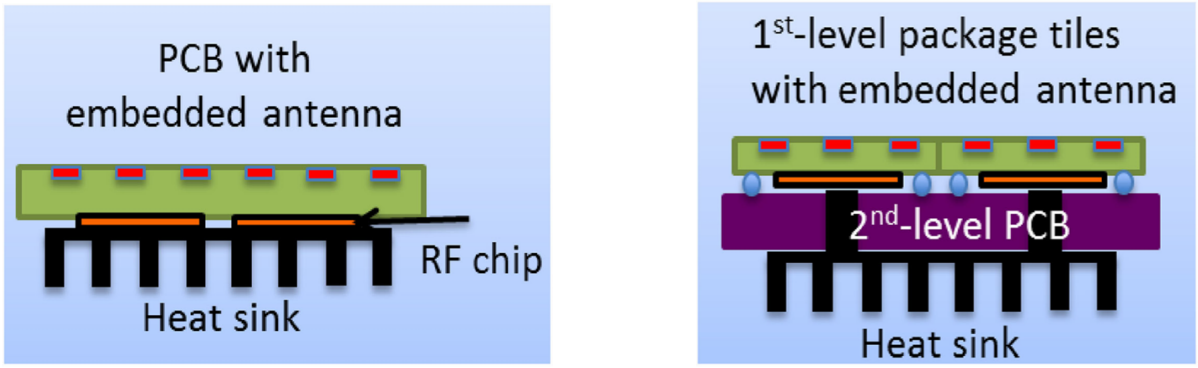
is presented in [22], where a dual linear probe fed stacked patch antenna was designed, as shown in Fig. 2.16a. The antenna exhibited an impedance bandwidth of 24% at 25 GHz. Initial simulations revealed poor isolation between the ports, peaking at −10 dB, primarily due to coupling between the probes and the direct path across the patch. To mitigate this effect, L-shaped stubs were added around the driven patch to introduce a $\lambda_g/2$ path that destructively combines with the direct coupling at port 2, as depicted in Fig. 2.16b. This modification improved the isolation by approximately 5 dB, reducing the port-to-port coupling from −10 dB to −15 dB across the operating band, which in turn reduced the boresight AR from 6 dB to below 2 dB. The authors then applied methods two and three using mirrored dual-fed antennas in a 2×2 subarray to create an 8×8 array. The boresight AR was significantly improved to 1 dB at 23 GHz, yet the worst-case 3 dB AR range at 26.5 GHz remained comparable at $\theta = \pm 35°$.

2.2.2 Active Phased Array Antenna Stack-up

In active PAAs, the antenna serves as the primary interface for transmitting or receiving signals, which are connected to active devices that can adjust the gain and phase of the signal. At higher frequencies, the physical constraints associated with element spacing make it impractical to connect active components using traditional cables and connectors. To mitigate losses introduced by these transitions, modern array designs typically integrate the antennas and the associated BFICs into a single, compact solution. This integration necessitates careful consideration of not only the antenna and RF routing, but also the power distribution, digital control signals, and thermal management within the array. Consequently, limitations on substrate thickness and material properties impose constraints on the overall stack-up design.

The literature reports two main approaches for array stack-up: a single-board solution, illustrated in Fig. 2.17a, and a tiled multi-board approach, illustrated in Fig. 2.17b. In the single-board approach, [21, 22] employed a 12-layer multi-laminate PCB to realize an 8×8 active phased antenna array. The first three layers were allocated to the antenna, consuming 1.27 mm of the total 2.54 mm available. The remaining layers facilitated routing of power and digital control signals, while the bottom layer accommodated the BFICs and other surface-mounted components. Embedded resistors were used in the Wilkinson power divider network, eliminating the need for surface-mounted resistors. Similarly, [23] implemented a 16×16 active phased array on a single 12-layer PCB using HDI technology to achieve electrical connections to every layer. Layer allocation was as such: the first seven layers (0.85 mm) supported the antenna, layers 8-10 carried digital control and power signals, layer 11 served as a ground plane, and layer 12 accommodated BFICs, RF routing,

WPDs, buffers, and connectors. The overall PCB height was approximately 1.54 mm, with a symmetric stack-up design to minimize warpage, of which 0.84 mm were allocated for the antenna.

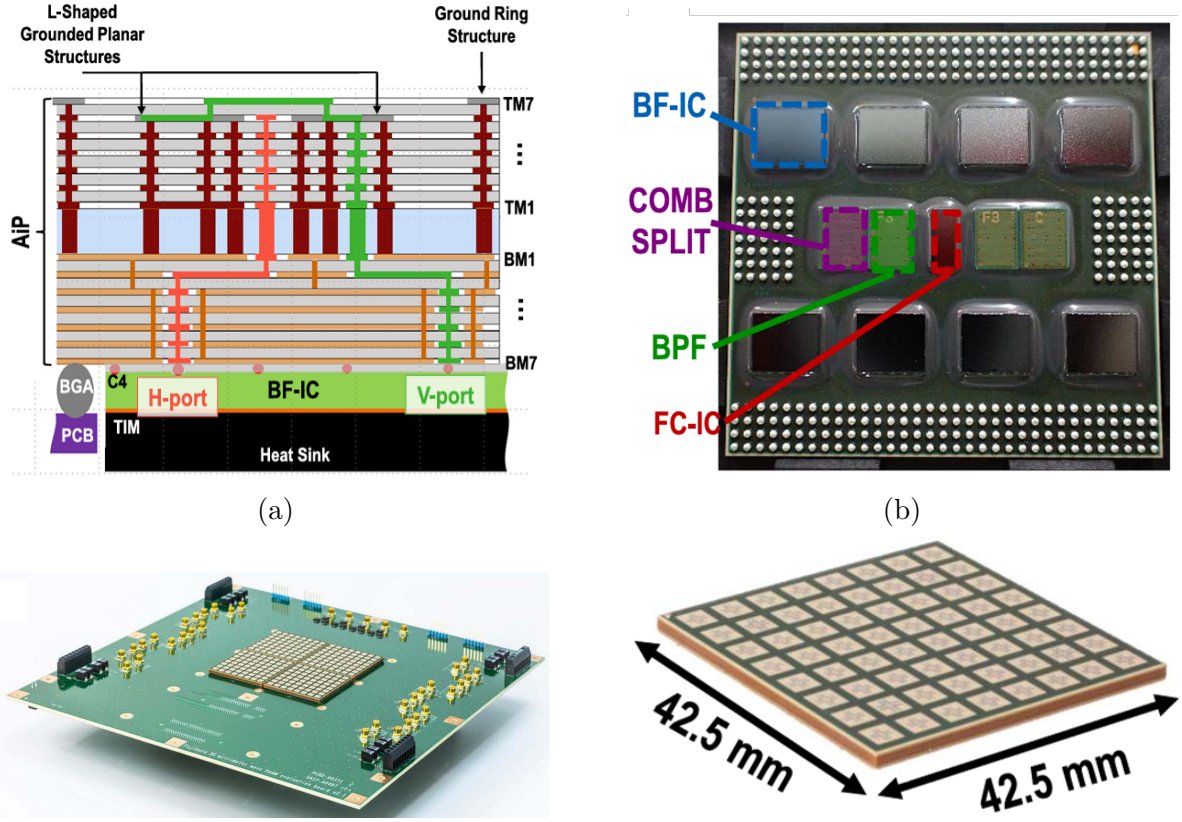


(a) (b)

Figure 2.17: General block diagram of an active PAA fabricated using a (a) single PCB and when using (b) antennas in tiled packages onto a PCB [24].

The multi-board or tiled approach offers an alternative to single-board integration. For example, [25] developed an AIP tile using a 14-layer surface laminar circuit package, containing an 8×8 antenna subarray as shown in Fig. 2.18d. In this design, each package provides five RF pins: local oscillator, TX intermediate frequency vertical polarization, TX intermediate frequency horizontal polarization, RX intermediate frequency vertical polarization, and RX intermediate frequency horizontal polarization. Each package incorporates an up/downconverter fed through a bandpass filter, followed by a 1-to-4 T-junction power divider to distribute signals to the BFICs, as shown in Fig. 2.18b. The top nine layers of the AIP were dedicated to the antenna, leaving five layers for RF, IF, LO, power, and digital signal routing. Four AIP tiles were then combined to form a larger 16×16 array mounted on a carrier PCB (Fig. 2.18c), which serves to distribute intermediate frequency signal, local oscillator, power, and digital control signals to each tile. The array achieved a measured EIRP of 68.5 dBm at P_{SAT} for 28 GHz. Scan performance at the same frequency showed an EIRP of 49 dBm at boresight, dropping to 43 dBm at $\theta = 70°$.

A limitation of the tiled approach arises from the gaps between tiles caused by the manufacturing process. These gaps introduce a secondary periodicity at the tile level, causing misalignment between the nulls generated by subarrays and the antennas, which increases sidelobe levels. In the 16×16 array, the 2.55 mm gap between tiles corresponds to 0.25λ at 29.5 GHz, resulting in an increased sidelobe level of 10.9 dB compared to the ideal

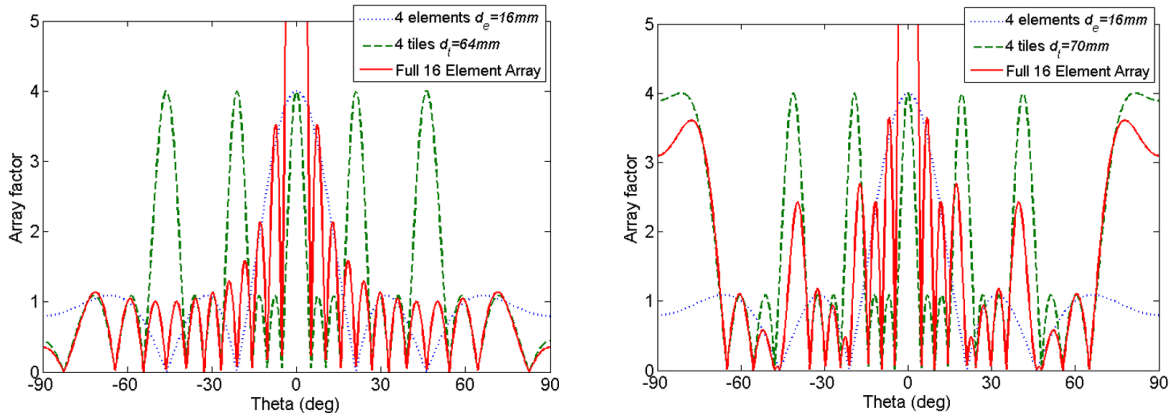


(a) (b)

(c) (d)

Figure 2.18: (a) Stack-up of a 6+2+6 AIP. (b) Bottom side of the AIP showing the BFICs, power splitter, bandpass filter, and up/downconverter [25].

-13.3 dB. To mitigate this effect, antenna excitations were tapered, successfully reducing the sidelobe level to -21.1 dB, albeit at the expense of a 6.5 dB reduction in gain.



(a) (b)

Figure 2.19: The array factor of a linear 16 element array made up of four 1×4 subarrays at 13 GHz when (a) there are no gaps in between the tiles and when (b) there is a 3 mm gap between the tiles. The blue curve shows the 1×4 subarray array factor; the green curve shows the array factor of the four tiles; and the red shows the combination of the green and blue curves [26].

2.2.3 Large Scale Phased Array Antennas for Satellite Communication

The work presented in [23] was extended in [27] to realize a 32×32 transmitter phased array antenna operating in the Ka-band to increase the EIRP. The system architecture of the 1024-element array is depicted in Fig. 2.20. In this design, the RF input signal is first distributed through two stages of WPDs, followed by amplification through drivers. Within each quadrant, the RF signal is further divided into 64 outputs using WPD network to feed the BFICs. Each BFIC features a single input and eight independent outputs, with each channel comprising its own amplifier and phase shifter. Every two output feeds into an antenna for a total of four antennas per BFIC, to generate dual linearly polarization. The antennas utilized are dual linearly polarized stacked patch antennas, occupying the first seven layers of the 12-layer HDI PCB. The unit cell was designed under periodic boundary conditions with a cell size of 4.67 mm ($0.48\lambda_h$), effectively suppressing scan blindness and grating lobes across the frequency band. The antennas achieved a return loss better than

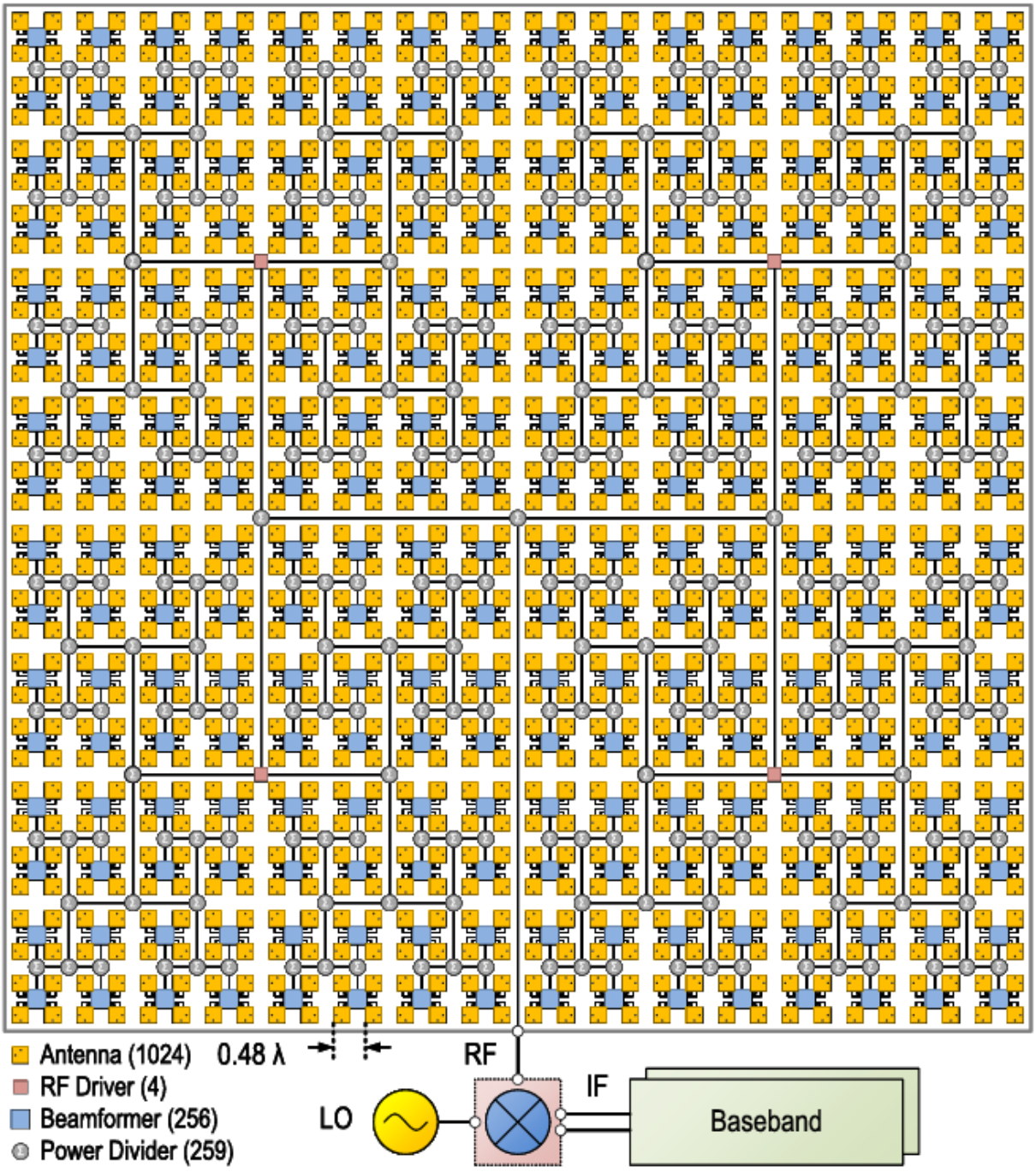


Figure 2.20: Block diagram of the 1024 element transmitter active phased array in [27].

-15 dB and feed coupling below -18 dB over the operating band. The BFICs were off-the-shelf components from Renesas, and the 2×2 subarray block diagram is shown in Fig. 2.21. WPDs were designed as 1-to-2 power dividers (Fig. 2.22) with a circuit model detailed in Fig. 2.22a, comprising of a 42 Ω impedance transformer split into two 62 Ω lines and connected via a 100 Ω surface-mounted resistor. Simulations indicate a return loss of -18 dB at the input port, -23 dB at the output ports, and output port isolation better than -20 dB across the band. The 1024-element transmitter array achieved a peak EIRP of 78 dBm at the 1 dB compression point, with a measured scan loss of 3.3 dB at $\theta = 60°$, cross polarization below -26 dB, and a boresight AR of 3 dB maintained across the 27.5—31 GHz band and ±70° scan range at 29 GHz.

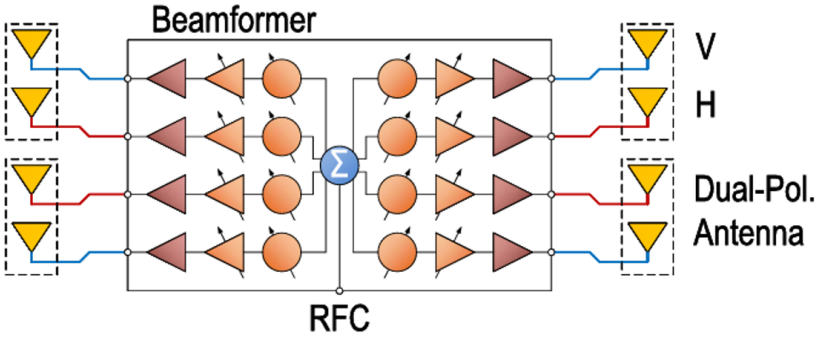
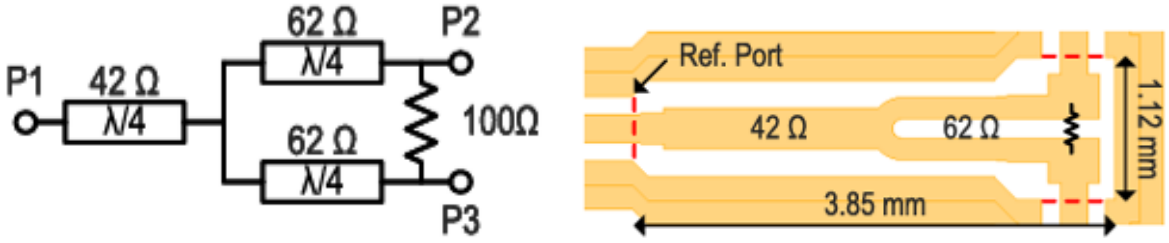


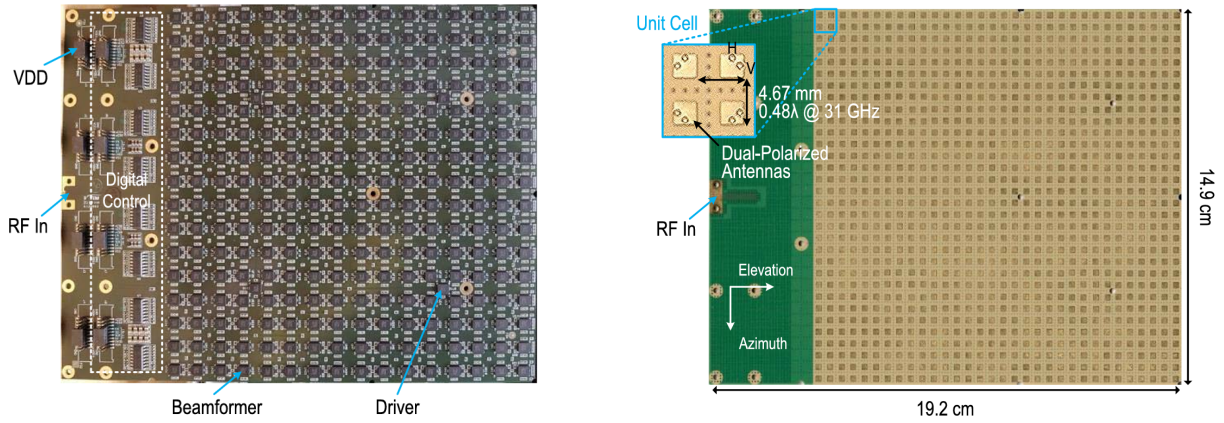
Figure 2.21: 2×2 subarray used in [27] to build the 1024 element array.



(a) (b)

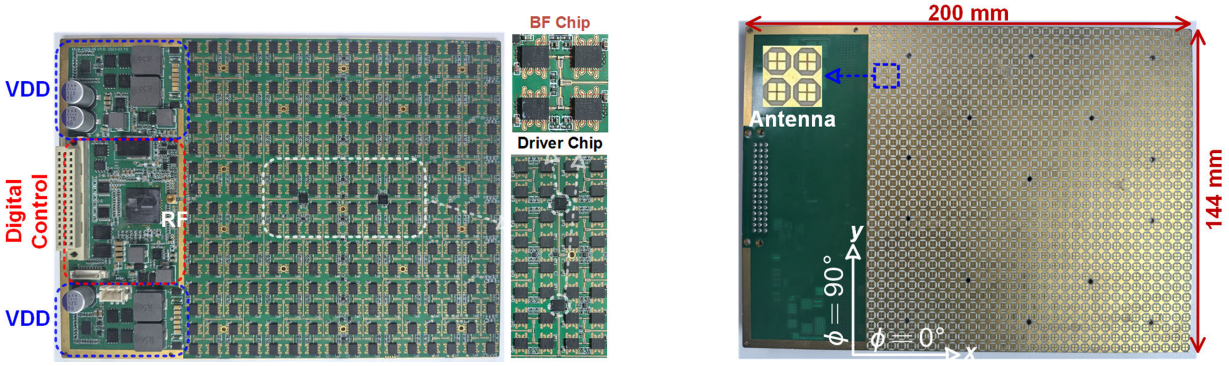
Figure 2.22: The WPD used in [27, 28] where (a) shows the circuit model and (b) shows the layout.

Another example of a large active array is reported in [29], featuring a similar architecture to Fig. 2.20, with the primary difference being that drivers were implemented per half-array rather than per quadrant. RF signals were distributed to the BFICs, from Renesas, via a network of 1-to-2 WPDs. Each divider utilized a 50 Ω line split into two 70.7 Ω



(a) (b)

Figure 2.23: The 1024 element transmitter array in [27]. (a) Bottom side of the PCB. (b) Top side of the PCB.



(a) (b)

Figure 2.24: 1024 element transmitter array in [29]. (a) Bottom side of the PCB. (b) Top side of the PCB.

impedance transformers connected with a 100 Ω 0402 resistor. Simulations of the 1-to-2 divider demonstrated return loss below -22 dB across all ports and isolation better than -25 dB. When cascading a quarter of the WPD network to represent the full array, return loss degraded slightly to -20 dB at input ports and -12 dB at outputs, with amplitude variation within ±0.5 dB.

This array introduced a novel stacked metasurface antenna, dual circularly polarized, with one port exciting left-hand and the other right-hand circular polarization. The antenna unit cell was designed under periodic boundary conditions with a size of 4.5 mm ($0.47\lambda_h$), achieving matching across 27.5—31 GHz and isolation better than -15 dB. A 2×2 subarray achieved simulated AR below 1 dB using sequential rotation. The array employed a 13-layer multi-laminate PCB, with the first six layers allocated to the antenna (1.9 mm of 2.7 mm total). Measured performance included a peak EIRP of 72 dBm at the 1 dB compression point, amplitude variation of 6 dB across frequency, scan loss of -4 dB at 60°, cross polarization exceeding 20 dB, and AR maintained below 3 dB across the band and scanning range.

Chapter 3

Design Methodology of Large Phased Array Antenna and Feed Network

The design of large-scale PAA requires a systematic approach to ensure accurate beamforming and polarization control across the array. The methodology involves iterative tuning of antenna elements modeled under periodic boundary conditions to achieve well matched active S-parameters and evaluation of radiation performance across different scan angles. Concurrently, the feed network is designed to provide uniform and matched power distribution to all antenna elements, while maintaining isolation between ports and supporting scalable architectures.

3.1 Design Requirements

3.1.1 Antenna Design Requirements

The proposed antenna design must satisfy several critical performance criteria to ensure reliable operation within SATCOM systems and compatibility with array implementations:

- The antenna shall exhibit an impedance bandwidth of at least -10 dB across the 27.5–31 GHz frequency range.
- Circular polarization must be maintained, with an AR not exceeding 3 dB, to meet SATCOM requirements.

- For LEO satellite operation, the antenna array shall support beam scanning up to $\pm 70°$.
- The design must be scalable to arrays comprising 1024 elements or more.
- The antenna shall be realizable using commercially available PCB fabrication technology.
- Sufficient PCB layers must be allocated to accommodate power distribution and digital signal routing without compromising RF performance.

3.1.2 Feed Network Design Requirements

The feed network, which distributes signals to each BFIC, must satisfy the following requirements:

- The input impedance of the network must remain below -10 dB across the 27.5–31 GHz operating band.
- The input signal must be divided equally among all output ports to ensure each BFIC receives the same power.
- Individual power dividers must be compact enough to be placed between BFICs without interfering with their layout or placement.

3.2 PCB Stack-Up Definition

All of the designs presented in this thesis were implemented on a 12-layer PCB fabricated using a low loss dielectric material in combination with HDI technology. The substrate, with a dielectric constant of $D_k = 3$ and a low loss tangent of $D_f = 0.0025$, was selected due to its favorable electrical performance at high frequencies as well as its compatibility with HDI manufacturing processes. These properties make it particularly suitable for multilayer RF designs where both low insertion loss and manufacturability are critical.

The proposed stack-up configuration, shown in Fig. 3.1, follows a "5+2+5" arrangement aiming to provide enough height for the antenna while allocating layers for power and digital. The board is constructed from a 2-layer core (layers L6 and L7), which is mechanically drilled to form vias between these central layers. Additional layers are sequentially

laminated above and below the core, beginning with L5 and L8, and repeated until the full 12-layer stack-up is achieved. Between each lamination step, laser-drilled micro-vias are employed to connect adjacent layers. Upon completion of the stack-up, through-holes can be mechanically drilled to connect the outermost layers (L1 to L12).

The use of micro-vias is particularly advantageous in dense layouts, as they provide direct access to any layer without the stubs that typically arise in conventional via structures. After drilling, the vias are plated with copper to ensure electrical continuity, and subsequently filled with resin or copper depending on design requirements. However, reliability concerns must also be considered. The different thermal expansion coefficients along the z-axis can can introduce mechanical stresses that manifest as cracking or misalignment in stacked micro-vias, as illustrated in Fig. 3.2. For this reason, stacking multiple micro-vias is generally discouraged and is typically limited based on the manufacturer capabilities. Additional manufacturing constraints were imposed by the PCB vendor to ensure yield and reliability. Specifically, micro-vias were required to have a minimum radius of 3 mil with a corresponding pad diameter of 6 mil.

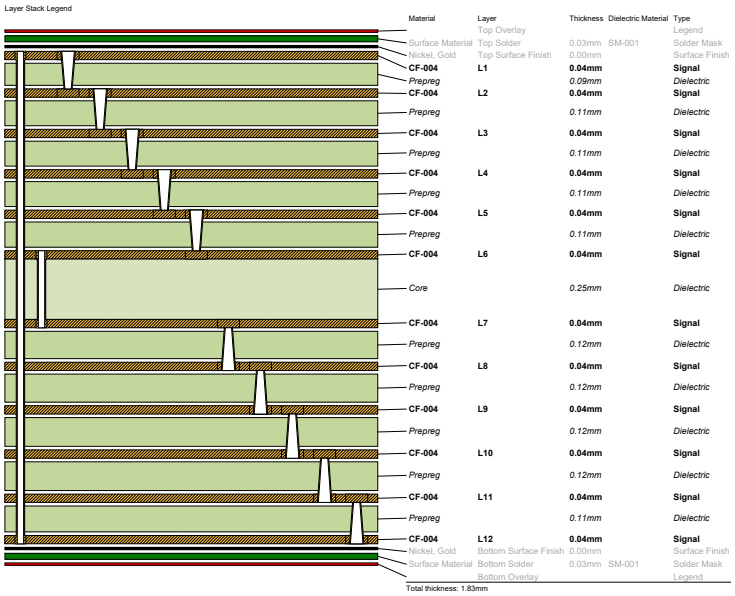
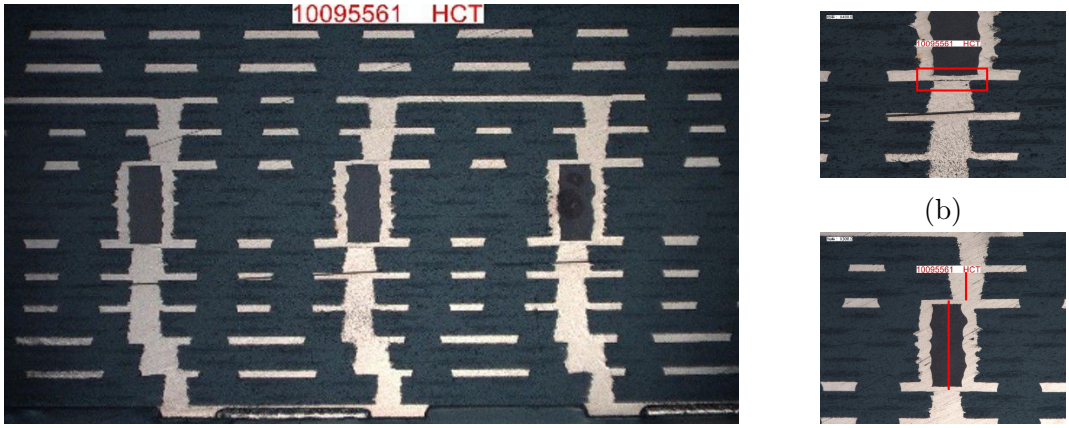


Figure 3.1: 12-layer PCB stack-up using HDI process with micro-via to access every layer.



(a)

(b)

(c)

Figure 3.2: (a) Fabricated cross-section of the proposed 12-layer stack-up. (b) Cracking between via and pad. (c) Misalignment of micro-vias.

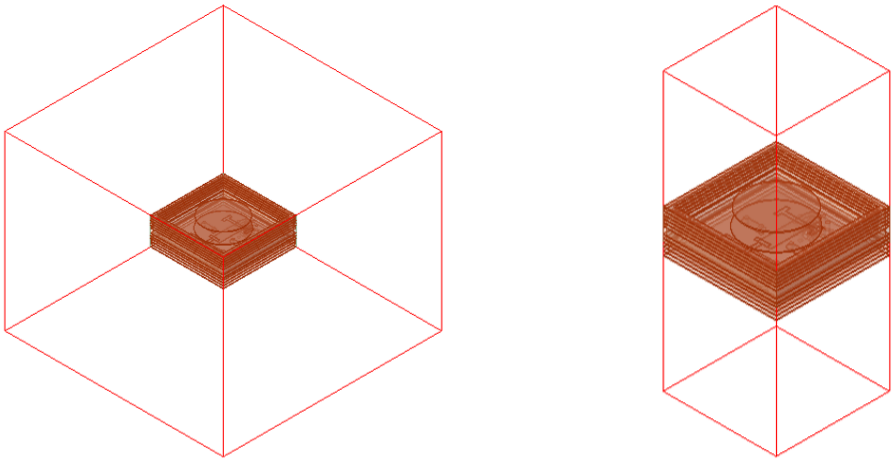
3.3 Antenna Design

3.3.1 Antenna Analysis in a Large Array

Ansys HFSS is a 3-D full-wave EM solver, it enables the modeling of complex geometries such as antennas, microwave circuits, and RF devices. To simulate structures in HFSS, boundary conditions need to be defined. In conventional antenna designs, the boundaries are defined as radiation surfaces positioned at least $\lambda/4$ away from the structure in all directions, as illustrated in Fig. 3.3a. This boundary absorbs outgoing waves and computes far-field radiation characteristics, ensuring that the simulated performance closely reflects that of the fabricated device. This simulation model is referred to as explicit simulation or open boundary condition.

For single antennas or small-scale arrays, explicit simulation is computationally viable and can typically be executed on local desktop workstations. However, as the size and complexity of antenna arrays increase, the computational burden grows exponentially. Larger arrays demand significantly greater memory and processing power, often rendering explicit simulations infeasible on standard computing resources. This limitation underscores the need for alternative simulation strategies or high-performance computing environments when analyzing large-scale antenna systems.

To overcome the computational challenges associated with explicit simulations of large



(a) (b)

Figure 3.3: (a) Explicit simulation boundary condition shown in red where there are radiation boundaries on all 6 faces. (b) Unit cell under periodic boundary condition, where the radiation boundaries are on the top and bottom, while the pair of parallel faces are set to be equivalent.

arrays, periodic boundary condition was introduced. This approach is effective for structures composed of a repeated unit cell, as is the case in antenna arrays. Under periodic boundary condition, the simulator assumes that the unit cell extends infinitely in all directions. Consequently, only a single antenna element requires meshing, drastically reducing computational cost. An example of such a unit cell bounded by periodic conditions is shown in Fig. 3.3b. To realize periodic boundary condition, the simulator equates the fields on two parallel boundaries. In phased arrays, beam steering can be modeled within this framework by applying a phase shift between the periodic boundaries, corresponding to the desired scan angle. These features makes periodic boundary conditions suitable for studying array performance across scan ranges. However, the periodic approach introduces certain limitations that must be carefully considered, with respect to S-parameter interpretation.

By definition, S-parameters are passive and represent the response of a device under independent port excitations. By contrast, under periodic boundary condition, the reported S-parameters are "half-active", since all unit cells are assumed to experience the same excitation as the reference element. For instance, if port 1 of the unit cell is excited, the reported $S_{1,1}$ reflects the condition where all other unit cells are likewise excited at their port 1. The periodic return loss, given by equation 3.1, explicitly depends on the collective

excitation of the array. This differs from the active return loss, in equation 2.8, where all ports are excited. The distinction between passive S-parameters and periodic S-parameters is important as it affects calibration and tapering performance, where uniform excitation is not the case. Fig. 3.4 shows the $S_{1,1}$ of an antenna under periodic boundary condition compared to when the same antenna is in a 16×16 array. It is evident that the $S_{1,1}$ is drastically different. When looking to the active $S_{1,1}$ when all other port 1s are turned on, it is clear that the periodic boundary condition reported S-parameters are "half-active".

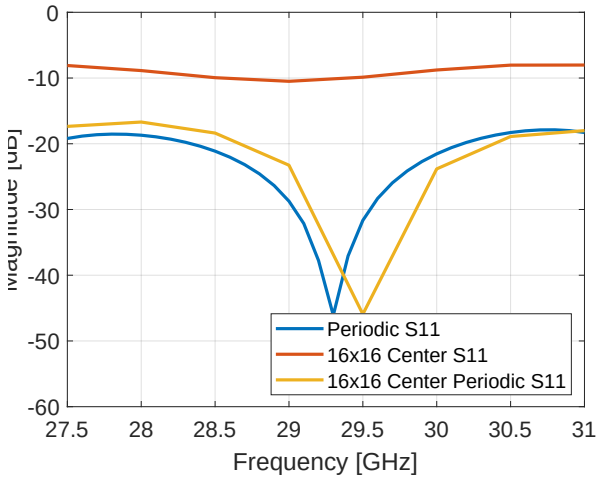


Figure 3.4: $S_{1,1}$ of an antenna simulated under periodic boundary condition compared to when simulated in a 16×16 array and the "half-active" $S_{1,1}$.

Furthermore, the dependence on mutual coupling implies that the periodic return loss cannot be directly measured, as it would require measurement of a large count of mutual couplings. Not only is the number of measurements large, the test structure is also difficult to design at higher frequencies where connectors cannot fit within the unit cell. [30] mentions that to measure the active return loss of an antenna in a 48 element array, 9.4 hours would be needed to measure 1128 points, assuming each measurement takes 30 seconds. For a 224 element array, 208 hours would be needed to measure 24976 points.

$$S_{i,i}^{per} = \frac{\sum_{n=i}^{N} S_{i,n} a_n}{a_i}, n = \begin{cases} \text{even}, & \text{if } i \text{ is even} \\ \text{odd}, & \text{if } i \text{ is odd} \end{cases} \tag{3.1}$$

where

i : reference port
a_n : excitation of n^{th} port

More importantly, in [31], Pozar discusses the concept of the active element pattern, which accounts for the distortion of an individual element's radiation pattern due to mutual coupling within an array environment. Unlike an isolated antenna, the radiation of a reference element is altered because "adjacent elements will radiate some power due to mutual coupling with the fed element." As a result, the radiation observed from the fed element inherently differs from its isolated counterpart. Under periodic boundary conditions, HFSS can only report this active element pattern, rather than the isolated element pattern. Pozar then derives two equations. the first, given in equation 3.2, defines the active element gain as a function of the reflection coefficient $\Gamma(\theta_0, \phi_0)$. This coefficient encapsulates both the effects of mutual coupling and the excitation phase distribution, thereby making the active element gain dependent on the scan angle. Interestingly, this equation is simply the realized gain. The second equation relates the active element pattern to the overall array pattern by multiplying the contribution of the active element by the number of elements in the array. It is important to note, however, that these relationships are valid only when the observation angle coincides with the scan angle, i.e., $\theta = \theta_0$.

$$G^e(\theta_0, \phi_0) = \frac{4\pi d^2}{\lambda^2}[1 - |\Gamma(\theta_0, \phi_0)|^2] \cos\theta_0 \tag{3.2}$$

$$G^a(\theta_0, \phi_0) = NG^e(\theta_0, \phi_0) \tag{3.3}$$

where

G^e	: active element gain
θ_0, ϕ_0	: direction of scanning
d	: dimensions of the unit cell
Γ	: active reflection coefficient
G^a	: array gain
N	: number of elements in the array

To validate the equations proposed in [31], an explicit simulation was performed on a 16×16 array to compare with periodic boundary condition simulations. The computational cost of this analysis was substantial: solving eleven frequency points required approximately one week of runtime on a server equipped with 90 cores and 768 GB of RAM. In contrast, the same antenna simulated using periodic boundary condition was completed in under five minutes on a local workstation with ten cores and 32 GB of RAM, while also resolving 81 frequency points.

The comparison of the simulated results is shown in Fig. 3.5. The element pattern, reported by HFSS under periodic boundary conditions is plotted in blue. When a phase shift is applied between the boundaries to emulate beam steering, the active element pattern

correspondingly shifts. The interpolated active element pattern, derived by evaluating the gain at $\theta = \theta_0$ in increments of 10° is shown in orange. In black shows the 16×16 array pattern as it is steered from $-70°$ to 70° in increments of 10°. These array patterns are generated by a full EM simulation of the 16×16 PAA. The results confirm that the active element pattern closely tracks the scanned array pattern rather than the element pattern.

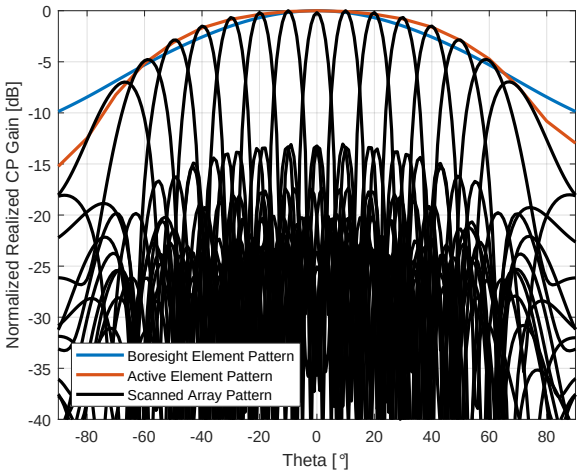


Figure 3.5: Normalized circularly polarized realized gain pattern of the element pattern, active element pattern, and scanned 16×16 array.

3.3.2 Design Methodology of Large Phased Array Antennas

Given that periodic boundary conditions do not capture the passive behavior of an antenna, the proposed design methodology begins with the antenna considered as an isolated element. In this initial stage, the antenna is analyzed under open boundary conditions, where no adjacent antennas are present and an extended ground plane may be included if necessary. At this point, certain geometric limitations are also applied to account for the antenna in an array. The antenna itself must remain within $0.5\lambda_h$ while the ground size should be expanded to 1.5λ with the antenna centered. The primary objective at this stage is to generate a first-order approximation of the antenna's radiation characteristics. Emphasis is placed on the gain pattern rather than the realized gain, thereby alleviating the need to tune the antenna for impedance mismatch. The simulated gain pattern is compared against theoretical models and literature references to verify that the antenna radiates as intended. It is expected that the directivity is higher than in the periodic

boundary condition since the power can be re-radiated from adjacent antennas in an array environment.

Once the isolated antenna demonstrates the desired radiation characteristics, it is subsequently modeled under periodic boundary conditions. The design is first tuned to match the active S-parameters at boresight. Depending on the operation of the antenna, whether the application demands simultaneous dual port excitation or single port excitation, the designer should refer to the active S-parameters or the periodic S-parameters, respectively. The antenna is then swept across a range of scan angles to evaluate both the active impedance matching and the active element gain. This procedure enables the identification of potential scan blindness or other anomalies that may occur when steering away from boresight. After validating the antenna performance under these conditions, the design of the feed network is undertaken. A flow chart of this process can be seen in Fig. 3.6.

3.3.3 Patch Antenna Design

The design of the antenna is enclosed in an area of 4.8 mm $\times$ 4.8 mm, corresponding to $0.496\lambda_h$ at the highest operating frequency of 31 GHz. This dimension was selected to suppress grating lobes within $\pm 90°$. As outlined in the literature review, the slot-fed patch architecture was adopted due to its inherently high port-to-port isolation, which enables low cross-polarization and low axial ratio, albeit at the cost of increased structural complexity.

The antenna stack-up comprises two radiating patches: the first on layer 1 with a radius of 52 mils, and the second on layer 6 with a radius of 54 mils. The ground plane is located on layer 7, where two orthogonal H-shaped slots are etched—one for each polarization. Each slot is excited by a low-impedance open-ended stub, which is in turn driven by a coaxial-like probe. The probe transitions to a CPWG transmission line on layer 12.

While stripline routing would ideally be used due to its complete field confinement and broadband behavior, it requires an additional ground layer. CPWG, on the other hand, offers sufficient field confinement and reduced radiation compared to microstrip, which suffers from stronger fringing fields. To minimize undesired coupling between the feeding stubs, four vias were added between layers 7 and 9, positioned between the two slots. Furthermore, a surrounding cavity was implemented to suppress surface waves and enhance mechanical rigidity. The remaining layers (10–12) are allocated for power routing and BFIC integration. The complete antenna structure is shown in Fig. 3.7. Overall, the antenna occupies 1.34 mm of the available 1.82 mm total stack height.

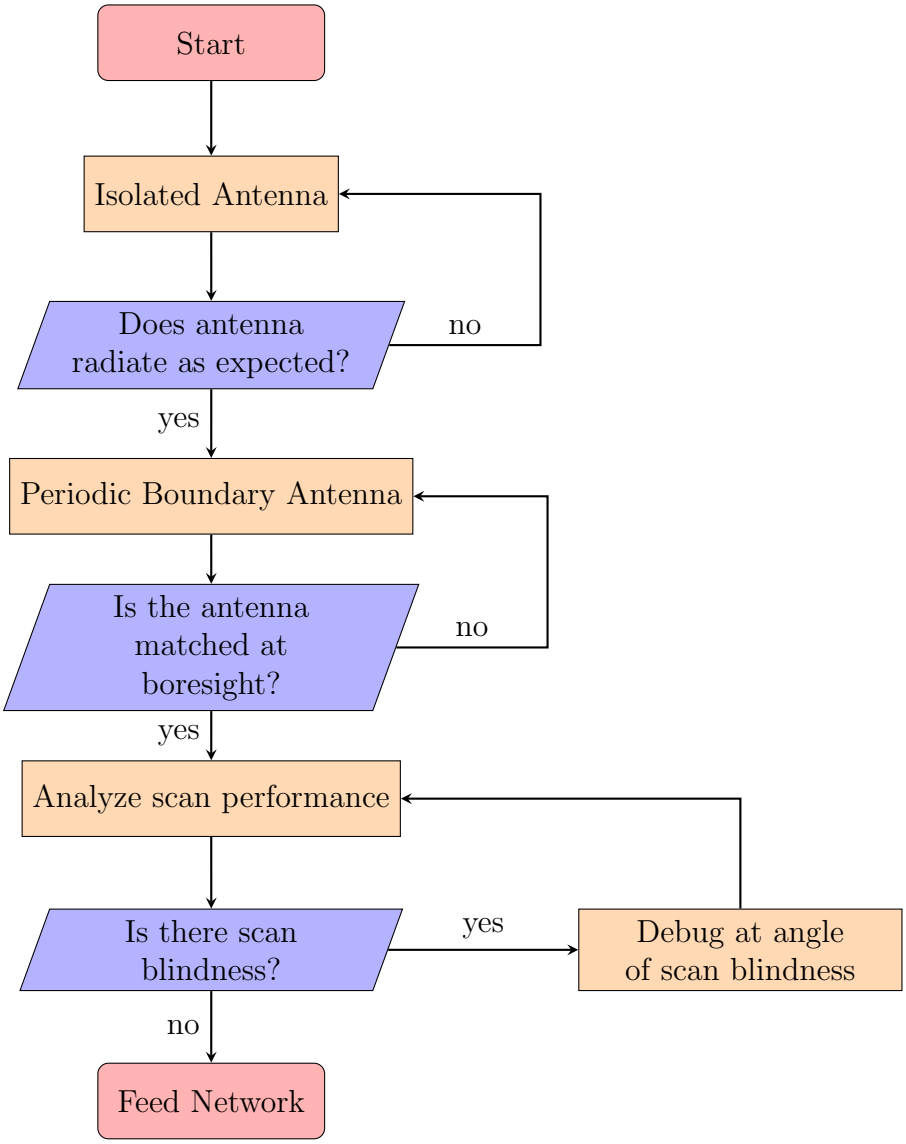
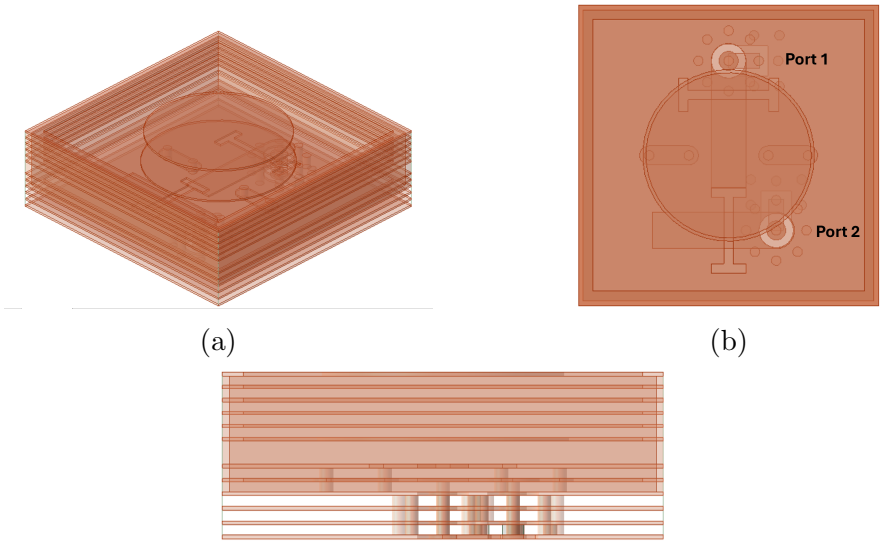


Figure 3.6: Design methodology of an antenna in a large array.



(a) (b)

(c)

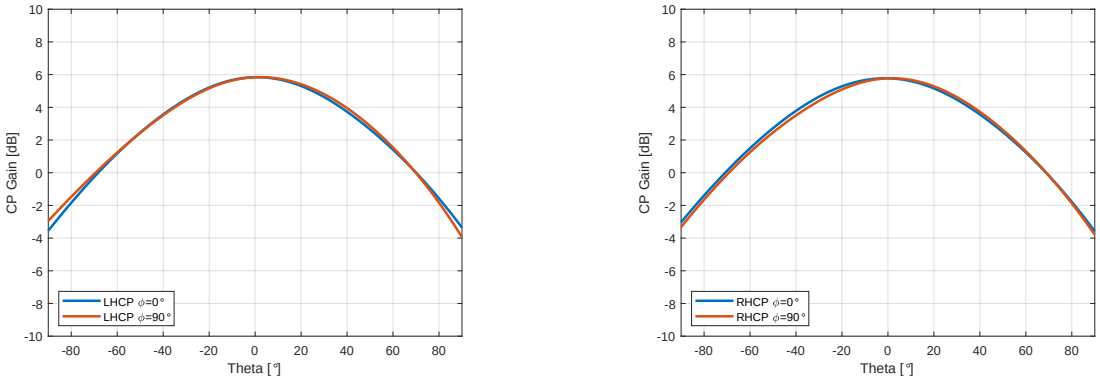
Figure 3.7: HFSS model of the proposed patch antenna. (a) Isometric view. (b) Top view. (c) Side view.

Isolated Antenna

Following the proposed design methodology, the antenna was initially analyzed under open boundary conditions to obtain a first-order approximation of its radiation characteristics. The circularly polarized gain patterns at 29.5 GHz are presented in Fig. 3.8. Under LHCP and RHCP excitation, the antenna achieves peak gains of 5.84 dB and 5.77 dB at boresight, respectively. The radiation patterns remain smooth and free from noticeable distortions or irregularities within $\pm 90°$, consistent with the literature. These results demonstrate that the open-boundary design provides a suitable first-order starting point before transitioning to the periodic boundary condition model.

Periodic Boundary Condition: Boresight

The design was then retuned under periodic boundary condition where the S-parameters are presented in Fig. 3.9. Both ports exhibit return losses below –18 dB across the operating band, comfortably meeting the –10 dB criterion. Despite the asymmetry in the feed structure, similar matching was achieved in both ports. Port isolation remains better than



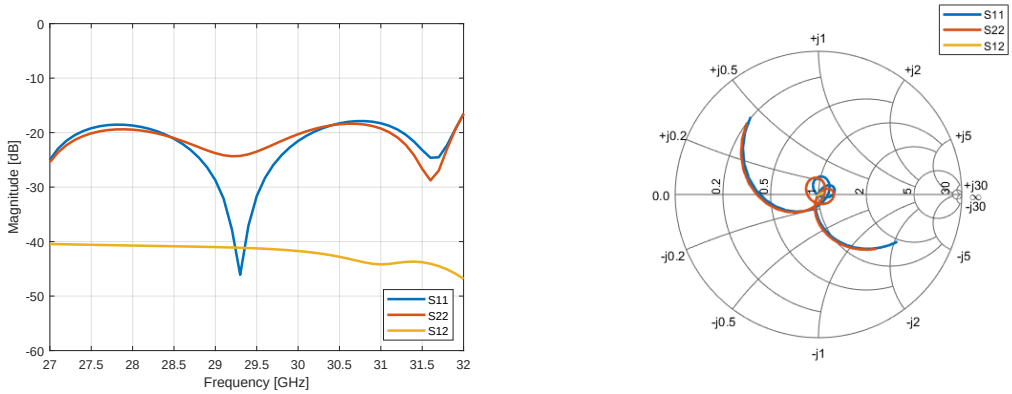
(a) (b)

Figure 3.8: Circularly polarized gain of the patch antenna under open boundary condition at 29.5 GHz under (a) LHCP and (b) RHCP excitation.

–40 dB across the band, largely due to the orthogonal slot placement and the shielding vias that suppress coupling through the stubs on layer 8.

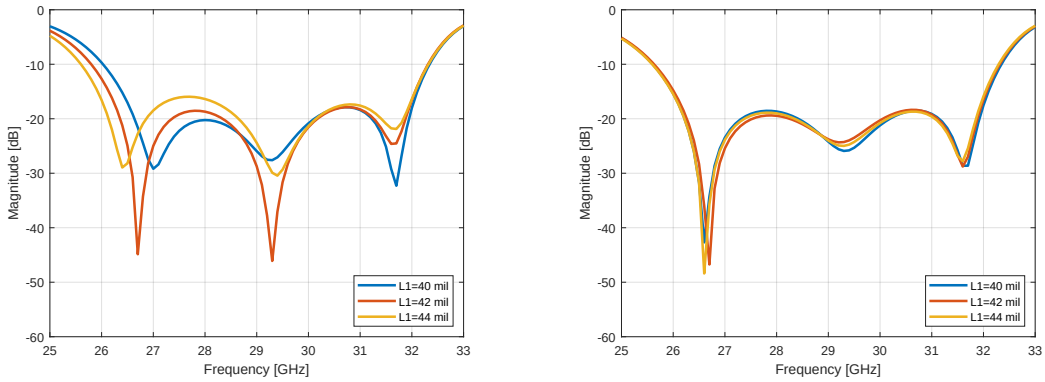
The impedance response reveals three distinct resonances, one from the first patch, the second from the second patch, and the third from the slot. As shown in Fig. 3.10a, varying the slot length shifts the resonance around 26.7 GHz while leaving the other two largely unaffected, confirming that the lowest-frequency resonance originates from the slot. Fig. 3.10b demonstrates that modifying the first slot does not impact the matching at port 2, consistent with the strong isolation observed. As such, the design of slot 1 and its feed can be independent from slot 2 and vice versa. However, since both ports still share the two patches, changing their radius will impact both ports. Fig. 3.11 and shows that changing the upper patch's radius affects the center resonance while the other two remain static, indicating that the second resonance is generated by the upper patch. This leaves the third resonance to the lower patch. Fig. 3.12 shows that varying the radius of the lower patch causes shifts on all three resonances as well as their matching at both ports. As mentioned in [17], the lower patch is strongly coupled to the slot as well as the upper patch. This causes the lower patch to play a vital role in managing the coupling both to the upper patch and to the slot.

The active S-parameters, presented in Fig. 3.14a, confirm that the antenna preserves excellent impedance matching in an active environment, with both ports maintaining return losses below –18 dB. Only minimal deviation is observed when compared to the conventional S-parameters, a consequence of the high isolation suppressing load modulation



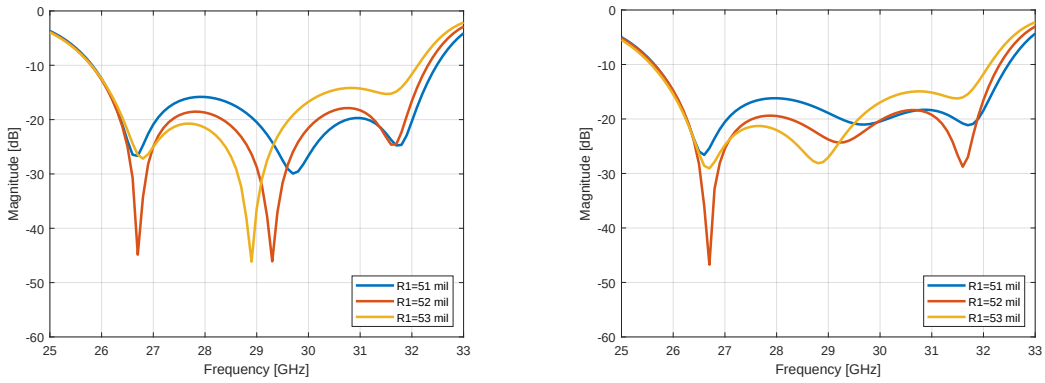
(a) (b)

Figure 3.9: Periodic S-Parameters of the designed slot fed antenna in (a) magnitude and (b) smith chart.



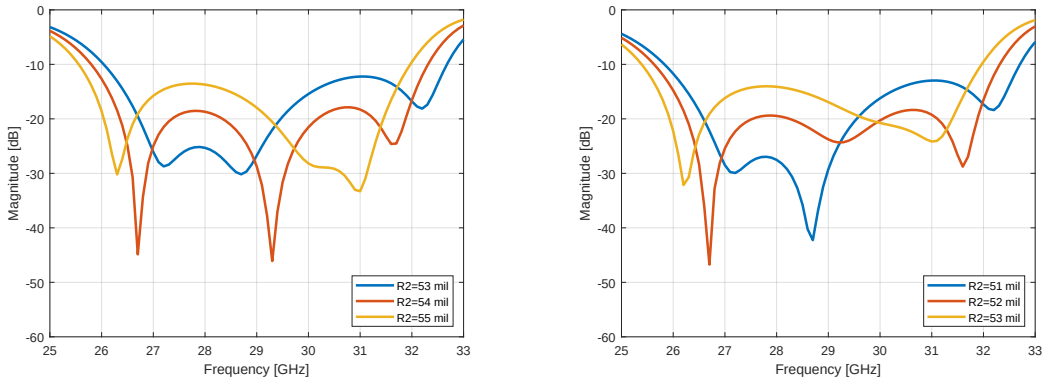
(a) (b)

Figure 3.10: (a) S_{11} and (b) S_{22} of the designed antenna as the length of slot 1 L_1 is varied.



(a) (b)

Figure 3.11: (a) S_{11} and (b) S_{22} of the designed antenna as the radius of the upper patch R_1 is varied.

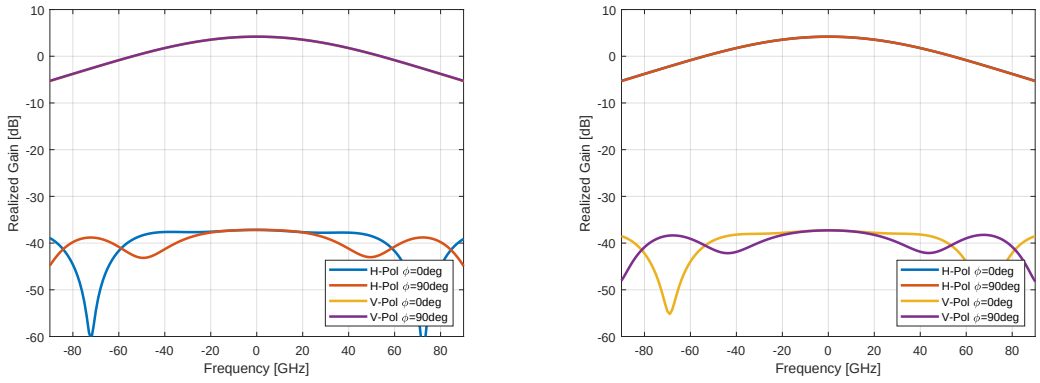


(a) (b)

Figure 3.12: (a) S_{11} and (b) S_{22} of the designed antenna as the radius of the lower patch R_2 is varied.

effects between ports. In terms of the radiation performance, the high isolation manifests in high polarization purity. The realized linear gain, shown in Fig. 3.13, demonstrates a cross-polarization discrimination of 40 dB at boresight when exciting one port at a time, highlighting the ability of the architecture to suppress undesired polarizations.

When both ports are simultaneously excited in quadrature, the antenna achieves circular polarization. The AR, shown in Fig. 3.14b, remains below 0.4 dB at boresight across the band, satisfying the AR specification. These results confirm that the antenna not only enables robust linear polarization but also facilitates highly pure and stable circular polarization, making the antenna suitable for applications requiring stringent polarization performance.

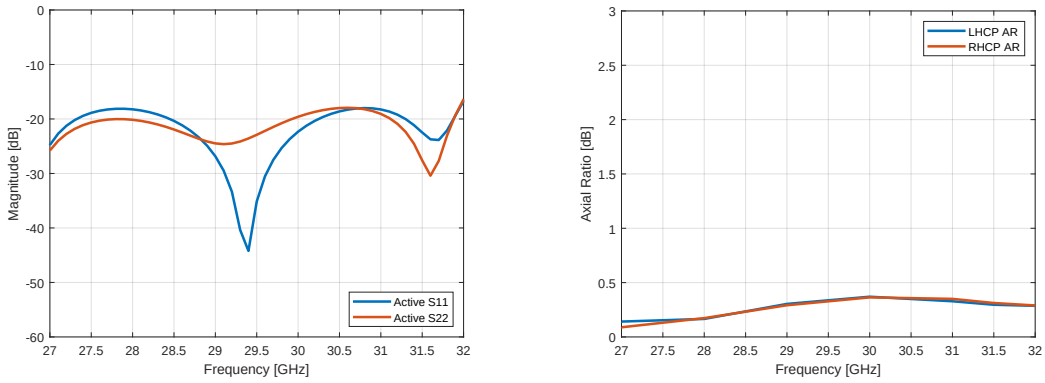


(a) (b)

Figure 3.13: Co-polarized and cross-polarized linear gain when (a) port 1 is excited and (b) when port 2 is excited.

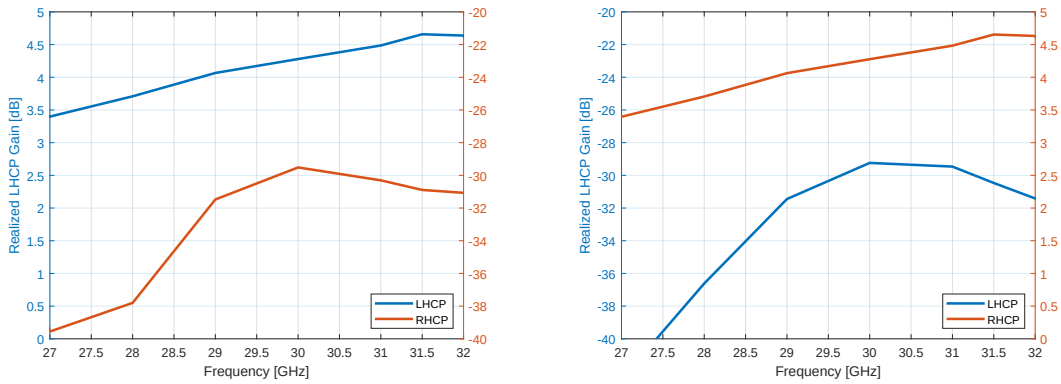
At boresight, the antenna demonstrates stable gain performance, with a maximum variation of 1 dB observed for both LHCP and RHCP across the examined frequency band, as shown in Fig. 3.15. Cross-polarization levels were shown to be at worst 33.75 dB below the co-polarized component throughout the operating band, successfully pure co-polarized fields.

The radiation efficiency was consistently maintained above 93%, indicating that the majority of the input power is effectively converted into radiated power. Meanwhile, the total efficiency remained above 91% throughout the band, accounting for additional losses introduced by mismatch. The difference between the radiation efficiency and total efficiency is directly reflected in the active S-parameters. This correlation highlights the impact of port matching and mutual coupling on the overall system efficiency, confirming that the



(a) (b)

Figure 3.14: (a) Active S-Parameters of the designed slot fed antenna. (b) Boresight AR across frequency.



(a) (b)

Figure 3.15: Boresight circular gain across frequency when in (a) LHCP mode and (b) RHCP mode.

antenna maintains both high radiation performance and effective power transfer even under active operating conditions.

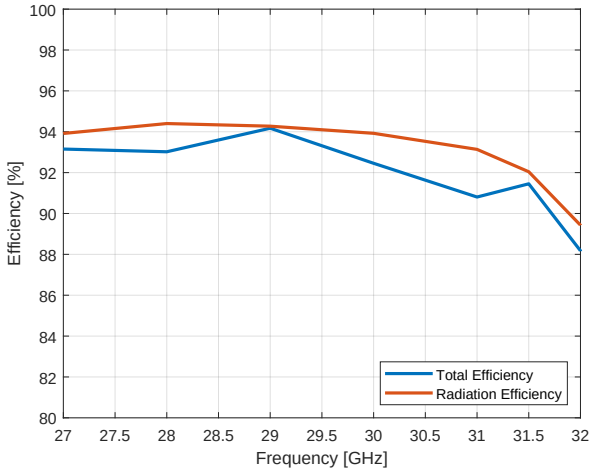
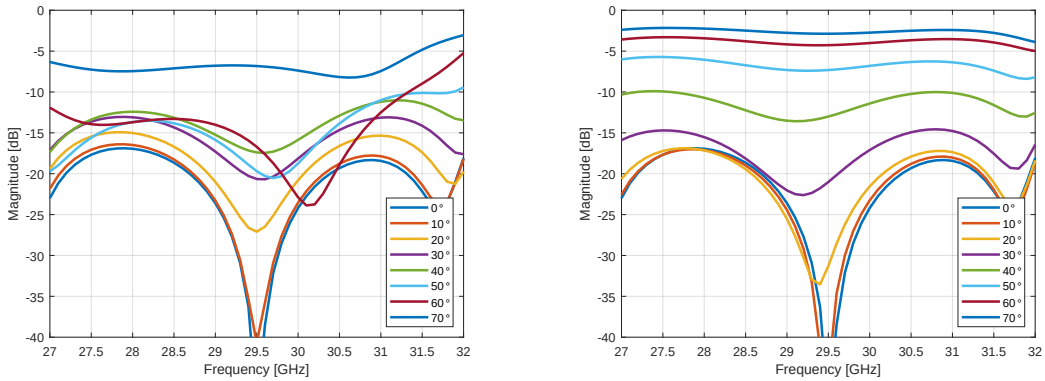


Figure 3.16: Total efficiency and radiation efficiency of the antenna across frequency.

Periodic Boundary Condition: Scanning

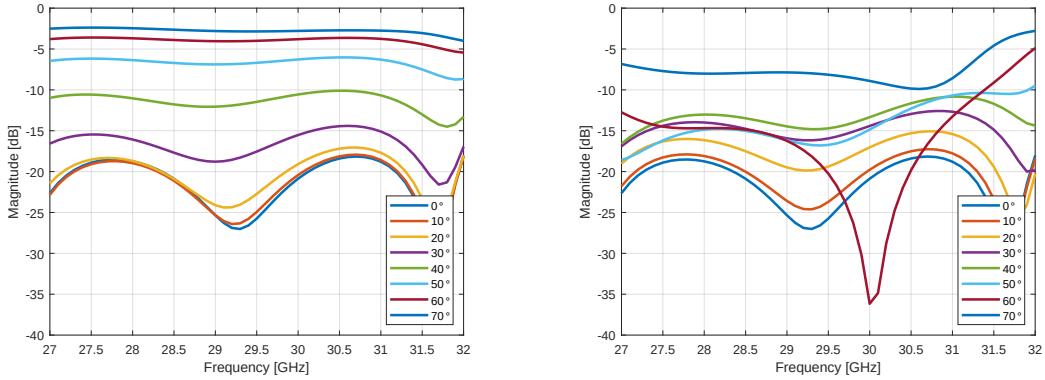
The active return loss results in Fig. 3.17 and Fig. 3.18 highlight the strong dependence of impedance matching on scan angle and feed orientation. A complementary behavior is observed between the two polarizations: along the $\phi = 0°$ plane, the active S_{11} remains well matched (< -10 dB) up to 60°, but degrades to -6 dB at 70°. Along the orthogonal $\phi = 90°$ plane, however, S_{11} degrades more rapidly, reaching only -3 dB at 70°. The same trend is observed for the active S_{22}, with poor matching arising when the scan direction aligns unfavorably with the feed orientation. This indicates that load modulation is highly scan-dependent.

The circularly polarized realized gain patterns in Fig. 3.19 provide further insight into this behavior. Both LHCP and RHCP patterns remain symmetric and largely undistorted, confirming that the antenna maintains its polarization purity across frequency and scan angles. At 27.5 GHz, the scan loss follows a $\cos^{1.1}(\theta)$ trend, with only 4.9 dB reduction at 70°. At 31 GHz, the trend steepens to $\cos^{1.6}(\theta)$, leading to 7.5 dB loss at 70°. This difference can be attributed to the higher directivity at the upper frequency, which narrows the beam and increases sensitivity to steering. Table. 3.1 shows the scan losses at 0°, 60°, and 70° across 27.5, 29.5 and 31 GHz. It is clear that the worst case scan loss occurs at 31



(a) (b)

Figure 3.17: Active S_{11} as the antenna is scanned along (a) $\phi = 0°$ and (b) $\phi = 90°$.



(a) (b)

Figure 3.18: Active S_{22} as the antenna is scanned along (a) $\phi = 0°$ and (b) $\phi = 90°$.

GHz. However, when looking to the actual gain in Table. 3.2, the gain at the wider angles are not largely varying across frequency, it is more so that the boresight gain is increasing with frequency that causes scan loss to increase. In addition, when considering the gain pattern at 31 GHz (not shown here), the observed scan loss is -5.5 dB at 70°, about 2 dB lower than the realized gain loss, showcasing the compounding effects on scan loss.

θ	27.5 GHz	29.5 GHz	31 GHz
0°	0 dB	0 dB	0 dB
60°	-4.12 dB	-4.08 dB	-4.74 dB
70°	-6.16 dB	-6.21 db	-7.42 dB

Table 3.1: Scan loss across frequency and scan angles.

θ	27.5 GHz	29.5 GHz	31 GHz
0°	3.54 dB	4.19 dB	4.49 dB
60°	-0.58 dB	0.11 dB	-0.25 dB
70°	-2.62 dB	-2.02 db	-2.93 dB

Table 3.2: Circularly polarized realized gain across frequency and scan angles.

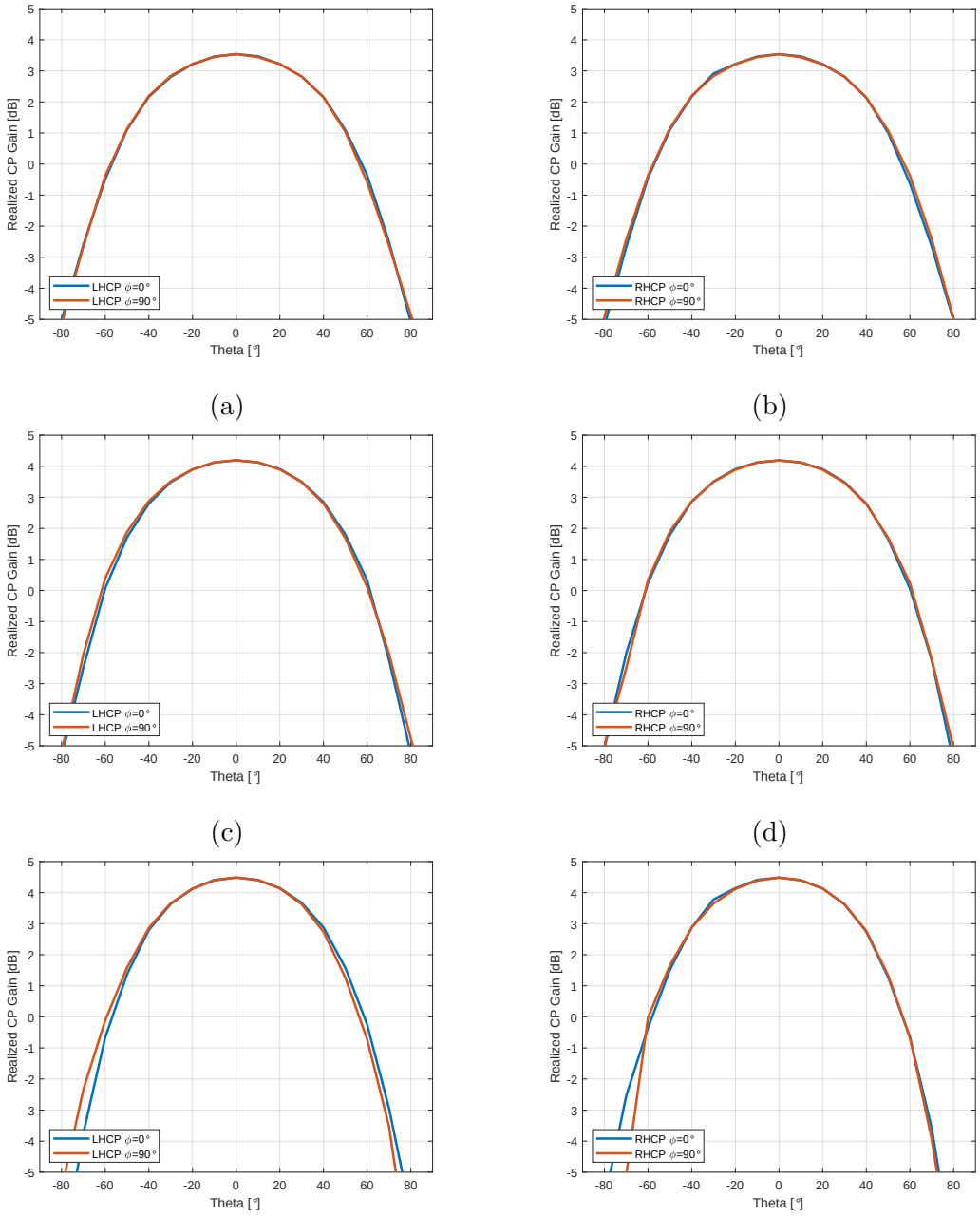


Figure 3.19: Circularly polarized realized gain of both principle azimuthal planes at (a)(b) 27.5 GHz, (c)(d) 29.5 GHz, and (e)(f) 31 GHz. The left column is LHCP while the right is RHCP.

3.4 Feed Network Design

In order to feed the BFICs, a power divider network was required to evenly distribute the RF signal to each device. As such, the 3-port network is used to generalize the divider. Microwave theory dictates that a 3-port network cannot simultaneously be lossless, reciprocal, and perfectly matched at all ports; at most, only two of these conditions can be satisfied at a time. A general representation of a 3-port network is shown in Fig. 3.20, where the incident and reflected waves at each port are defined, along with the associated reflection coefficients. The mathematical relationships governing these interactions are expressed in equation 3.4, while equations 3.5 and 3.6 provide further detail on the reflection coefficients observed at the input and outputs, respectively.

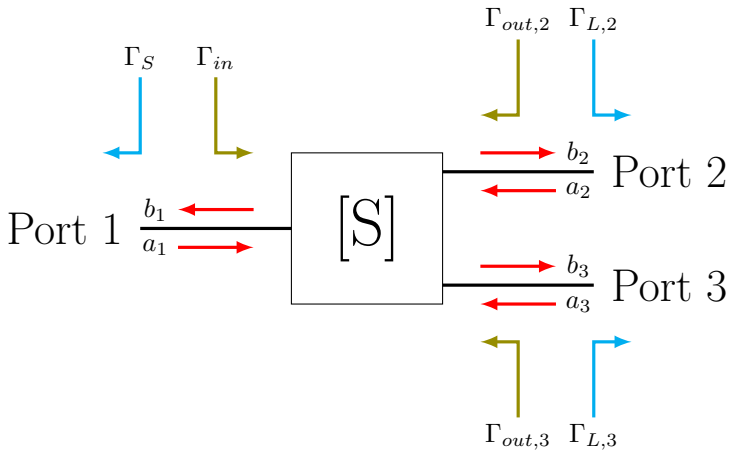


Figure 3.20: Block diagram of a 3-port network.

$$\begin{bmatrix} b_1 \\ b_2 \\ b_3 \end{bmatrix} = \begin{bmatrix} S_{11} & S_{12} & S_{13} \\ S_{21} & S_{22} & S_{23} \\ S_{31} & S_{32} & S_{33} \end{bmatrix} \begin{bmatrix} a_1 \\ a_2 \\ a_3 \end{bmatrix} \tag{3.4}$$

$$\Gamma_s = \frac{a_1}{b_1}, \Gamma_{in} = \frac{b_1}{a_1} \tag{3.5}$$

$$\Gamma_{L,i} = \frac{a_i}{b_i}, \Gamma_{out,i} = \frac{b_i}{a_i} \tag{3.6}$$

Assuming that ports 2 and 3 are driven by identical excitations ($a_2 = a_3$) and that the divider splits power equally ($S_{12} = S_{13}$), the input and output reflection coefficients can be expressed as shown in equation 3.7 and equation 3.8, respectively. Equation 3.7 indicates that the input reflection coefficient is influenced by both the load reflection and the S_{11}. This relationship highlights how mismatches at the outputs propagate back toward the source. This highlights how a poor load can create a mismatched input impedance which can propagate when multiple stages of dividers are cascaded.

Similarly, equation 3.8 demonstrates that the output reflection coefficient is a function of the return loss, the coupling between ports, and the source matching. Analogous to the input reflection coefficient, the output reflection coefficient is also dependent on the source reflection and S_{ii}. However, the output reflection coefficient also depends on the S_{ij}, the coupling or isolation. The presence of the coupling in the equation highlights the impact of the second output port on the reflection coefficient at the first and vice versa.

$$\Gamma_{in} = S_{11} + \frac{2S_{12}S_{21}\Gamma_{L,2}}{1 - (S_{22} + S_{23})\Gamma_{L,2}} \tag{3.7}$$

$$\Gamma_{out,i} = S_{ii} + S_{ij} + \frac{2S_{1i}S_{i1}\Gamma_s}{1 - S_{11}\Gamma_s} \tag{3.8}$$

3.4.1 Design Methodology of the Feed Network

For the feed network, it begins with the creation of a circuit model, simulated using Keysight Advanced Design System or any equivalent high-frequency linear circuit simulator. The circuit model provides insight into the ideal S-parameters and allows for initial evaluation of the divider's compatibility with system-level requirements. If needed, circuit-level simulations also facilitate the rapid generation and evaluation of large networks of dividers.

Once the divider topology has been selected, the design is implemented in HFSS to perform full-wave simulations. Initially, a single 1-to-2 divider is simulated, as it is impractical to tune the full multi-stage network due to the large size of the simulation model. After the 1-to-2 divider demonstrates S-parameters consistent with the circuit-level predictions, it is incorporated into a network arranged in an H-shaped corporate feed architecture. The S-parameters and reflection coefficients of the complete divider network are then evaluated to ensure compliance with system specifications. A flow chart of this process is detailed in Fig. 3.21.

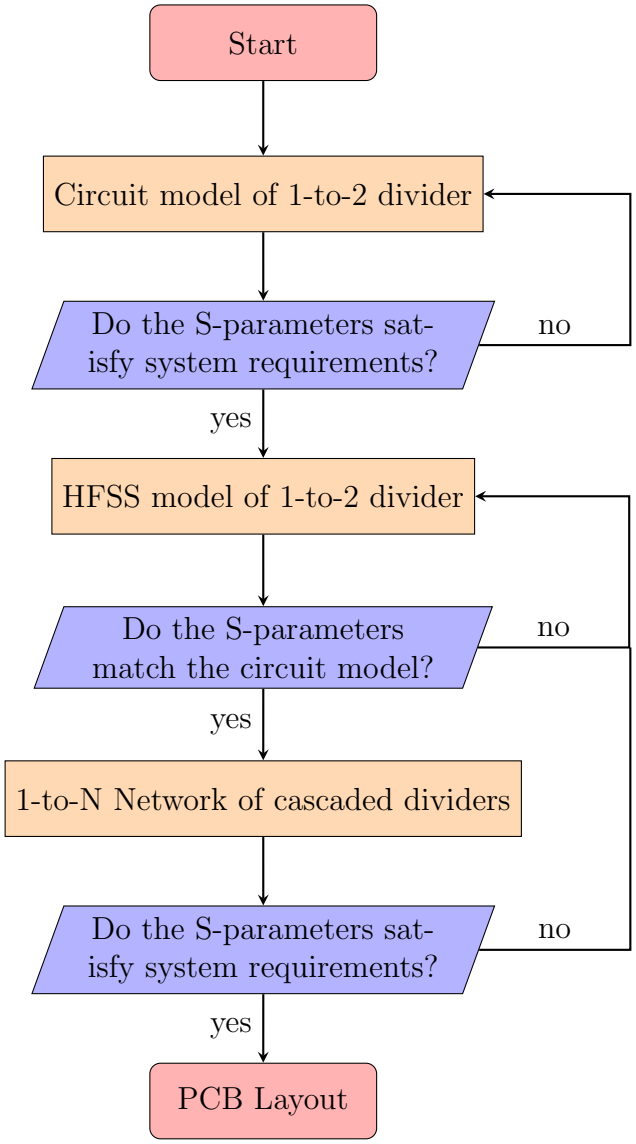


Figure 3.21: Proposed design methodology for the feed network.

3.4.2 Power Divider Topologies

Three candidate topologies were considered for the power divider: the resistive power divider, the lossless power divider and the Wilkinson power divider.

Resistive Power Divider

The RPD consists of resistors arranged to provide matched and reciprocal operation. The circuit model can be seen in Fig. 3.22 and the S-parameters are shown in equation 3.9. It can be seen that the transmission coefficients from the input port to either output port are $S_{1,2} = S_{1,3} = 0.5$, corresponding to -6 dB insertion loss. This implies that only 25% of the input power is delivered to each output port, while the remaining 50% is dissipated in the resistive elements. Although the RPD is simple and inherently broadband, the high insertion loss makes it unsuitable for feed networks in large antenna arrays where efficiency is critical.

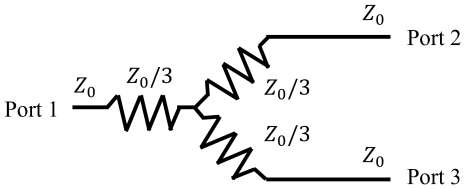


Figure 3.22: Circuit model of the RPD.

$$[S_{RPD}] = \begin{bmatrix} 0 & 1/2 & 1/2 \\ 1/2 & 0 & 1/2 \\ 1/2 & 1/2 & 0 \end{bmatrix} \tag{3.9}$$

Lossless Power Divider

As the name indicates, the LPD is reciprocal and ideally lossless in terms of power dissipation, but it is not matched at all ports. In the implementation considered here, the LPD is matched at the input port by sacrificing the matching at the output ports. The circuit model is shown in Fig. 3.23, where a 50 Ω transmission line is split into two 70.7 Ω $\lambda/4$ lines. The corresponding S-parameters are given in equation 3.10, which show that the input port is matched while the power division between the two outputs is equal, $S_{12} = S_{13} = -j/\sqrt{2}$, corresponding to half the power delivered to each output.

The return loss at the output ports is 0.5, confirming that the outputs are not individually matched. However, the effective reflection at the output depends on both the return loss S_{ii} and the mutual coupling S_{ij} between the output ports. In the case of the LPD, S_{ii} and S_{ij} are out of phase, leading to cancellation when the ports are excited simultaneously with equal amplitude and phase. This property enables the LPD to appear well-matched under uniform excitation.

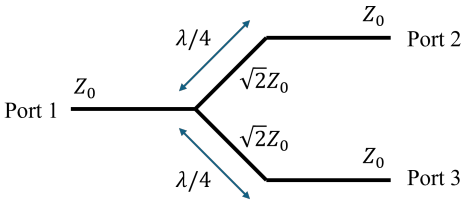


Figure 3.23: Circuit model of the LPD.

$$[S_{LPD}] = \begin{bmatrix} 0 & -j/\sqrt{2} & -j/\sqrt{2} \\ -j/\sqrt{2} & 1/2 & -1/2 \\ -j/\sqrt{2} & -1/2 & 1/2 \end{bmatrix} \tag{3.10}$$

Wilkinson Power Divider

The WPD builds upon the same fundamental circuit model as the LPD, with the key distinction being the addition of a 100 Ω isolation resistor bridging ports 2 and 3, as illustrated in Fig. 3.24. The corresponding theoretical S-parameters are given in equation 3.11. The WPD is matched at all ports, reciprocal, but is lossy. However, each output port still receives half of the input power, $S_{12} = S_{13} = -j/\sqrt{2}$, as in the LPD.

The lossy behaviour in the WPD arises from the added isolation resistor where it dissipates power only when there is an imbalance or reflection at the outputs, thereby preventing interaction between ports 2 and 3. This ensures that mismatches or reflections at one output do not degrade the performance of the other, a property that makes the WPD especially attractive for array feed networks. Unlike the LPD, the output reflection coefficient in the WPD does not rely on cancellation between S_{ii} and S_{ij} terms; instead, each port is inherently well matched.

$$[S_W] = \begin{bmatrix} 0 & -j/\sqrt{2} & -j/\sqrt{2} \\ -j/\sqrt{2} & 0 & 0 \\ -j/\sqrt{2} & 0 & 0 \end{bmatrix} \tag{3.11}$$

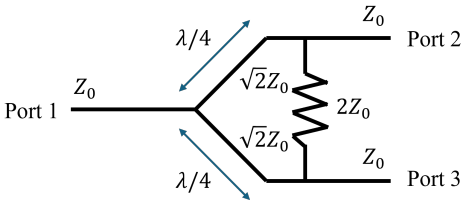


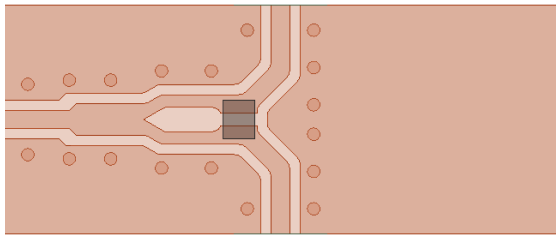
Figure 3.24: Circuit model of the WPD.

3.4.3 Design of Power Divider Network

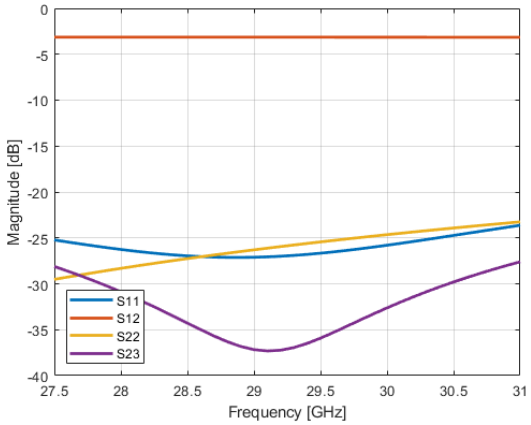
A 1-to-2 WPD was implemented in HFSS using CPWG as the transmission line, with the layout shown in Fig. 3.25a. There are three ways to model the resistor: the first is to use the physical resistor with its material properties; the second is to use two lumped ports paired with the S-parameters provided by the manufacturer; the third is to use an ideal resistor sheet. The first method is the most accurate, capturing the actual discontinuities and material interactions, however the model was not available. The third method is an idealistic model that does not capture the geometry of the resistor and only the parasitics from the pads. The second method does a better job of capturing the resistor geometry using measured data provided from the vendor.

In earlier iterations of the divider, -12 dB input matching was achieved in the cascaded network. Even though this satisfied the requirements, to account for manufacturing tolerances, the author aimed to improve the input matching. To improve input matching, a stepped-impedance section was introduced at port 1, improving the return loss from -13 dB to -23 dB. The WPD was forced to be integrated on the bottom layer of the PCB stack-up to accommodate a surface-mount implementation of the resistor. The simulated S-parameters, presented in Fig. 3.25b, demonstrate return losses below -23 dB at both input and output ports, with isolation better than -28 dB across the operational frequency band.

The WPD was subsequently extended to a 1-to-64 divider to feed 64 BFICs following a H-shaped corporate feed methodology. The layout, shown in Fig. 3.26, occupies a 90 mm $\times$ 90 mm footprint and incorporates 63 individual WPDs interconnected via CPWGs. The input return loss remained below -15 dB while the output return loss was below -20 dB across the band, as seen in Fig. 3.27a. Compared to the 1-to-2 divider, the return loss at both input and output ports has slightly degraded due to the non-zero reflection at the load and source of each stage. This issue propagates and worsens as more division stages are cascaded. The transmission response exhibited a magnitude of approximately -20 dB, as seen in Fig. 3.27b. This is roughly 2 dB below the ideal division, which is



(a)



(b)

Figure 3.25: (a) HFSS layout of the 1-to-2 WPD. (b) Simulated S-parameters of the 1-to-2 WPD.

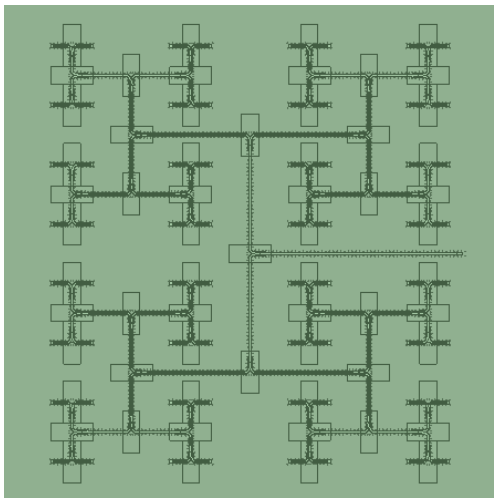


Figure 3.26: HFSS layout of the 1-to-64 WPD network where each stage is connected using CPWG.

due to conductor and dielectric losses inherent to the PCB materials. Isolation between adjacent output ports remained below −26 dB, as shown in Fig. 3.27c.

As previously noted, the output reflection coefficient in a WPD is independent of the phase relationship between S_{22} and S_{23}, both ideally being zero. Simulated output reflections were approximately −12 dB across the band, as illustrated in Fig. 3.28a under uniform excitation ($a_2 = a_3 = a_i$). When a tapered amplitude distribution was applied, the worst-case output reflection increased to −7 dB, while the average remained near −17 dB. These results demonstrate that the WPD network maintains acceptable matching under tapering conditions.

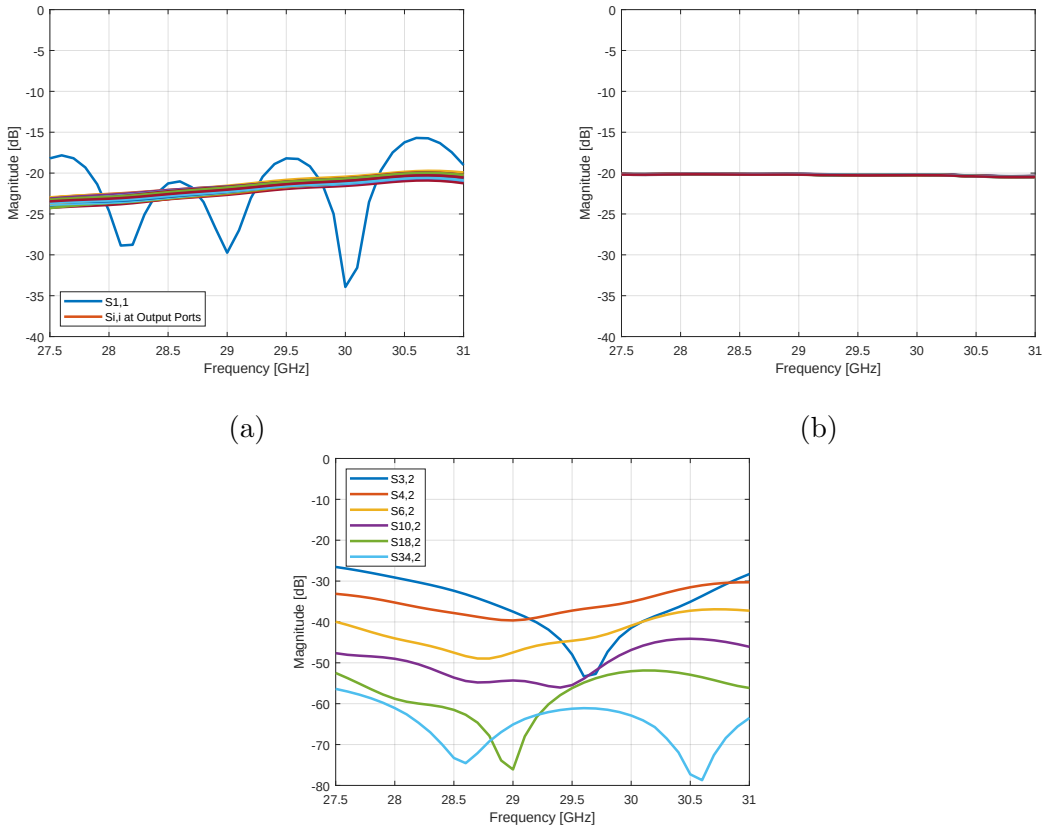
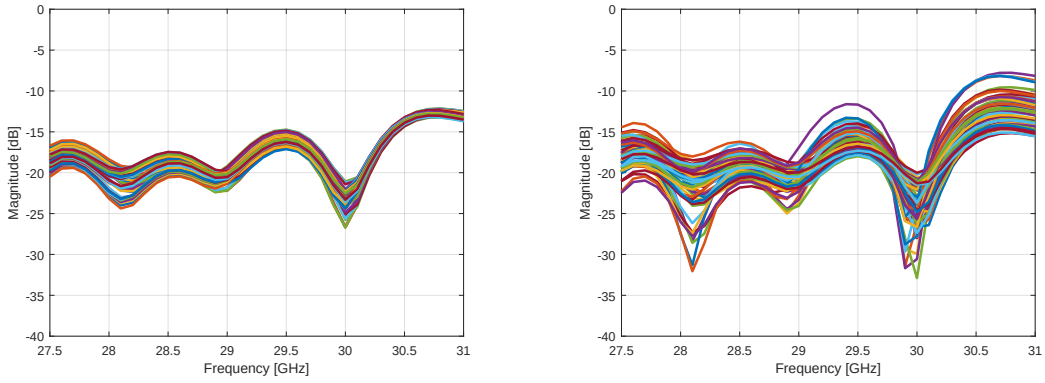


Figure 3.27: S-parameters of the designed 1-to-64 WPD network. (a) Return losses. (b) Through. (c) Isolation from port 2.



(a) (b)

Figure 3.28: Output reflection coefficient of the 1-to-64 WPD (a) with uniform excitation, (b) array tapering.

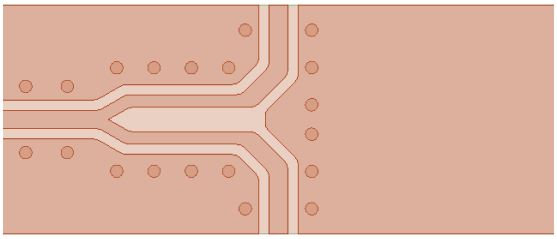
Wilkinson Power Divider vs Lossless Power Divider

For comparison, the same design methodology was applied to the LPD. A 1-to-2 LPD was implemented, with the layout shown in Fig. 3.29a. The simulated S-parameters, presented in Fig. 3.29b, indicate that the input port is well matched, with a return loss better than -25 dB across the band. The transmission coefficient, $S_{1,2}$, is approximately -3 dB, confirming equal power division between ports 2 and 3. However, the return loss and isolation at the output ports are poor, both around -6 dB which is expected.

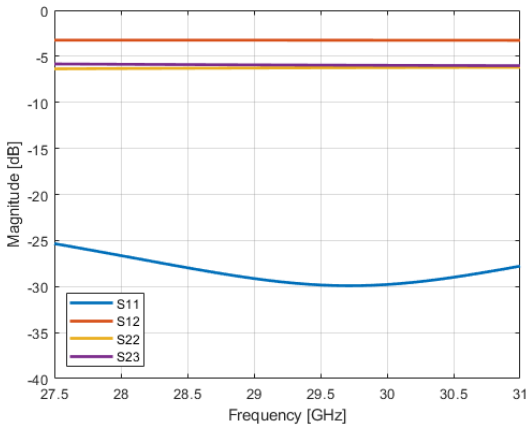
Extending this to a 1-to-64 LPD network, the S-parameters are shown in Fig. 3.30. The input port remains well matched, with a return loss below -15 dB across the operational band, as illustrated in Fig. 3.30a. The transmission magnitude was observed to be -20 dB, approximately 2 dB below the ideal division, as seen in Fig. 3.30b. These results are similar to the WPD for the input port and transmission performance.

At the output ports, the return loss remains around -6 dB. Fig. 3.30c shows the isolation between output ports in different sections of the feed network. Adjacent ports exhibit isolation near -6 dB, improving by approximately 6 dB for more distant port pairs, consistent with theoretical expectations for a LPD.

Similar to the WPD, Fig. 3.31a shows that the output reflection coefficient remains below -15 dB under uniform excitation ($a_2 = a_3 = a_i$). However, when amplitude tapering is applied across the array, the output reflection coefficients degrade significantly, as shown in Fig. 3.31b. Several ports exhibit poor matching, with reflections reaching up to -3 dB



(a)



(b)

Figure 3.29: (a) HFSS layout of the 1-to-2 LPD. (b) Simulated S-parameters of the 1-to-2 LPD.

and large variations between ports. This highlights a fundamental limitation of the LPD. While LPDs can perform well under uniform excitation, its output reflection coefficient drastically deteriorates under non-uniform excitations, due to the poor isolation.

In contrast, the WPD has superior resilience to load modulation. Whereas the LPD is highly sensitive to variations, the WPD architecture maintains both matching across all output ports, even in the presence of tapering. This robustness makes the WPD a more reliable and practical choice for large-scale phased array feed networks.

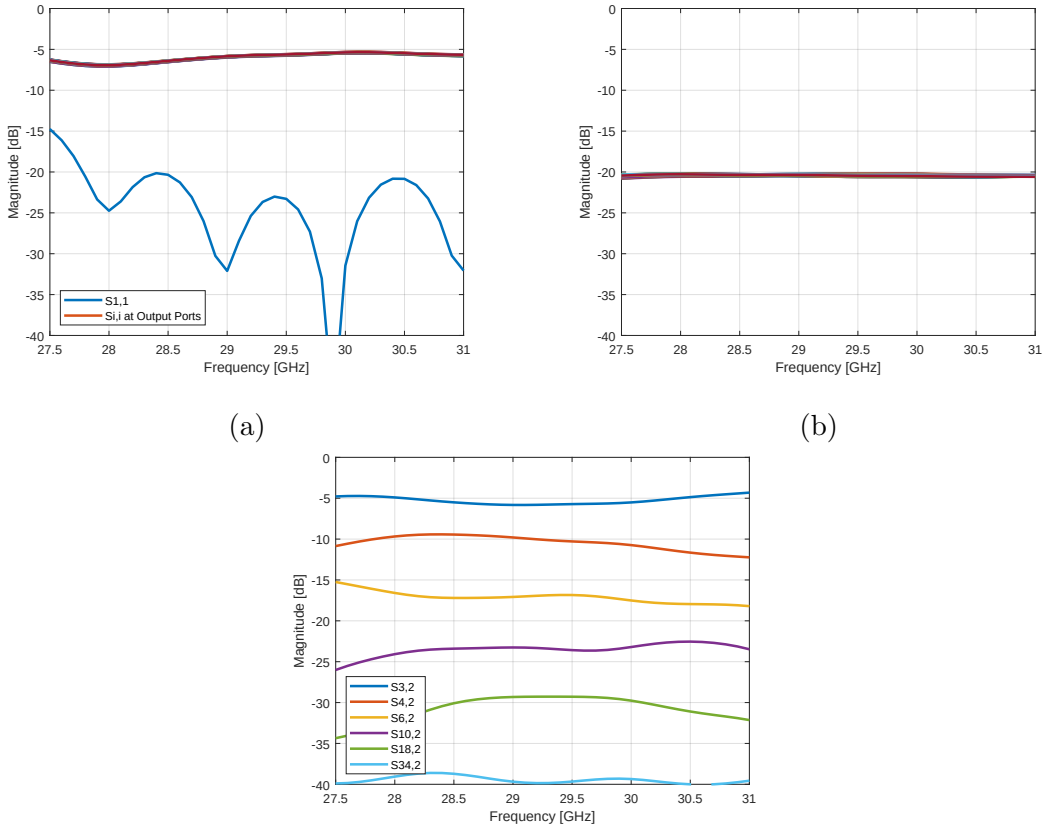
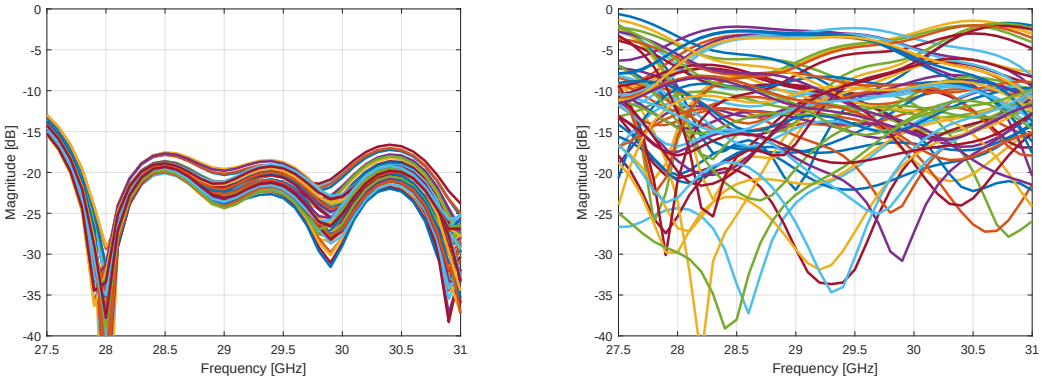


Figure 3.30: S-parameters of the 1-to-64 LPD network. (a) Return losses. (b) Through. (c) Isolation at port 2.



(a) (b)

Figure 3.31: Output reflection coefficients of the 1-to-64 LPD network (a) with uniform excitation, and (b) with array tapering.

Chapter 4

16 × 16 Active Phased Array Antenna Analysis

The design of the active PAA requires careful consideration beyond the RF front-end and the antenna elements themselves. Given the integration of a large number of BFICs, the overall system performance is influenced not only by the RF design but also by other components necessitated by the BFIC. Specifically, the PCB layout must accommodate four critical domains: RF routing, DC power distribution, digital signal integrity, and thermal management. To address these requirements, layers 1 through 9 are allocated for the antenna, layer 10 serves as the power plane, layer 11 is dedicated to ground, and layer 12 houses the feeding network. Digital signal routing is distributed across layers 10 to 12. The following sections present an analysis of each domain, supported by full-wave and circuit simulations, and describe the solutions implemented to satisfy the RF, DC, signal integrity, and thermal requirements of the array.

4.1 System Architecture

The designed feeding network of WPD distributes a single input signal equally into 64 outputs with a conversion gain of -20 dB. Each output feeds into a BFIC each which feed into four antennas. Each BFIC has eight outputs where two outputs feed a single antenna, one for each polarization. The overall architecture can be seen in Fig. 4.1. The design of both the feed network and antenna elements were covered previously in chapter 3.

The selected BFIC is an off-the-shelf transmitter chip operating across 27.5–31 GHz, equipped with a single RF input and eight RF outputs. Each RF chain incorporates an

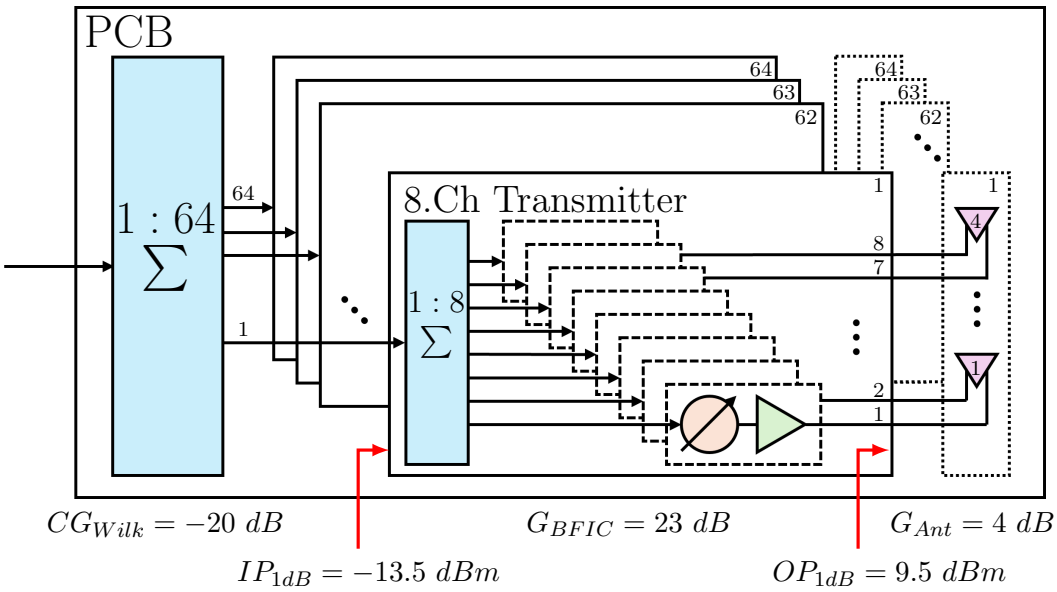


Figure 4.1: Block diagram of the RF architecture of the 16 × 16 active PAA.

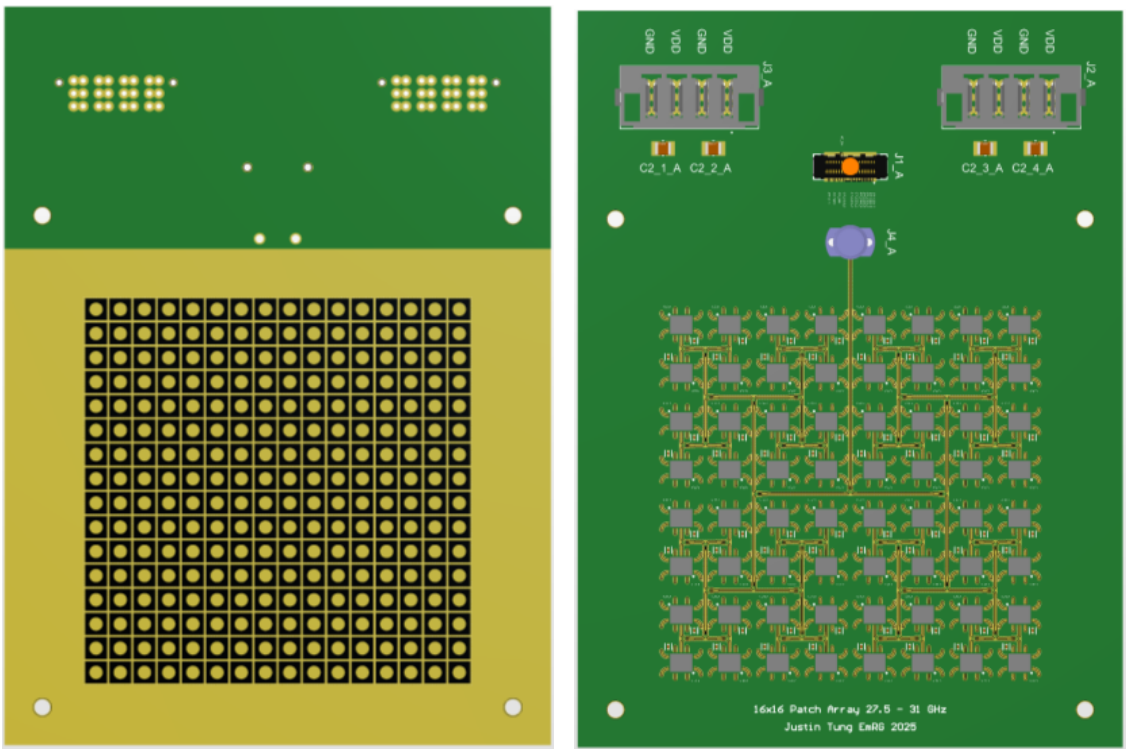
independent phase shifter and power amplifier, thereby enabling per-channel control of both phase and amplitude. Configuration is achieved through a SPI, which programs the phase and gain settings in each chain. The BFIC was selected primarily for its high level of integration and compact footprint of 4.39 mm × 3.59 mm. A further advantage lies in its use of a common supply voltage for both digital and RF circuits, which simplifies the power distribution network and facilitates system-level integration. The OP_{1dB} of one channel in the BFIC is 9.5 dBm, as such the peak EIRP is calculated to be 40.5 dBm in equation 4.1.

$$\begin{aligned} EIRP_{1dB} &= OP_{1dB} + G_{Ant} + G_{Array} + 10\log(N_{pol}) \\ &= OP_{1dB} + G_{Ant} + 10\log(N) + 10\log(N_{pol}) \\ &= 9.5\ \text{dBm} + 4\ \text{dB} + 24\ \text{dB} + 3\ \text{dB} = 40.5\ \text{dBm} \end{aligned} \tag{4.1}$$

where

$EIRP_{1dB}$	:	EIRP at the 1 dB compression point
OP_{1dB}	:	output power at the 1 dB compression point
G_{Ant}	:	gain of the antenna element
G_{Array}	:	gain of the array
N_{pol}	:	number of active ports in the antenna
N	:	number of antennas in the array

The PCB layout of the antenna array is presented in Fig. 4.2. The top side hosts the 16×16 antenna array, the circular patch and cavities are visible on the top layer. The bottom side accommodates the WPD network, BFICs, input/output connectors, and power connectors. This arrangement isolates the radiating elements from the active components, while also enabling routing and minimizing undesired coupling between RF and digital subsystems.



(a) (b)

Figure 4.2: PCB layout of the designed active PAA. (a) Top side. (b) Bottom side.

4.2 DC Power Analysis

The BFICs operate from a single 1.2 V supply that powers both the digital and RF sections of the chip. To distribute power effectively across the board, two high-current connectors were selected based on the current-carrying capacity of both the connectors and their associated cables. At peak operation, each BFIC draws 575 mA at P_{1dB}, resulting in a maximum total board current of 36.8 A. Each connector consists of four blades, with two allocated to the 1.2 V rail and two to ground. Given that each blade is rated up to 28 A, the expected current per blade of 9.6 A remains within the safe operating limits, ensuring reliable power delivery.

Due to the relatively high current demand, layer 10 was designated as the 1.2 V power plane. However, routing constraints introduced by digital control signals necessitated partial use of this layer for signal traces. As a result, the current flows along the edges of the board from the connector, feeding each row of BFICs. As such, the largest voltage drop occurs at the ends of the first row, where the cumulative current is greatest. To mitigate this, additional copper area was allocated along the board edges, reducing current density and minimizing voltage drops.

To evaluate the impact of this compromise, the design was exported to Ansys SIwave for voltage drop analysis. In the DC simulation, the connectors are modeled as 1.2 V voltage sources while each BFIC was modeled as a current source drawing 575 mA. The resulting voltage distribution across the power plane is shown in Fig. 4.3. The analysis indicates that the worst-case BFIC receives an input voltage of 1.153 V, corresponding to a voltage drop of less than 4% from the nominal supply. This is within the specified ±10% tolerance range. These results confirm that the power plane design provides sufficient margin to ensure stable operation of all BFICs under maximum load conditions.

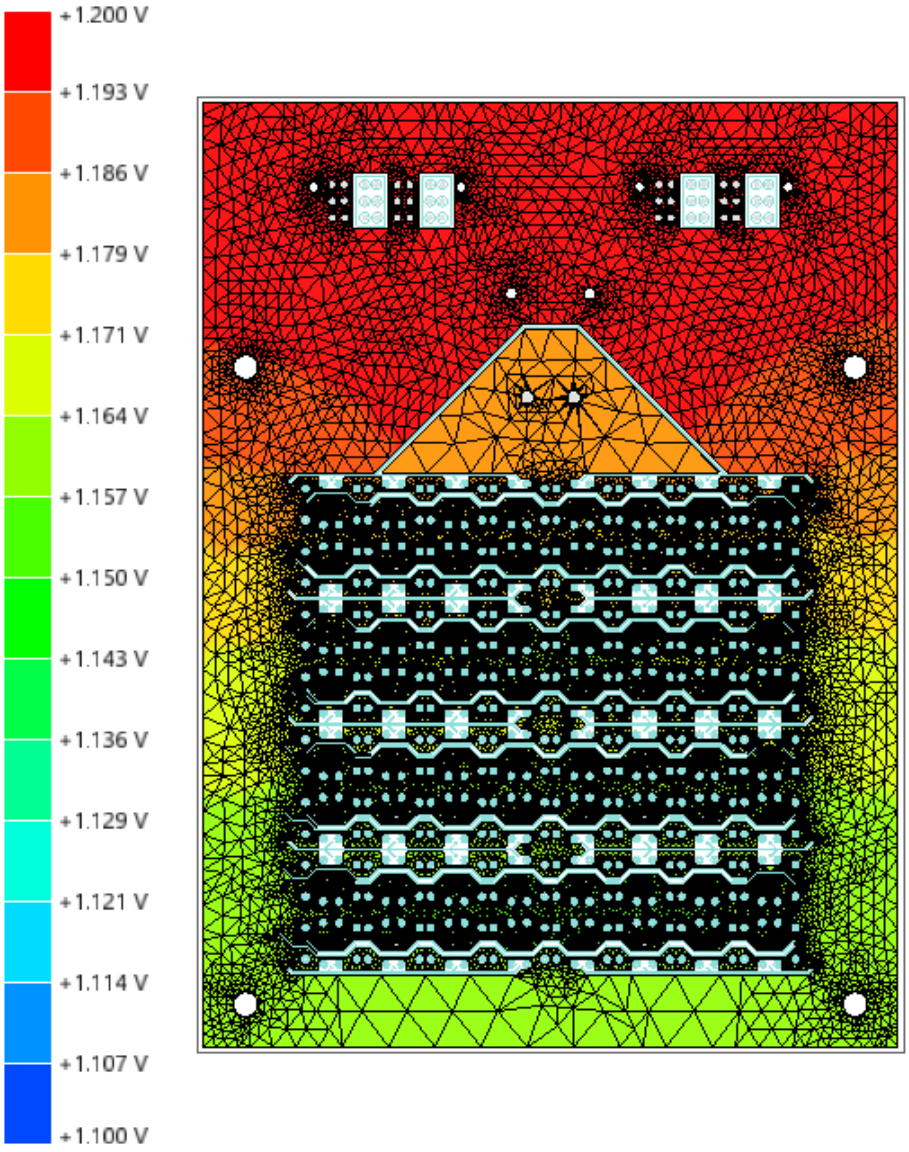


Figure 4.3: Layer 10 of the DC simulation of the antenna array.

4.3 Signal Integrity Analysis

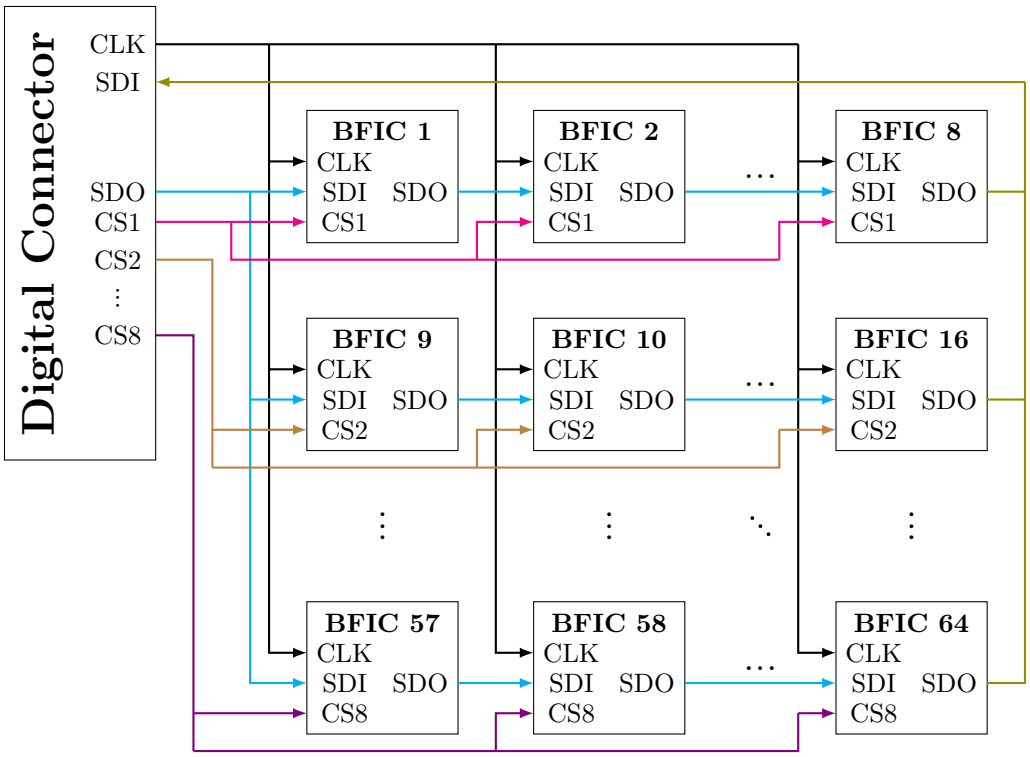


Figure 4.4: Block diagram of a SPI connections from the connector to the BFICs.

The BFICs are configured and controlled through a SPI protocol. The protocol comprises four primary signals: CLK, SDO, SDI, and CS. For the array implementation, eight CSs (CS[1:8]) are used to address eight daisy chains of BFICs, with each chain consisting of eight devices. When a specific CS line is asserted, the corresponding chain is activated while all others remain idle. Within each chain, the SDO and SDI signals are shared. The controller drives the SDO line, which fans out to the first BFIC in each chain. Conversely, the SDI line is driven by the selected BFIC and routed back to the controller. Since the SDI net is shared among all chains, high-impedance tri-state buffers within each BFIC ensure that only the selected device drives the line, thereby preventing contention. The CLK is distributed globally to all 64 BFICs, driven by the controller.

Signal integrity of the SPI network was analyzed through transient simulations, at a CLK frequency of 500 kHz. The results are shown in Fig. 4.5, where the eye diagrams of the SDI, SDO, and CS lines demonstrate clean transitions and well-defined logic levels at

the driver and receiver ends. However, the global CLK distribution exhibited noticeable degradation. While the voltage thresholds were still satisfied, the CLK showed significantly slower rise and fall times compared to the data and CS lines. This degradation arises from the cumulative capacitive loading of the 64 BFIC inputs, with each ball-grid-array connection contributing approximately 20 pF. The total capacitance directly impacts edge rates, resulting in extended transition times. Furthermore, resistive losses along the clock trace caused the signal amplitude to drop from 1.2 V to approximately 0.95 V at the farthest BFIC.

Although operation at 500 kHz is well within specification, these effects indicate that the CLK signal becomes the primary limiting factor as the operating frequency increases. Without additional measures, reliable communication cannot be guaranteed at higher speeds. A potential solution, as used in [27, 28], is to introduce buffers within each daisy chain. This approach reduces capacitive loading by segmenting the distribution network, thereby restoring signal integrity and enabling operation at higher CLK frequencies.

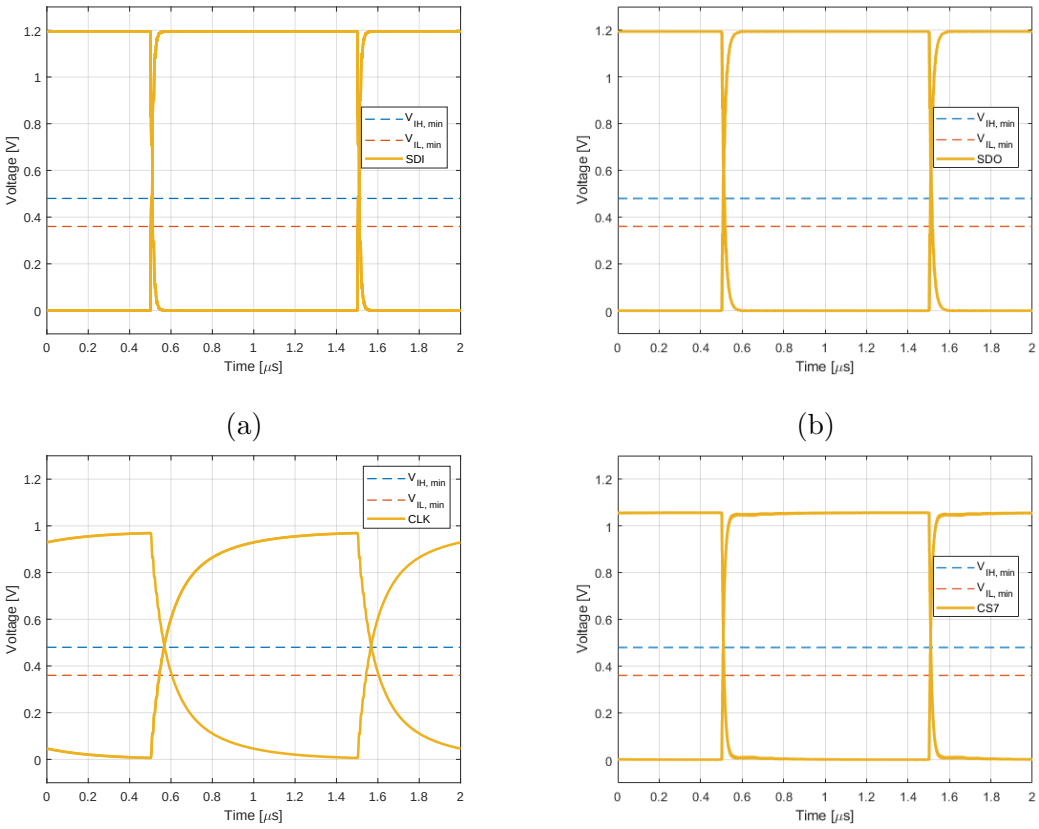


Figure 4.5: Eye diagrams from transient simulations of the digital control signals are shown, where the yellow trace corresponds to the simulated waveform, the blue line indicates the minimum threshold for a logic-high level, and the orange line indicates the minimum threshold for a logic-low level. (a) Signal received at the connector when the furthest BFIC is driving the SDI net. (b) Signal received at the furthest BFIC when the connector is driving the SDO net. (c) Signal received at the furthest BFIC when the connector is driving the CLK signal. (d) Signal received at the furthest BFIC when the connector is driving the longest CS signal.

4.4 Thermal Analysis

To ensure reliable operation, the BFICs must be maintained within the specified temperature range of -40°C to 85°C. Proper thermal regulation ensures compliance with datasheet requirements which is determined to extend device lifespan and improve performance consistency across the array.

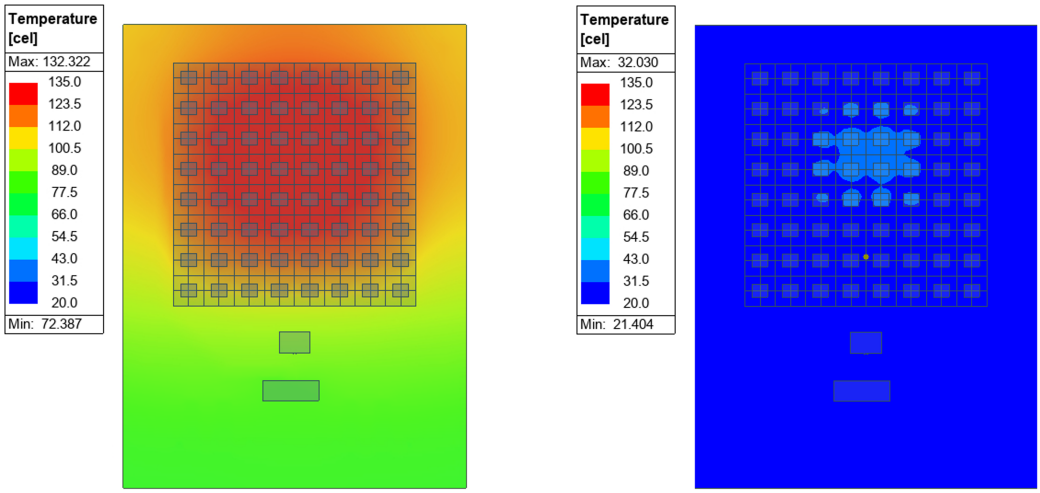
In SATCOM applications, 16-QAM modulation schemes are becoming standard [32], resulting in an expected peak-to-average power ratio of approximately 6 dB. With an OP_{1dB} of 9.5 dBm, the average output power of each channel is 3.5 dBm, 6 dB below the peak. Under these operating conditions, each BFIC is estimated to consume approximately 520 mW, of which 250 mW is attributed to the power amplifiers, and 270 mW for digital and analog circuitry. Assuming the power amplifiers operate in class AB, the efficiency is estimated to be 30% at 6 dB back off. As such, the dissipated power per BFIC is approximated as 445 mW.

$$P_{out,avg} = OP_{1dB} - PAPR \approx 9.5\ dBm - 6\ dB = 3.5\ dBm \tag{4.2}$$

$$P_{diss} = P_{control} + (1 - \eta_{BO})P_{PA} = 270\ mW + 0.7 \times 250\ mW = 445\ mW \tag{4.3}$$

A thermal simulation was conducted using Ansys Icepak, with each BFIC modeled to dissipate 500 mW, to provide some margin of error. The BFICs were modeled with a thermal resistance of $5.5°C/W$ as specified in the datasheet. The simulation environment assumed still air at an ambient temperature of 20°C. The results, shown in Fig. 4.6a, indicated significant overheating, with the central BFICs reaching a peak temperature of 133°C, while the coolest devices operated at 92°C. These temperatures exceed the allowable operating range, confirming the necessity for additional cooling.

To mitigate this, a mechanical enclosure was designed to serve both as a thermal management solution and structural support for the array. The enclosure, designed from aluminum, was mounted to the PCB using screws, and commercially available heatsinks were attached to its backside to further enhance heat dissipation, as shown in Fig. 4.7. A subsequent thermal simulation was performed including the aluminum case, heatsinks, and a small cooling fan. As shown in Fig. 4.6b, the results demonstrated a substantial improvement: the hottest BFICs reached only 32°C, while the coolest BFICs remained close to ambient temperature. These results confirm that the proposed thermal management solution provides sufficient margin to keep all BFICs within their specified operating range.



(a) (b)

Figure 4.6: Ansys Icepak thermal simulations of the antenna array (a) without any cooling devices, (b) with a case, heatsink and fan.

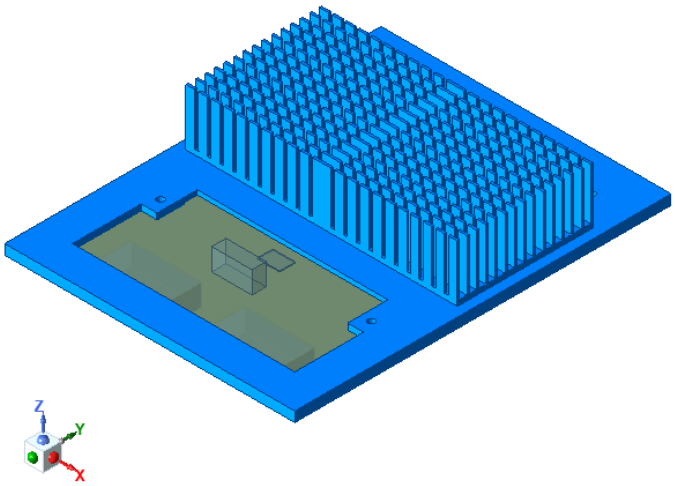


Figure 4.7: The designed aluminum case with heatsinks glued onto the back to cool the antenna array.

Chapter 5

Conclusion and Future Works

5.1 Conclusion

This thesis has presented the design, implementation, and analysis of a 16×16 Ka-band active PAA for SATCOM applications. The work addressed the end-to-end design challenges spanning antenna element development, RF feed network synthesis, power delivery, digital control analysis, and thermal analysis within a compact and manufacturable PCB.

A systematic antenna design methodology was introduced, beginning with open boundary simulations to capture first-order element behavior, followed by periodic boundary analysis to incorporate mutual coupling and assess scan performance. This approach provided a practical and accurate means of predicting large-array behavior without resorting to prohibitively expensive full-array simulations. The resulting antenna elements achieved the required -10 dB impedance bandwidth and 3 dB axial ratio from 27.5–31 GHz, while supporting beam scanning up to $\pm 70^{\circ}$ with worst case scan loss of 7.5 dB at the upper frequency.

The feed network was developed using both circuit and full-wave simulations, with comparisons drawn between WPD and LPD topologies. While both achieved comparable transmission characteristics, the WPD structure demonstrated resiliency to non-uniform excitation, establishing it as the more robust architecture for large-scale phased arrays.

System-level integration required careful consideration of other equally important subsystems. A power delivery network was designed and validated, ensuring voltage drops remained within tolerance under full load conditions. Digital control signals were verified for integrity across the array. Thermal simulations revealed that passive cooling was insufficient, necessitating the design of an aluminum case with heatsinks and active cooling.

This solution reduced the maximum BFIC temperature from 133°C to 32° under realistic operating conditions, ensuring long-term device reliability.

The proposed methodology demonstrates a path toward the practical realization of large, active PAA for next-generation SATCOM terminals. By being able to evaluate EM, RF, power, digital, and thermal performance, the design is able to meet the requirements of Ka-band SATCOM systems.

5.2 Future Works

- **Validation of proposed methodology from measurements:** The proposed design methodology has been verified using simulations; however, experimental measurements are necessary to fully validate its accuracy and practical viability.
- **Improving scan loss in large PAAs:** The designed active array experiences a scan loss of -7.5 dB at $\theta = 70°$, which is approximately 3 dB greater than the theoretical $\cos(70°)$ reference. This degradation arises from the element radiation pattern and active return loss. Solutions proposed in the literature include employing antenna structures with wider element patterns, such as magneto-electric dipoles, or incorporating wide-angle impedance matching (WAIM) layers to reduce mutual coupling and load modulation effects during beam steering.
- **Cost reduction through alternative stack-ups:** A significant portion of the array cost originates from the 12-layer HDI PCB stackup. Cost can potentially be reduced by separating the antenna and active circuits onto two PCBs with lower layer count. However, this approach requires careful design of the interconnect transition. Possible solutions reported in the literature include flip-chip BGA integration or conductive adhesive interconnects.
- **32×32 Active PAA:** While the 16×16 array met system requirements, scaling to larger arrays introduces new challenges. Increased current draw will exacerbate voltage drops, requiring optimized power source placement. Clock distribution will further degrade as more BFICs are connected, suggesting the use of clock buffers. Additionally, the increase of BFICs will increase thermal coupling, necessitating more aggressive cooling strategies.
- **Large active PAA with near-field probes:** Manufacturing variations in the PCB and BFICs can lead to performance inconsistencies between antenna channels. To

maximize system performance, calibration techniques are proposed which require a feedback mechanism, such as near-field probes that can be used to characterize each antenna chain and enable precise correction.

- **Large active PAA with multi-beam capabilities:** Future LEO SATCOM systems may require multi-beam operation to enable seamless satellite handovers. This significantly increases design complexity, as it requires multiple RF feed networks and potentially larger BFICs to support RF signal mixing. Such implementations may necessitate a revised PCB stackup or a multi-board architecture.

References

[1] Shanzhi Chen, Ying-Chang Liang, Shaohui Sun, Shaoli Kang, Wenchi Cheng, and Mugen Peng. Vision, requirements, and technology trend of 6g: How to tackle the challenges of system coverage, capacity, user data-rate and movement speed. *IEEE Wireless Commun.*, 27(2):218–228, 2020.

[2] Shanzhi Chen, Shaohui Sun, and Shaoli Kang. System integration of terrestrial mobile communication and satellite communication —the trends, challenges and key technologies in b5g and 6g. *China Communications*, 17(12):156–171, 2020.

[3] C.A. Balanis. Antenna theory: A review. *Proc. IEEE*, 80(1):7–23, 1992.

[4] Constantine A. Balanis. *Antenna Theory: Analysis and Design*. John Wiley & Sons, 4th edition, 2016.

[5] HyperPhysics. Classical polarization of light. http://hyperphysics.phy-astr.gsu.edu/hbase/phyopt/polclas.html. Accessed: Nov. 1, 2025.

[6] W.S.T. Rowe and R.B. Waterhouse. Edge-fed patch antennas with reduced spurious radiation. *IEEE Trans. Antennas Propag.*, 53(5):1785–1790, 2005.

[7] R. Munson. Conformal microstrip antennas and microstrip phased arrays. *IEEE Trans. Antennas Propag.*, 22(1):74–78, 1974.

[8] R. B. Waterhouse and D. Novak. A technique to enhance the impedance response of probe-fed stacked patch antennas. In *2017 IEEE International Symposium on Antennas and Propagation & USNC/URSI National Radio Science Meeting*, pages 2317–2318, 2017.

[9] Telesphor Kamgaing, Adel A. Elsherbini, Sasha N. Oster, and Emanuel Cohen. Low-profile fully integrated 60 ghz 18 element phased array on multilayer liquid crystal

polymer flip chip package. In *2015 IEEE 65th Electronic Components and Technology Conference (ECTC)*, pages 994–998, 2015.

[10] Yun Wang, Rui Wu, Jian Pang, Dongwon You, Ashbir Aviat Fadila, Rattanan Saengchan, Xi Fu, Daiki Matsumoto, Takeshi Nakamura, Ryo Kubozoe, Masaru Kawabuchi, Bangan Liu, Haosheng Zhang, Junjun Qiu, Hanli Liu, Naoki Oshima, Keiichi Motoi, Shinichi Hori, Kazuaki Kunihiro, Tomoya Kaneko, Atsushi Shirane, and Kenichi Okada. A 39-ghz 64-element phased-array transceiver with built-in phase and amplitude calibrations for large-array 5g nr in 65-nm cmos. *IEEE J. Solid-State Circuits*, 55(5):1249–1269, 2020.

[11] Kevin Erkelenz, Noah Sielck, Alexander Koelpin, and Arne F. Jacob. A hybrid-integrated k-/ka-band phased array module with dual-polarized shared aperture. *IEEE Trans. Microw. Theory Techn.*, 72(10):6130–6139, 2024.

[12] C.L. Mak, K.M. Luk, K.F. Lee, and Y.L. Chow. Experimental study of a microstrip patch antenna with an l-shaped probe. *IEEE Trans. Antennas Propag.*, 48(5):777–783, 2000.

[13] William J. Lambert, Arnaud L. Amadjikpe, Jimin Yao, Sri Chaitra J. Chavali, Peter Sagazio, Ye Seul Nam, Marwan Abu-Mahaimed, and Stefano Pellerano. Scalable multichip packaging with integrated antenna array for a 73-ghz transceiver ic. *IEEE Trans. Microw. Theory Techn.*, 69(1):387–398, 2021.

[14] Dongjin Jung, Chan-Ju Park, Taek Sun Kwon, Jung Woo Seo, Byungkuon Ahn, Sang-Hyuk Wi, and Ilju Na. Terahertz antenna-in-package design and measurement for 6g communications systems. *IEEE Trans. Antennas Propag.*, 72(2):1085–1096, 2024.

[15] Haiyang Xia, Zhiqiang Liu, Huan Liu, Tao Zhang, Fei Wang, Xianqin Hu, Xu Wu, Lianming Li, and Zhigong Wang. A cost-effective wideband dual-polarized l-shaped probe-fed phased array antenna for 60-ghz aip applications. *IEEE Trans. Compon., Packag. Manuf. Technol.*, 13(11):1790–1803, 2023.

[16] R. B. Waterhouse. *Microstrip Patch Antennas: A Designer's Guide*. Kluwer Academic Publishers, Boston, MA, 2003.

[17] S.D. Targonski, R.B. Waterhouse, and D.M. Pozar. Design of wide-band aperture-stacked patch microstrip antennas. *IEEE Trans. Antennas Propag.*, 46(9):1245–1251, 1998.

[18] José D. Díaz, Jorge L. Salazar-Cerreno, Javier A. Ortiz, Nafati A. Aboserwal, Rodrigo M. Lebrón, Caleb Fulton, and Robert D. Palmer. A cross-stacked radiating antenna with enhanced scanning performance for digital beamforming multifunction phased-array radars. *IEEE Trans. Antennas Propag.*, 66(10):5258–5267, 2018.

[19] Tobias Chaloun, Volker Ziegler, and Wolfgang Menzel. Design of a dual-polarized stacked patch antenna for wide-angle scanning reflectarrays. *IEEE Trans. Antennas Propag.*, 64(8):3380–3390, 2016.

[20] Xuanfeng Tong, Zhi Hao Jiang, Chao Yu, Fan Wu, Xin Xu, and Wei Hong. Low-profile, broadband, dual-linearly polarized, and wide-angle millimeter-wave antenna arrays for ka-band 5g applications. *IEEE Antennas Wireless Propagat. Lett.*, 20(10):2038–2042, 2021.

[21] Sanghamitro Das, Satish Kumar Sharma, Seth W. Waldstein, James M. Downey, Bryan L. Schoenholz, Sarah M. Dever, James A. Nessel, and Rudraishwarya Banerjee. A flat-panel 8×8 wideband k-/ka-band dual circularly polarized phased array antenna for cubesat communications. *IEEE Trans. Antennas Propag.*, 71(5):4153–4166, 2023.

[22] Rudraishwarya Banerjee, Satish Kumar Sharma, Seth W. Waldstein, James M. Downey, Bryan L. Schoenholz, Sarah M. Dever, James A. Nessel, and Sanghamitro Das. A 22–28 ghz polarization-reconfigurable flat-panel 8×8 tx/rx phased array antenna with uniquely arranged novel radiating elements for cubesat communication. *IEEE Trans. Antennas Propag.*, 71(5):4138–4152, 2023.

[23] Kevin Kai Wei Low, Samet Zihir, Tumay Kanar, and Gabriel M. Rebeiz. A scalable switchable dual-polarized 256-element ka-band satcom transmit phased-array with embedded rf driver and $\pm 70^\circ$ beam scanning. In *2020 IEEE/MTT-S International Microwave Symposium (IMS)*, pages 821–824, 2020.

[24] Xiaoxiong Gu, Duixian Liu, and Bodhisatwa Sadhu. Packaging and antenna integration for silicon-based millimeter-wave phased arrays: 5g and beyond. *IEEE J. Microwaves*, 1(1):123–134, 2021.

[25] Bodhisatwa Sadhu, Arun Paidimarri, Duixian Liu, Mark Yeck, Caglar Ozdag, Yujiro Tojo, Wooram Lee, Kevin Xiaoxiong Gu, Jean-Olivier Plouchart, Christian W. Baks, Yusuke Uemichi, Sudipto Chakraborty, Yo Yamaguchi, Ning Guan, and Alberto Valdes-Garcia. A 24–30-ghz 256-element dual-polarized 5g phased array using fast on-chip beam calculators and magnetoelectric dipole antennas. *IEEE J. Solid-State Circuits*, 57(12):3599–3616, 2022.

[26] Z. Yang et al. High efficiency planar arrays and array feeds for satellite communications. In *Utah Space Grant Consortium*, 2015. Online; accessed December, 2022.

[27] Kevin Kai Wei Low, Samet Zihir, Tumay Kanar, and Gabriel M. Rebeiz. A 27–31-ghz 1024-element ka-band satcom phased-array transmitter with 49.5-dbw peak eirp, 1-db ar, and ±70° beam scanning. *IEEE Trans. Microw. Theory Techn.*, 70(3):1757–1768, 2022.

[28] Kevin Kai Wei Low, Tumay Kanar, Samet Zihir, and Gabriel M. Rebeiz. A 17.7–20.2-ghz 1024-element k-band satcom phased-array receiver with 8.1-db/k g/t, ±70° beam scanning, and high transmit isolation. *IEEE Trans. Microw. Theory Techn.*, 70(3):1769–1778, 2022.

[29] Mei Qian, Hao Jiang, Xiongjian Zhang, Shaowei Liao, and Quan Xue. A 1024-element dual-circularly polarized phased-array transmitter for ka-band satcom with wide-axial-ratio bandwidth and beamwidth. *IEEE Trans. Microw. Theory Techn.*, pages 1–12, 2025.

[30] Mert Kalfa and Erhan Halavut. A fast method for obtaining active s-parameters in large uniform phased array antennas. In *2013 IEEE International Symposium on Phased Array Systems and Technology*, pages 684–688, 2013.

[31] D.M. Pozar. The active element pattern. *IEEE Trans. Antennas Propag.*, 42(8):1176–1178, 1994.

[32] Qorvo. Ka-band satcom trends and power amplification challenges. *Microwave Product Digest*, May 2020. Accessed: 2025-09-19.

[33] Duixian Liu, Xiaoxiong Gu, Christian Baks, Koichiro Masuko, Yujiro Tojo, Atom O. Watanabe, Arun Paidimarri, Yuta Hasegawa, Gokul Chandran, Xu Lei, Ning Guan, Alberto Valdes-Garcia, and Bodhisatwa Sadhu. A scalable heterogeneous aip module for a 256-element 5g phased array. In *2023 IEEE 73rd Electronic Components and Technology Conference (ECTC)*, pages 467–474, 2023.